学位論文

Anion Control in Transition Metal Oxide Thin Films via Topotactic Reactions

（トポタクティック反応による遷移金属酸化物薄膜のアニオン制御）

平成 27 年 12 月博士（理学）申請

東京大学大学院理学系研究科化学専攻

片山　司

Anion Control in Transition Metal Oxide Thin Films via Topotactic Reactions

by

Tsukasa Katayama

Department of Chemistry
Graduate School of Science
The University of Tokyo
December, 2015

Abstract

Perovskite transition metal oxides have attracted great attention because of their intriguing properties such as colossal magnetoresistance, ferroelectric, and photocatalysis. The physical properties of the oxides are controllable in a wide range through cation substitution. However, in comparison with cation substitution, anion substitution has scarcely been reported because of the difficulty in synthesizing mixed anion compounds such as oxyhydrides and oxyfluorides. Recently, low-temperature topotactic synthesis was developed to fabricate mixed anion compounds that are not accessible by conventional high-temperature synthesis. Although such topotactic reactions have been studied in various bulk samples, the reactions on thin-film samples is expected to have several advantages over bulk: considerably higher reactivity owing to the larger surface area/volume ratio, stabilization of the perovskite-based framework by epitaxial effect, and modification of physical properties by epitaxial strain. Accordingly, in this study, I performed four types of low-temperature topotactic reactions, i.e., hydridation, fluorination, reduction, and oxidation, on perovskite transition metal oxide films, and investigated the properties of the thus obtained mixed anion films.

For topotactic hydridation, I successfully fabricated perovskite $SrCoO_xH_y$ and $SrVO_2H$ oxyhydride thin films from precursor $SrCoO_{2.5}$ and $SrVO_3$ films, respectively, by using CaH_2. The new Co oxyhydride phase, $SrCoO_xH_y$ film, was epitaxially stabilized by substrate and possessed novel two-dimensional Co–H^-–Co networks in the perovskite structure, in contrast to previously reported perovskite oxyhydrides, $SrMO_{3-x}H_x$ (M = Cr, Ti, V). The $SrCoO_xH_y$ thin film exhibited insulating behavior with a much wider band gap than the precursor $SrCoO_{2.5}$, deriving from the large structure distortion. On the other hand, the single-crystalline $SrVO_2H$ film possessed one-dimensional V-H^--V bonds along the out-of-plane direction. With the H^- substitution, binding energy shift of Sr and metal-insulator transition were observed. Furthermore, the synthesis temperature of $SrVO_2H$

film could be lowered by reducing the film thickness.

For topotactic fluorination, I fabricated perovskite $SrFeO_{3-x}F_x$ oxyfluoride epitaxial thin films from $SrFeO_{3-\delta}$ (δ ~ 0, 0.5, 1) precursor films using polyvinylidene fluoride (PVDF). The $SrFeO_{3-x}F_x$ films were obtained by fluorination at 150–270 °C, which is substantially lower than the reaction temperature for polycrystalline bulk samples prepared with PVDF. Furthermore, the fluorine content (x) of the $SrFeO_{3-x}F_x$ film was widely varied by controlling the PVDF-treatment temperature and/or the amount of oxygen vacancies in the precursor film, in contrast to bulk $SrFeO_2F$. The optical bandgap of the $SrFeO_{3-x}F_x$ films was expanded with respect to the fluorine doping and the $SrFeO_2F$ film showed a wider bandgap than perovskite $LaFeO_3$. The density functional theory (DFT)-based calculations suggested that majority of the FeO_4F_2 octahedra in the $SrFeO_2F$ film had *cis* configurations and that the enlarged bandgap mainly originated from bond bending in the O-Fe-O chains. In addition, I also succeeded in fabricating $SrCoO_xF_y$ epitaxial thin film via topotactic fluorination of $SrCoO_{2.5}$ film using PVDF. The Co valence state of the $SrCoO_xF_y$ film was a mixture of 2+ and 3+, which was smaller than that of the $SrCoO_{2.5}$ precursor film, indicating that PVDF acted as a reductive fluorinating agent, in sharp contrast to oxidative F_2 gas. This compound is the first example of perovskite-related Co oxyfluoride with $Co^{2+/3+}$.

For topotactic reduction, I fabricated single-crystalline $SrFeO_2$ epitaxial thin films from $SrFeO_{3-\delta}$ films using CaH_2. The highly crystalline $SrFeO_2$ films prepared on lattice-matched $KTaO_3$ substrate exhibited metallic conduction, while those grown on $SrTiO_3$ and $DyScO_3$ substrates were insulating, in analogy to bulk $SrFeO_2$. From Hall measurements on the metallic $SrFeO_2$ films, the conduction carriers were determined to be *n*-type (i.e., electrons) with a carrier density of 3.1×10^{18} cm^{-3} and mobility of 10.2 cm^2 V^{-1} s^{-1} at 300 K. The electron carriers are supplied by oxygen vacancies or hydrogen ions in the metallic $SrFeO_2$ films. I also found that Sm substitution could enhance the conductivity of $SrFeO_2$ films.

Finally, I performed topotactic oxidation and reduction on *A*-site cation-ordered perovskite $YBaCo_2O_x$ epitaxial thin films using NaClO and CaH_2, respectively. The x values of the $YBaCo_2O_x$ films were successfully controlled in a range of 4.5−6, which was wider than the previous reports, 4.5−5.5, manifesting the high reactivity of the films. The resistivity (ρ) of the films changed depending on x; the $x \sim 4.5$ film was insulating with $\rho = 5.5$ Ωcm at 300 K due to the distortion of the CoO_x layers, while the new phase ($x \sim 6$) showed metallic behavior with $\rho = 3.5 \times 10^{-4}$ Ωcm at 300 K due to hole doping. The new $YBaCo_2O_6$ thin film exhibited ferromagnetic metallic behavior with T_C of 130 K deriving from the double exchange mechanism between Co^{3+} and Co^{4+}. Furthermore, I found large crystal magnetic anisotropy and negative magnetoresistance in the $YBaCo_2O_6$ film. These results proved that topotactic anion doping into transition metal oxide thin films is a promising way of synthesizing new mixed anion compounds.

Contents

1. General introduction 1

1.1 Topotactic reactions on transition metal oxides 1

1.2 Hydridation 3

1.3 Fluorination 8

1.4 Reduction 13

1.5 Oxidation 17

1.6 Topotactic reactions on thin-film samples 20

1.7 Purpose of this study 21

2. Experimental techniques 23

2.1 Sample preparation 23

2.2 Crystallography analysis 27

2.3 Composition analysis 31

2.4 Valence state and electronic structure analysis 35

2.5 Magnetic and transport properties analysis 37

2.6 Density functional theory calculation 39

3. Topotactic hydridation: perovskite $SrCoO_xH_y$ and $SrVO_2H$ films 41

3.1 Introduction 41

3.2 Method 42

3.3 Results and discussion 44

3.4 Conclusion 57

4. Topotactic fluorination: perovskite $SrFeO_{3-x}F_x$ and $SrCoO_xF_y$ films 59

4.1 Introduction 59

4.2 Method 60

4.3 Results and discussion 63

4.4 Conclusion 86

5. Topotactic reduction: metallic conductivity in infinite layer $SrFeO_2$ films 89

5.1 Introduction 89

5.2 Method 90

5.3 Results and discussion 92

5.4 Conclusion 107

6. Oxidation and reduction: *A*-site ordered perovskite $YBaCo_2O_x$ films 109

6.1 Introduction 109

6.2 Method 111

6.3 Results and discussion 112

6.4 Conclusion 123

7. General conclusion 125

Acknowledgement 127

Publications related to the thesis 129

References 131

Chapter 1 General introduction

1.1 Topotactic reactions on transition metal oxides [1]

Transition metal oxides have been intensively studied from both fundamental and practical viewpoints due to their intriguing properties, such as high-temperature superconductivity, colossal magnetoresistance, ferroelectricity, and photocatalysis. Such physical properties are widely controllable through selection constituent elements and/or modification of crystal structure. There are many types of perovskite-related crystal structures, such as simple perovskite ABO_3 and layered perovskite $A_{n+1}B_nO_{3n+1}$. These transition metal oxides are typically synthesized by heating binary metal oxides and/or metal carboxylate at high temperature. This synthesis usually requires elevated temperature (> 1000ºC) and long heating time (in days), because the chemical species in oxides have very low mobility due to the strong metal−oxygen bonds. This high-temperature synthesis has successfully produced a large variety of materials. However, most of them are thermodynamically stable phases or their mixture because the system is nearly in equilibrium. Thus, many kinds of metastable phases are not accessible through this route.

In order to fabricate such metastable materials, low-temperature topotactic synthesis has recently been developed. In certain transition metal oxides, some species have high mobility even at low temperature, while the other species are immobile and form host lattice. The topotactic synthesis utilizes the highly mobile species, resulting in low synthesis temperature (< 500 K), in contrast to the conventional high-temperature synthesis. In the topotactic synthesis, the highly mobile species are removed from, or inserted into, a precursor compound with maintaining the host lattice. For example, when $RbLaNb_2O_7$ is reacted with rubidium vapor at 200ºC, Rb ions are inserted into the host lattice (between $LaNb_2O_7$ layers), resulting in formation of $Rb_2LaNb_2O_7$ phase as shown

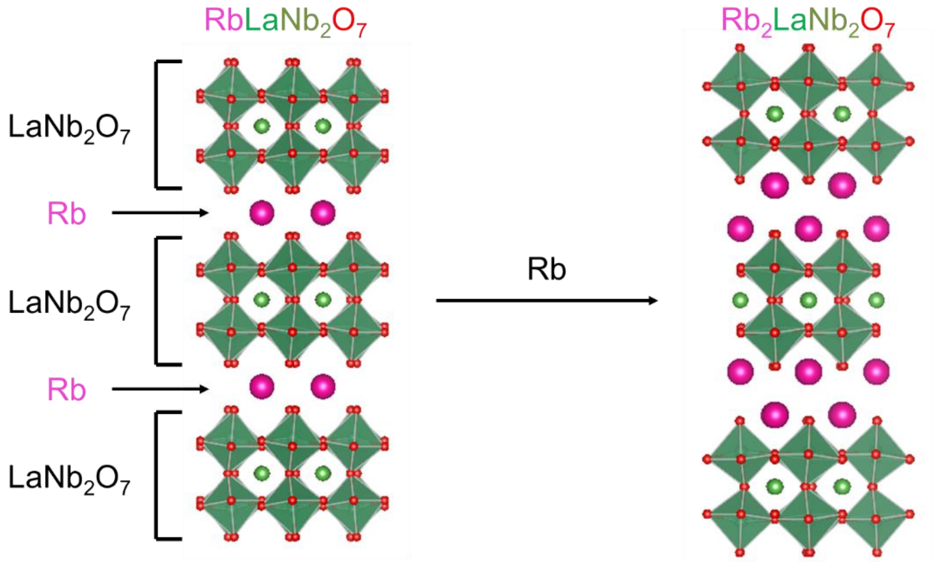

Figure 1-1. Topotactic synthesis of $Rb_2LaNb_2O_7$ from $RbLaNb_2O_7$ by using Rb vapor.

in Fig. 1-1 [2]. Notably, such products, obtained via topotactic synthesis, have very similar crystal structures with the precursors, in contrast to the high-temperature synthesis. In these reactions, the inserted or removed species are required to have much higher mobility than the species of host lattice.

The topotactic reaction is roughly divided into four types: insertion and deintercalation of cations and those of anions. In cation insertion and deintercalation, alkali metals such as Li and Na are generally used as mobile species because of their high ion mobility. The host lattice for the insertion (or deintercalation) reaction must contain the reducible (or oxidizable) metals. Furthermore, the host lattice for the insertion reaction should have either vacant sites within anion frameworks or layered structure. For example, Li ions are inserted as *A*-site cations into ReO_3 with *A*-site cation vacant perovskite structure by reacting with LiI at room temperature, resulting in obtaining Li_xReO_3 [3]:

$$ReO_3 + x\ LiI \rightarrow Li_xReO_3 + x/2\ I_2\ (0 < x < 0.2)$$

For the cation insertion into layered structure, Dion-Jacobson phase is commonly used as a precursor as shown in Fig. 1-1. The Dion-Jacobson phase $RbLaNb_2O_7$ changes into the Ruddlesden-Popper phase $Rb_2LaNb_2O_7$ by the Rb insertion, resulting in expansion of the distance between $LaNb_2O_7$ layers. On the other hand, as a cation deintercalation reaction, $LiCoO_2$ is well studied as an electrode material of lithium ion battery. By reacting $LiCoO_2$ with acid such as HCl and H_2SO_4, lithium ions are removed from the host lattice [4]:

$$LiCo_2O_4 + x\ H^+ \rightarrow Li_{1-x}CoO_2 + x\ Li^+ + x/2\ H_2$$

As well as the topotactic insertion and deintercalation reactions of cations, those of anions have also been widely studied. As mobile species, hydride (H^-), fluoride (F^-), and oxide (O^{2-}) anions are mostly used because of their high ion mobility originating from the large ionicity and small ionic size. The details of topotactic hydridation, fluorination, reduction, and oxidation reactions are presented in the next section.

1.2 Hydridation

1.2.1 Introduction of oxyhydrides

Hydrogen has various chemical states in solid materials: H^+, H, and H^-. Among them, recently, hydride ions (H^-) with negative valence state have attracted considerable interest due to unique properties of metal hydrides. For example, sulfur hydride, mixture of H_3S and H_2S, exhibits high-temperature superconductivity with a transition temperature (T_c) of 203 K under high pressure condition [5]. The T_c value is the highest ever reported and much higher than that of the well-known high-T_c cuprate superconductors ($T_c \leq 164$ K) [6]. In addition, BaH_2 shows very fast pure ionic transport of H^- with anion conductivity of 0.2 Scm^{-1} at 630°C, which is much larger than those of oxide and fluoride anion conductors [7].

The H^- ions can coexist with O^{2-} ions, resulting in formation of oxyhydride compounds. For instance, LaOH is synthesized by reacting oxide La_2O_3 and hydride $LaH_{2.5}$ at 900ºC in hydrogen gas [8]. Introduction of H^- into perovskite-related transition metal oxides is also possible and has recently gained considerable attention as a new technique for changing their electrical and magnetic properties [9-18]. Interestingly, the H^- ions in the perovskite-related transition metal oxyhydrides occupy the oxygen sites of the parent oxides and construct new cation-anion networks.

1.2.2 Topotactic hydridation

Perovskite-related transition metal oxyhydrides are available through topotactic hydridation or high-pressure synthesis methods (Table 1-1). For example, oxyhydride $LaSrCoO_3H_{0.7}$ can be synthesized from precursor oxide $LaSrCoO_4$ by heating with CaH_2 at 450ºC (Fig. 1-2) [9,10]. This topotactic hydridation reaction contains two steps; oxide ions are firstly removed from the precursor, and then hydride ions are inserted into the vacant anion sites as follows:

$$LaSrCoO_4 + 0.65\ CaH_2 \rightarrow LaSrCoO_{3.35} + 0.65\ CaO + 0.375\ H_2$$

$$LaSrCoO_{3.35} + 0.35\ CaH_2 \rightarrow LaSrCoO_3H_{0.7} + 0.35\ CaO$$

Metal hydride CaH_2 works as both reducing and hydride source reagents. During the reaction, the Co oxidation state is reduced from 3+ to 1.75+ due to the strong reducing

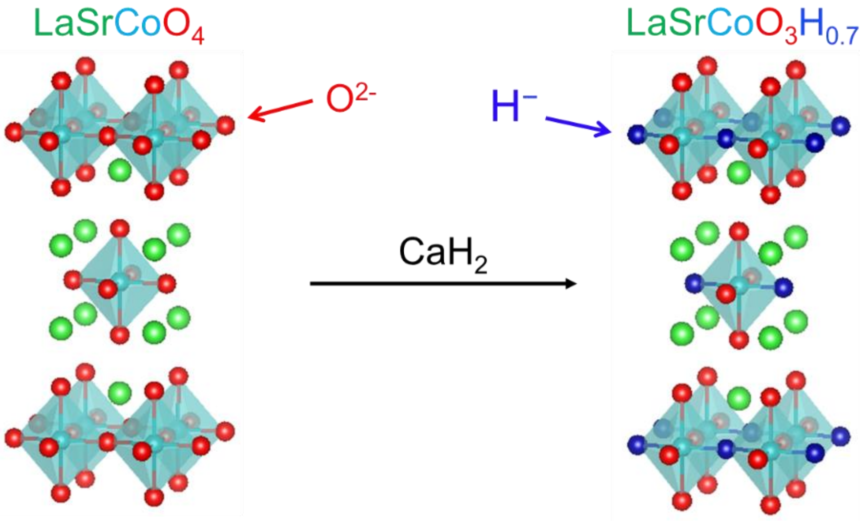

Figure 1-2. Topotactic synthesis of $LaSrCoO_3H_{0.7}$ from $LaSrCoO_4$ by using CaH_2.

power of CaH_2. The standard electrode potential of H^- in CaH_2 is estimated to be $E^0(H^-/H_2) = -2.2$ V [10]. The obtained oxyhydride $LaSrCoO_3H_{0.7}$ has Co-H^--Co bonds parallel to the *b*-axis and Co-O^{2-}-Co bonds along the *a* and *c*-axes; i.e., it has a one-dimensionally ordered Co-H^- bond network (1D-type). As shown in Table 1-1, the other topotactic hydridation reactions also utilizes CaH_2 reagent to dope H^- ions into the precursor oxides.

Table 1-1. Perovskite-related transition metal oxyhydrides

Composition	**Synthesis method**	**Physical property**	**Anion coordination**	**Reference**
$LaSrCoO_3H_{0.7}$	Topotactic hydridation: from $LaSrCoO_4$ and CaH_2 at 450 °C	Antiferromagnet (T_N = 380 K)	1D-type	[9-11]
$Sr_3Co_2O_{4.33}H_{0.84}$	Topotactic hydridation: from $Sr_3Co_2O_{7-\delta}$ and CaH_2 at 255 °C	lack of long-range magnetic order	2D-type	[14]
$ATiO_{3-x}H_x$ (A = Ba, Sr, Ca, $x = 0.1-0.3$)	Topotactic hydridation: from $ATiO_3$ and CaH_2 at 500−580 °C	Metallic behavior H^- is exchangeable with H_2 gas at 400°C.	Random-type	[15] [17]
$EuTiO_{3-x}H_x$ ($x = 0.07-0.3$)	Topotactic hydridation: from $EuTiO_3$ and CaH_2 at 550−600 °C	Ferromagnetic metal (T_C = 12 K at $x = 0.3$)	Random-type	[18]
$Sr_{n+1}V_nO_{2n+1}H_n$ ($n = 1, 2, \infty$)	Topotactic hydridation: from $Sr_{n+1}V_nO_{3n+1}$ and CaH_2 at 600−630 °C	Antiferromagnet (T_N = 170, 240, > 300 K when $n = 1, 2, \infty$, respectively)	1D-type	[12]
$SrCrO_2H$	High-pressure high-temperature technique: from SrH_2, SrO, Cr_2O_3 at 5 GPa and 1000 °C	Antiferromagnet (T_N > 380 K)	Random-type	[16]
$Sr_2VO_{4-x}H_x$ ($x \leq 1.01$)	High-pressure high-temperature technique: from SrH_2, SrO, VO_2 at 5 GPa and 1200 °C		2D-type ($x < 0.2$), 1D-type ($x > 0.7$)	[13]

1.2.3 Crystal structure of perovskite-related metal oxyhydrides

As is observed in $LaSrCoO_3H_{0.7}$, perovskite-related transition metal oxyhydrides have several types of oxide/hydride ion arrangements because hydride ions could have different oxidation state, orbital and ionic size from oxide ions. The 1D-type anion coordination in $LaSrCoO_3H_{0.7}$ is also found in $SrVO_2H$ as shown in Fig. 1-3(a) [12]. The H^- anions of $SrVO_2H$ occupy the axial positions of VO_4H_2 octahedral units, resulting in 1D ordered V-H^- bond networks along *c*-axis. Such 1D-type oxyhydrides possess much shorter metal-hydride bonds but longer metal-oxide bonds as compared to the corresponding metal-oxide bonds in the parent oxides. Indeed, $SrVO_2H$ has shorter *c*-axis length, 0.366 nm, but has longer *a*-axis length, 0.393 nm, than *a*-axis length of the parent oxide $SrVO_3$, 0.384 nm. This derives from smaller ionic radius of H^- (0.104−0.139 nm) than that of O^{2-} (0.138 nm). The size of H^- is of wide range, depending on the surrounding environment.

The other kind of oxide/hydride ion arrangements is metal-H^- two-dimensional network (2D-type). For example, hydride ions in oxyhydrides $Sr_2VO_{3-x}H_x$ ($x < 0.2$) and $Sr_3Co_2O_{4.33}H_{0.84}$ are randomly distributed in the equatorial sites, while the apical sites are

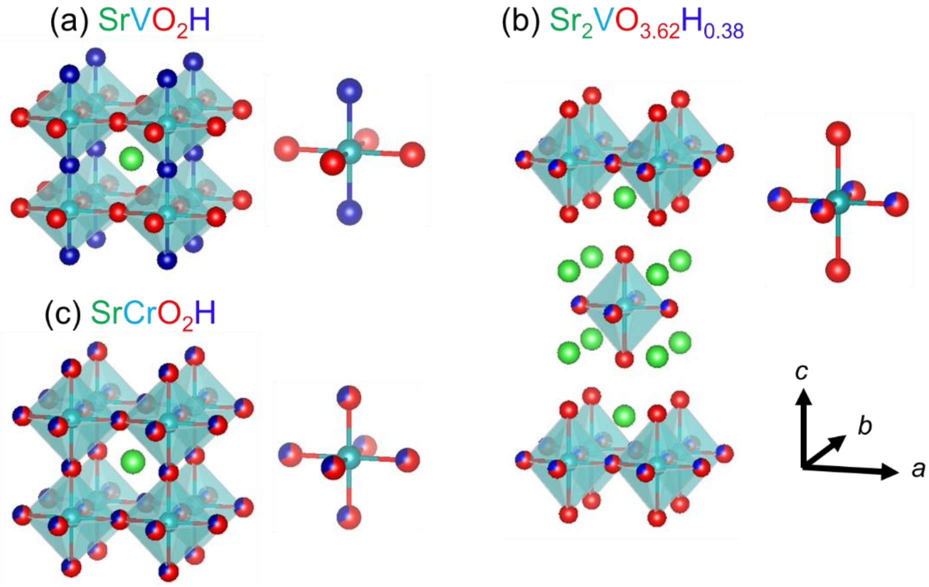

Figure 1-3. Crystal structures of (a) $SrVO_2H$ (1D-type), (b) $Sr_2VO_{3.62}H_{0.38}$ (2D-type) and (c) $SrCrO_2H$ (Random-type).

occupied by oxide ions as shown in Fig. 1-3(b) [13,14]. The 2D-type oxyhydrides have shorter metal−X (X = O^{2-}, H^{-}) bonds and longer metal-oxide bonds as compared to the corresponding metal-oxide bonds of the parent oxides. The final type of anion coordination is random distribution of oxide/hydride ions (Random-type), which is observed in $BaTiO_{3-x}H_x$ and $SrCrO_2H$ as shown in Fig. 1-3(c) [15,16]. The Random-type oxyhydrides $BaTiO_{3-x}H_x$ and $SrCrO_2H$ have cubic structures.

1.2.4 Physical properties of perovskite-related transition metal oxyhydrides

The substitution of H^{-} modifies the physical properties of the parent oxides. There are mainly three roles of the H^{-} substitution: alternation of transition metal oxidation states, construction of new metal(d)−hydride(s) bonds, and change of the lattice parameters. The first one utilizes the difference in valence state between O^{2-} and H^{-}. For example, insulating ATiO$_3$ (A = Ba, Sr, Ca) can be transferred into metallic compounds via H^{-} substitution [15,17]. It is reported that the carrier density of $SrTiO_{2.75}H_{0.25}$ is 4.1×10^{21} cm^{-3}, which is almost the same as the hydrogen density of 4.2×10^{21} cm^{-3}, indicating that H^{-} works as an effective electron donor [17].

The second role of H^{-} substitution utilizes the orbital difference between H 1s and O 2p, which affects the nature of metal-anion bonds and produces new properties. One example is $LaSrCoO_3H_{0.7}$, in which H 1s orbitals form σ bonding with Co 3d e_g orbitals, but hardly interact with Co 3d t_{2g} orbitals, because H 1s orbitals have σ-symmetry (Fig. 1-4) [9]. The σ bonding between Co 3d e_g and H 1s orbitals produces purely antiferromagnetic superexchange interaction between the Co ions, and the shorter Co-H distance makes the antiferromagnetic interaction stronger [9]. Therefore, $LaSrCoO_3H_{0.7}$ exhibits strong antiferromagnetic interaction with Néel temperature (T_N) of 380 K, which is higher as compared to Co oxides with K_2NiF_4-type structure including $LaSrCoO_{3.5}$ (T_N = 110 K) [19]. Another example is $SrVO_2H$ (Fig. 1-3(a)). The V 3d^2 electrons in the t_{2g} orbitals interact with not H 1s but O 2p orbitals, resulting in low dimensional V 3d – O

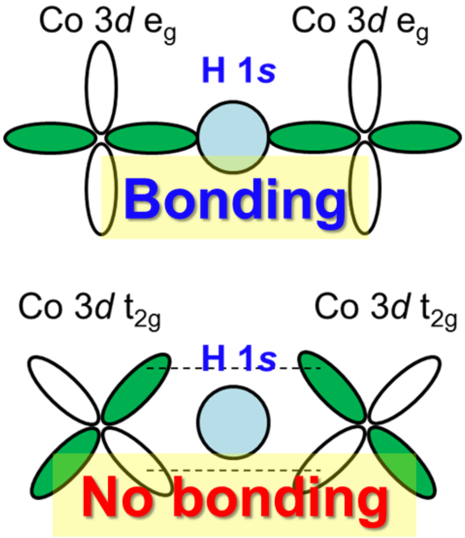

Figure 1-4. H 1s orbitals interact with not Co 3*d* t_{2g} but e_g orbitals.

2*p* bonding system in $SrVO_2H$. This leads to strong antiferromagnetic coupling with Néel temperature above 300 K [12,20].

The H^- substitution can also be used as a tool to control the lattice parameter. For example, perovskite oxyhydride $SrCrO_2H$ has the highest Goldschmidt tolerance factor (t) value in perovskite Cr^{3+} oxides, including $RCr^{3+}O_3$ [16]. It is known that perovskite $RCr^{3+}O_3$ has stronger antiferromagnetic interaction with increasing the t value. Thus, $SrCrO_2H$ exhibits antiferromagnetic behavior with high T_N of 380 K [16].

1.3 Fluorination

1.3.1 Introduction of transition metal oxyfluorides

Since the discovery of high-T_c superconductivity (T_c = 46 K) in non-ordinary oxyfluorides $Sr_2CuO_2F_{2+x}$, the replacement of O^{2-} by F^- in transition-metal oxides has attracted considerable attention [21]. The transition metal oxyfluorides can be fabricated by using the conventional high-temperature synthesis as far as the amount of fluorine is small. For example, $Ba_5Co_5FO_{13-\delta}$ is obtained by heating BaO_2, BaF_2 and Co_3O_4 at

1030 °C in a sealed gold tube [22]. However, when the F^- amount is large, high-temperature synthesis tends to produce very stable fluoride phases such as AEF_2, $LnOF$, and LnF_3 (AE = alkali earth metal, Ln = lanthanoid), resulting in failure of synthesis of perovskite-related transition metal oxyfluorides [23]. To fabricate such compounds, low-temperature topotactic or high-temperature high-pressure synthesis routes are demanded. Indeed, low-temperature topotactic fluorination synthesis has succeeded in yielding many perovskite-related transition metal oxyfluorides, while the high-temperature high-pressure synthesis also produces some oxyfluorides such as $PbFeO_2F$ [24] and Sr_2CoO_3F [25].

1.3.2 Low-temperature topotactic fluorination

Perovskite-related transition metal oxyfluorides have two types of fluorine sites. First one is interstitial sites between the perovskite block layers. By reacting Ruddlesden-Popper $Sr_3Ru_2O_7$ with CuF_2 at 300°C, fluorine ions are inserted between the perovskite block layers, yielding $Sr_3Ru_2O_7F_2$ as shown in Fig. 1-5 [26]:

$$Sr_3Ru_2O_7 + CuF_2 + 0.5\ O_2 \rightarrow Sr_3Ru_2O_7F_2 + CuO$$

The inserted fluorine ions form SrF rock salt layers between the perovskite blocks, and the Ru ions are oxidized from 4+ to 5+ during the fluorination reaction. The second fluorine site is oxygen and/or anion-vacancy sites in the precursor oxides. For example, by heating oxygen vacant perovskite $SrCoO_{2.5}$ with F_2 gas, fluorine ions are inserted into the vacant sites of the precursor near the Co cation, yielding perovskite $SrCoO_{2.5}F_{0.5}$ [27]:

$$SrCoO_{2.5} + 0.25\ F_2 \rightarrow SrCoO_{2.5}F_{0.5}$$

The inserted fluorine ions form CoO_5F octahedral coordinations, and the Co ions are oxidized from 3+ to 3.5+ associated with the fluorination. This oxidative fluorination derives from the strong oxidizing power of F_2 gas.

In terms of the oxidizing/reducing power, fluorine reagents are roughly divided

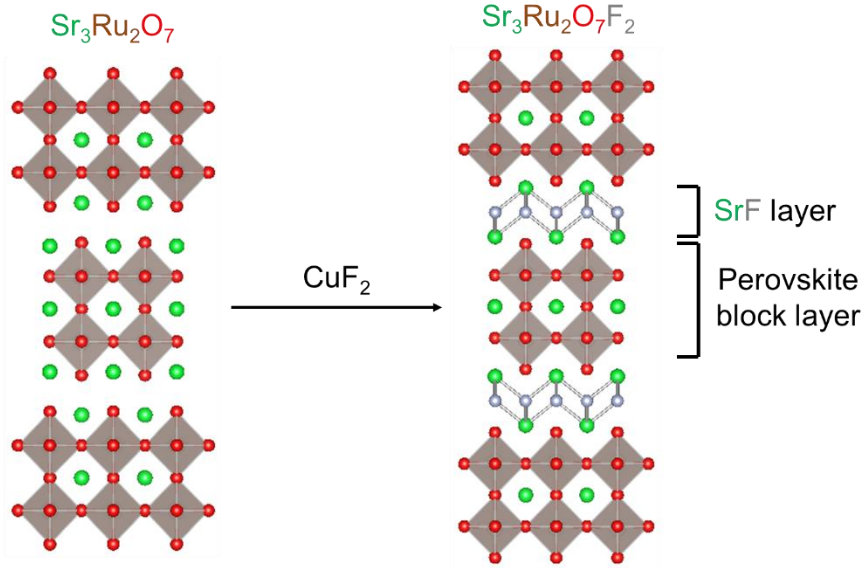

Figure 1-5. Topotactic synthesis of $Sr_3Ru_2O_7F_2$ from $Sr_3Ru_2O_7$ by using CuF_2.

into three groups. The first group, such as F_2 gas, XeF_2, and MF_2 (M = Cu, Zn), has strong oxidizing power [23,26-29]. When F_2 gas reacts, F valence state changes from 0 to –1, which tends to accompany oxidation of transition metal. Due to the strong oxidizing power, F_2 gas and XeF_2 are difficult to handle. The second group is reductive fluorination reagent such as NH_4F. During the fluorination reaction, NH_4F decomposes into NH_3 and HF, and the gaseous HF works as a reductive fluorine agent [23]. This reaction yields water as the reaction product, and also easily yields impurity AEF_2 phase [30]. The third group is fluorine containing polymer such as polyvinylidene fluoride (PVDF, monomer unit CH_2CF_2) and polytetrafluoroethylene (PTEE, monomer unit CF_2) [33]. These polymers have low melting points (~180ºC for PVDF and ~330ºC for PTEE), resulting in good compositional homogeneity. Interestingly, PVDF can work as both reductive and oxidative fluorination agent as shown in Table 1-2 [31-38]. For instance, $SrFeO_{3-\delta}$ changes into $SrFeO_2F$ by heating with PVDF [31]:

$$SrFeO_{3-\delta} + 0.5/n\ (CH_2CF_2)_n \rightarrow SrFeO_2F + (0.5+\delta)\ C + 0.5\ H_2O + (0.5-\delta)\ CO$$

This process reduces the iron ions from 3+/4+ to 3+ because not only insertion but substitution of fluorine ions occur.

Table 1-2. Perovskite-related transition metal oxyfluorides synthesized via topotactic reaction using PVDF

Product	**Precursor**	**Valence state change**	**Reaction temperature**	**Reference**
$RbLaNb_2O_6F$	$RbLaNb_2O_7$	Nb:4.5+ → 4+	400 ℃	[33]
$SrFeO_2F$	$SrFeO_{3-\delta}$	Fe: 3+/4+ → 3+	400 ℃	[31][32]
$BaFeO_2F$	$BaFeO_{3-\delta}$	Fe: 3+/4+ → 3+	400 ℃	[34]
$La_{1-x}Sr_xFeO_{3-x}F_x$	$La_{1-x}Sr_xFeO_{3-\delta}$	Fe: 3+/4+ → 3+	375 ℃	[35]
$Sr_3Fe_2O_{5.28}F_{1.72}$	$Sr_3Fe_2O_{7-\delta}$	Fe: 3+/4+ → 3.1+	375 ℃	[36]
$Sr_3Fe_2O_4F_4$	$Sr_3Fe_2O_{7-\delta}$	Fe: 3+/4+ → 3+	375 ℃	[36]
$Sr_3Fe_2O_3F_6$	$Sr_3Fe_2O_{7-\delta}$	Fe: 3+/4+ → 3+	375 ℃	[36]
$Ca_2CuO_2F_2$	Ca_2CuO_3	Cu: 2+ → 2+	350 ℃	[37]
$Sr_2TiO_3F_2$	Sr_2TiO_4	Ti: 4+ → 4+	350 ℃	[37]
$Ln_{1.2}Sr_{0.8}Mn_2O_7F_2$ (*Ln* = Pr, Nd, Sm, Eu, Gd)	$Ln_{1.2}Sr_{0.8}Mn_2O_7$ (*Ln* = Pr, Nd, Sm, Eu, Gd)	Mn: 4.4+ → 5.4+	300-350 ℃	[38]

1.3.3 Crystal structure of perovskite-related metal oxyfluorides

The oxygen and fluorine positions in the oxyfluorides are hardly distinguished via X-ray and neutron diffraction methods, because these atoms have very similar electron configuration and neutron scattering cross section. In order to determine possible anion coordination of oxyfluorides, bond valence sum calculation and Madelung energy calculation are often used [23]. According to the calculations, some perovskite-related oxyfluorides are reported to have oxide/fluoride order. One of the examples is $Sr_2CuO_2F_{2+x}$ [21]. It has fluorine ions in both substitutional (F) and interstitial (F') sites as shown in Fig. 1-6. In the CuO_4F_2 octahedra of $Sr_2CuO_2F_{2+x}$, the substitutional fluorine ions reside at the apical anion sites, while oxygen ions occupy the equatorial sites, resulting in flat CuO_2 plane. The formation of CuO_4 square-planer is energetically favored [21]. When $x = 0.33$, $Sr_2CuO_2F_{2+x}$ exhibits high-T_c superconductivity with T_c of 46 K owing to the hole doping into the CuO_2 plane [21].

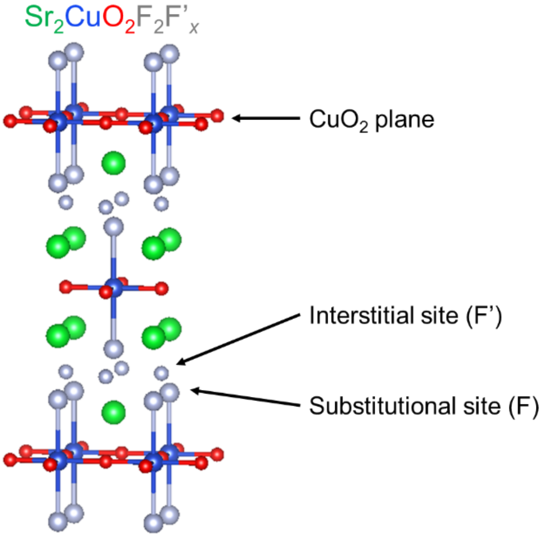

Figure 1-6. Crystal structure of $Sr_2CuO_2F_{2+x}$.

1.3.4 Physical properties of perovskite-related transition metal oxyfluorides

The fluorination can be utilized as a method for carrier doping; replacement of O^{2-} by F^- supplies electron, while insertion of F^- supplies hole. This technique has been applied to cuprates, yielding many superconducting cupper oxyfluorides such as $Sr_2CaCu_2O_{4.3}F_{2.4}$ (T_c = 99 K), and $Sr_2Ca_2Cu_3O_{6.4}F_{3.2}$ (T_c = 111 K) [39]. Other example of the carrier doping by F^- substitution is Dion-Jacobson phase $RbLaNb_2O_6F$ [33]. The F^- substitution changes insulating $RbLaNb_2O_7$ to metallic $RbLaNb_2O_6F$.

Physical properties of perovskite-related transition metal oxyfluorides strongly depends on the kind of transition metal ion. Iron oxyfluorides have attracted interest due to their unique magnetic properties. For example, perovskite $SrFeO_2F$ and hexagonal perovskite 15R-$BaFeF_{0.2}O_{2.42}$ exhibit strong antiferromagnetic coupling with T_N of 685–710 K and ~700 K, respectively [40,41]. Such high T_N derives from the changes of the Fe–X–Fe (X = O, F) bonding, and reduction of iron ions [40]. Interestingly, in perovskite iron oxides, $A\mathrm{FeO_2F}$ (A = Sr [41], Ba [42], Pb [24]), the T_N value increases from 645 to 710 K by decreasing the iron-anion distance from 2.03 to 1.98 Å, associating with the increase of orbital overlap. Perovskite-related cobalt oxyfluorides also exhibit strong antiferromagnetic interaction such as $\mathrm{LaSrCoFeO_5F}$ ($T_\mathrm{N} > 300$ K) [43], $\mathrm{BaCoO_xF_y}$ (T_N = 130 K) [44], and $\mathrm{Sr_2CoO_3F}$ (T_N = 320 K) [25]. Indeed, almost all perovskite-related iron and cobalt oxyfluorides are categorized as antiferromagnetic insulators. On the other hand, layered-type manganese oxyfluorides, such as $\mathrm{LaSrMnO_4F}$ and $\mathrm{La_{1.2}Sr_{1.8}Mn_2O_7F}$, do not exhibit long range magnetic order [45]. Nickel oxyfluoride $\mathrm{Sr_2NiO_3F}$ does not have long range magnetic order, as well, but shows spin glass behavior below 11 K [46].

1.4 Reduction

1.4.1 Topotactic reduction of perovskite transition metal oxides

Topotactic oxygen deintercalation reaction can produce transition metal oxides with anion-vacancy ordered perovskite structure. One of the well-studied anion-vacancy ordered perovskite phase is $AB\mathrm{O_{2.5}}$ (A = Alkaline earth metal and rare earth element, B = transition metal). There are three types of $AB\mathrm{O_{2.5}}$ phases as illustrated in Fig. 1-7 [47]. The type of anion-vacancy order depends on the kind of transition metal. For example, manganese oxide $\mathrm{CaMnO_{2.5}}$ [48] and copper oxides $\mathrm{SrCuO_{2.5}}$ [49] have $\mathrm{MnO_5}$ and $\mathrm{CuO_5}$ square-pyramidal coordinations, respectively, as shown in Fig. 1-7(a). On the other hand, nickel oxide $\mathrm{LaNiO_{2.5}}$ [50] has alternately arranged $\mathrm{NiO_6}$ octahedral and $\mathrm{NiO_4}$ square planner coordinations (Fig. 1-7(b)), while iron oxide $\mathrm{SrFeO_{2.5}}$ [51] and cobalt oxides $\mathrm{SrCoO_{2.5}}$ [47] have brownmillerite structure with alternately arranged $B\mathrm{O_6}$ octahedral and $B\mathrm{O_4}$ tetrahedral coordinations (B = Fe and Co, respectively) (Fig. 1-7(c)). The $AB\mathrm{O_{2.5}}$ phases can be obtained from perovskite $AB\mathrm{O_3}$ by various means of topotactic reductions: electrochemical reduction and chemical reduction using reducing agents. For example, brownmillerite $\mathrm{SrCoO_{2.5}}$ can be obtained from perovskite $\mathrm{SrCoO_3}$ via electrochemical

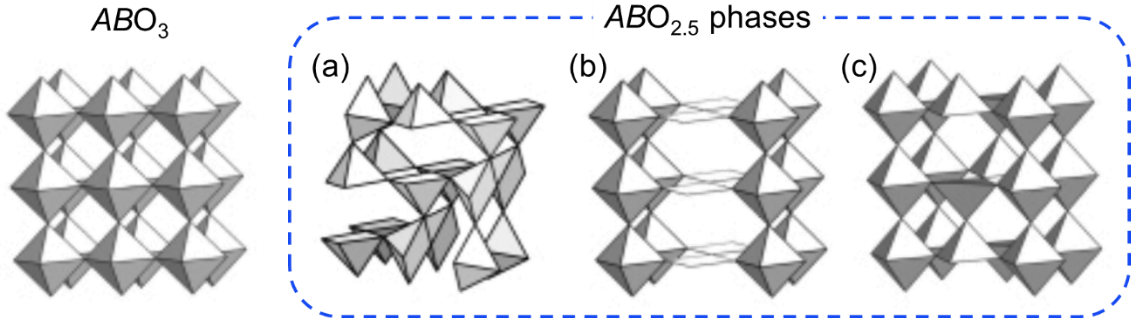

Figure 1-7. Crystal structures of $ABO_{2.5}$ phases when *B*-site cations are (a) Mn, Cu, (b) Ni, (c) Fe and Co [47]. Reprinted with permission from R. L. Toquin, W. Paulus, A. Cousson, C. Prestipino, and C. Lamberti, J. Am. Chem. Soc. **128**, 13161 (2006). Copyright 2006 American Chemical Society

reduction method. In this method, $SrCoO_3$ and Pt are used as cathode and anode electrodes, respectively. The electrolyte is KOH solution. When voltage is applied between the electrodes, $SrCoO_3$ is reduced as follow [52]:

$$SrCoO_3 + 0.5\ H_2O + e^- \rightarrow SrCoO_{2.5} + OH^-$$

This is a reversible reaction. $SrCoO_{2.5}$ can also be obtained from $SrCoO_3$ by chemical reduction using H_2O_2 solution [52]:

$$SrCoO_3 + 0.5\ H_2O_2 \rightarrow SrCoO_{2.5} + 0.5\ H_2O + 0.5\ O_2$$

In this reaction, H_2O_2 solution works as a reducing agent. There are not only solution- but also gas- and solid-phase reducing agents. Heating $CaMnO_3$ in H_2 gas at 300ºC yields anion-vacancy ordered $CaMnO_{2.5}$ [48], while heating $LaCoO_3$ with Zr metal at 400ºC yields brownmillerite $LaCoO_{2.5}$ [53]:

$$CaMnO_3 + 0.5\ H_2 \rightarrow CaMnO_{2.5} + 0.5\ H_2O$$

$$LaCoO_3 + 0.5/y\ Zr \rightarrow LaCoO_{2.5} + 0.5/y\ ZrO_y$$

By using metal hydrides, including NaH, CaH_2, and LiH, as reducing agents, more oxygen vacancies can be introduced into the perovskite-related structure [54]. For example, $LaNiO_2$ with infinite layer structure can be synthesized from perovskite $LaNiO_3$

by heating with NaH in a sealed glass tube (Fig. 1-8) [55]:

$$LaNiO_3 + NaH \rightarrow LaNiO_2 + NaOH$$

$LaNiO_2$ possesses a NiO_4 square planner coordination, and very low Ni oxidation state of Ni^{1+}. The driving force of the strong reducing power of NaH is large thermodynamic energy difference between NaOH and NaH.

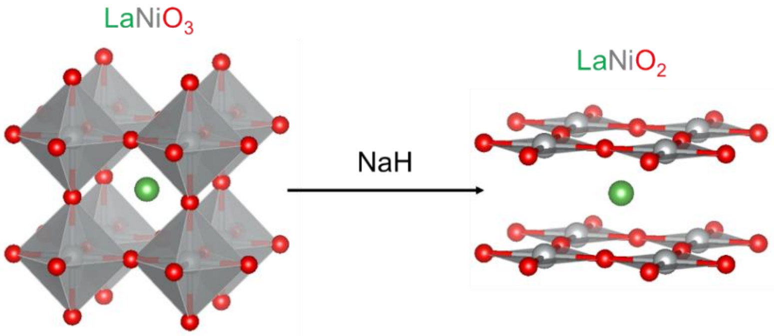

Figure 1-8. Topotactic synthesis of $LaNiO_2$ from $LaNiO_3$ by using NaH.

1.4.2 Low-temperature topotactic reduction of perovskite transition metal oxides using metal hydrides [54]

As observed in $LaNiO_2$, low-temperature topotactic reduction reactions using metal hydrides can produce new transition metal oxides, which possess very low oxidation state and/or unique coordination of transition metal centers (Table 1-3). For example, $SrFeO_2$, which is obtained via topotactic reduction using CaH_2, possesses infinite FeO_2 layers of corner-sharing FeO_4 square planers similar to $LaNiO_2$ (Fig. 1-8), in contrast to common iron oxides which have three-dimensional coordinations such as FeO_6 octahedra and FeO_4 tetrahedra [58]. The topotactic reduction synthesis of infinite-layer $SrFeO_2$ from perovskite $SrFeO_{3-\delta}$ using CaH_2 is expressed as

$$SrFeO_{3-\delta} + (1-\delta)\ CaH_2 \rightarrow SrFeO_2 + (1-\delta)\ CaO + (1-\delta)\ H_2$$

The low-temperature topotactic reductions with metal hydrides are also applied to iron and nickel oxides with layered perovskite structures, resulting in producing new layered

Table 1-3. Topotactic reduction reactions of perovskite-related transition metal oxides using metal hydrides

Product	**Valence**	**Precursor**	**Reagent**	**Reaction temperature**	**Reference**
$LaNiO_2$	Ni^{1+}	$LaNiO_2$	NaH	200 ºC	[55]
$La_3Ni_2O_6$	$Ni^{1.5+}$	$La_3Ni_2O_7$	CaH_2	350 ºC	[56]
$La_4Ni_3O_8$	$Ni^{1.33+}$	$La_4Ni_3O_{10}$	NaH	200 ºC	[57]
$A\mathrm{FeO}_2$ (A = Sr, Ca)	Fe^{2+}	$A\mathrm{FeO}_{3-\delta}$ (A = Sr, Ca)	CaH_2	280 ºC	[58,59]
$BaFeO_2$	Fe^{2+}	$BaFeO_{2.5}$	NaH	140 ºC	[60]
$Sr(Fe_{0.5}Ru_{0.5})O_2$	Fe^{2+}, Ru^{2+}	$Sr(Fe_{0.5}Ru_{0.5})O_3$	CaH_2	400 ºC	[61]
Sr_2FeO_3	Fe^{2+}	Sr_2FeO_4	CaH_2	280 ºC	[62]
$Sr_3Fe_2O_5$	Fe^{2+}	$Sr_3Fe_2O_{7-\delta}$	CaH_2	350 ºC	[63]
$La_{1-x}Ca_xMnO_2$ (x = 0.6,0.7,0.9)	$Mn^{(1+x)+}$	$La_{1-x}Ca_xMnO_3$ (x = 0.6,0.7,0.9)	NaH	210 ºC	[64]
$\mathrm{La}A\mathrm{MnO}_{3.5}$ (A = Sr, Ba)	Mn^{2+}	$\mathrm{La}A\mathrm{MnO}_4$ (A = Sr, Ba)	CaH_2	480 ºC	[65]
$LaBaCo_2O_{4.25}$	$Co^{1.75+}$	$LaBaCo_2O_5$	NaH	210 ºC	[66]
$YBaCo_2O_{4.25}$	Co^{2+}	$YBaCo_2O_5$	NaH	210 ºC	[66]

perovskite iron oxides, Sr_2FeO_3 [62] and $Sr_3Fe_2O_5$ [63], and nickel oxides, $La_3Ni_2O_6$ [56] and $La_4Ni_3O_8$ [57], with FeO_4 and NiO_4 square planner coordinations, respectively.

In topotactic reduction of cobaltites, *A*-site cation-ordered perovskite $LaBaCo_2O_{4.25}$ is synthesized from $LaBaCo_2O_5$ using NaH [66]. $LaBaCo_2O_{4.25}$ has low Co oxidation state of 1.75+ and contains CoO_4 square planner coordination. It is predicted that the Co^{1+} ions exist in the square planner coordinations, while the Co^{2+} ions are located in the CoO_4 tetragonal coordination. On the other hand, heating $YBaCo_2O_5$ with NaH produces $YBaCo_2O_{4.5}$ with Co^{2+}, demonstrating that the amount of oxygen vacancies in the cobaltites depends on the size of the *A*-site cations.

In addition, anion vacant perovskite $La_{1-x}Ca_xMnO_2$ is obtained via low-temperature topotactic reduction using NaH, [64]. The Mn oxidation state of

$La_{1-x}Ca_xMnO_2$ is a mixture of 1+ and 2+, which is much lower than those of conventional manganese oxides.

1.5 Oxidation

1.5.1 Introduction of topotactic oxidation

Since the discovery of high-T_c superconductivity in $La_2CuO_{4+\delta}$, topotactic oxidation methods for transition metal oxides have been widely studied [67-72]. The parent compound La_2CuO_4 is an antiferromagnetic insulator, however the excess oxygen insertion induces superconducting transition due to the hole doping effect. The T_c value of $La_2CuO_{4+\delta}$ is known to depend on the amount of excess oxygen (δ); T_c is 32–36 K for $\delta \sim 0.03$ and 42–45 K for $\delta \sim 1.1$ [67]. So far, various means of topotactic excess oxygen insertion into La_2CuO_4 have been reported. In this section, four kinds of topotactic oxidation methods are introduced as representative examples. The first one is high-temperature oxidation using oxygen gas. For instance, heating La_2CuO_4 at 600ºC in 1–3 kbar oxygen gas yields $La_2CuO_{4+\delta}$, which includes three superconducting phases with T_c = 32, 36 and 45 K, although the T_c = 45 K phase is very small [68]. The second oxidation method is low-temperature solid-gas oxidation such as ozone oxidation and plasma oxidation [69]. In the ozone oxidation process, ozone (O_3) changes into oxygen (O_2) and gives an oxygen atom to La_2CuO_4 as follows:

$$La_2CuO_4 + \delta\, O_3 \rightarrow La_2CuO_{4+\delta} + \delta\, O_2$$

Ozone has much stronger oxidizing power than oxygen gas, leading to low reaction temperature. The third oxidation method is electrochemical oxidation [67]. In this method, La_2CuO_4 and Pt are used as anode and cathode electrodes, respectively, in NaOH electrolyte. When voltage is applied between the electrodes, La_2CuO_4 is oxidized at anode as follows:

$$La_2CuO_4 + 2\delta\ OH^- \rightarrow La_2CuO_{4+\delta} + \delta\ H_2O + 2\delta\ e^-$$

Notably, at high voltage (0.61 V versus Ag/AgC1), the evolution of oxygen takes place according to the following reaction:

$$2\ OH^- \rightarrow H_2O + 1/2\ O_2 + 2\ e^-$$

The δ values are controllable from 0 to 0.36 by using electrochemical oxidation method, and the T_c = 45 K phase is obtained at δ = 0.11. The forth oxidation method is solid-solution oxidation using a solution with strong oxidizing power, such as $KMnO_4$ [70], NaBrO [71] and NaClO [72] solutions. By reacting these solutions with La_2CuO_4, excess oxygen ions are introduced into the precursor La_2CuO_4 as follows:

$$La_2CuO_4 + \delta\ KMnO_4 \rightarrow La_2CuO_{4+\delta} + \delta/2\ K_2MnO_4 + \delta/2\ MnO_2$$

$$La_2CuO_4 + \delta\ NaBrO \rightarrow La_2CuO_{4+\delta} + \delta\ NaBr$$

$$La_2CuO_4 + \delta\ NaClO \rightarrow La_2CuO_{4+\delta} + \delta\ NaCl$$

In general, the oxidizing power of the solutions increases with increasing their standard electrode potentials. The standard electrode potentials of $KMnO_4$, NaBrO, and NaClO solutions are $E^0(MnO_4^-/MnO_2)$ = 0.60 V, $E^0(BrO^-/Br^-)$ = 0.766 V, $E^0(ClO^-/Cl^-)$ = 0.890 V, respectively, suggesting that NaClO solution has stronger oxidizing power than $KMnO_4$ and NaBrO solutions. Indeed, oxidation process using NaClO solution produces the T_c = 45 phase, while those using $KMnO_4$ and NaBrO solutions produce the T_c = 40 K phases. This method is much easier than the electrochemical oxidation method, and has an advantage of making large-volume samples.

1.5.2 Low-temperature topotactic oxidation on cation-ordered perovskite oxides

These low-temperature topotactic oxidation methods enable to synthesize many compounds which cannot be obtained via conventional high-temperature synthesis. One example is cation-ordered perovskite oxides. In general, cation-ordered perovskite oxides are not energetically favored as compared to the cation-disordered perovskite oxides according to the entropy law. However, low-temperature oxidation can produce *A*-site cation-ordered perovskite $LaBaMn_2O_6$ from $LaBaMn_2O_{5.5}$ as shown in Fig. 1-9, while conventional high-temperature synthesis yields cation-disordered perovskite [73]. The precursor $LaBaMn_2O_{5.5}$ has *A*-site cation-ordered structure, because the oxygen vacancy ordering makes the cation-ordered structure more energetically stable. The metastable cation-ordered perovskite $LaBaMn_2O_6$ exhibits antiferromagnetic behavior with a higher T_N value of 335 K as compared to the disordered one (T_N = 270 K). There are some other reports of low-temperature topotactic oxidation synthesis of metastable cation-ordered perovskite oxides such as *A*-site cation-ordered perovskite $LaBaCo_2O_6$ [74] and *B*-site cation-ordered perovskite Ca_2FeMnO_6 [75].

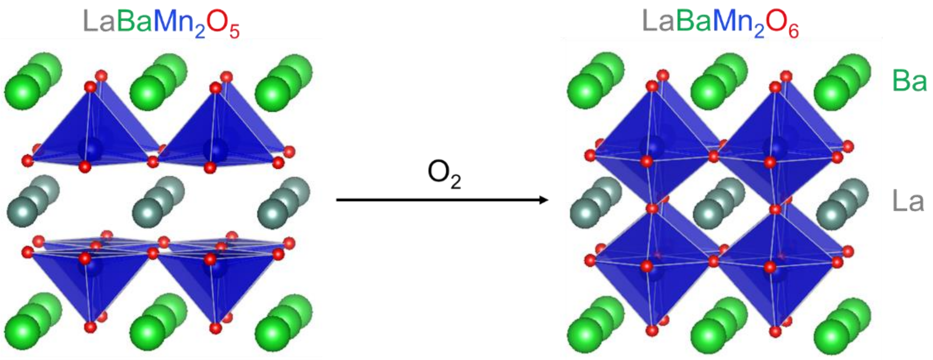

Figure 1-9. Topotactic synthesis of *A*-site cation-ordered perovskite $LaBaMn_2O_6$ from $LaBaMn_2O_5$.

1.6 Topotactic reactions on thin-film samples

Although the topotactic reactions are mainly studied on polycrystalline powder samples, some reactions have been conducted on thin film samples. There are two characteristics of thin film samples: small diffusion path length (nanometer-order), and epitaxial strain from substrate (Fig. 1-10). These characteristics lead to advantages of topotactic reactions on thin film samples. One of the advantages is capability to obtain single crystals owing to the substrate-induced epitaxial force. For example, single crystalline $SrFeO_2$ and $LaNiO_2$ films with *c*-axis oriented infinite layer structure are grown on $SrTiO_3$ substrates through topotactic reduction using CaH_2 [76,77]. In addition, thin films prepared via topotactic reaction tend to be homogeneous and to have high crystallinity. Indeed, $La_2CuO_{4+\delta}$ thin films, obtained via topotactic oxidation, exhibit superconductive behavior with T_c of 52 K, which is higher as compared to bulk one ($T_c \leq$ 45 K) [78]. In addition, epitaxial strain can also affect the local anion arrangement. Recently, Bouilly *et al*. used the topotactic reaction to synthesize the 214-type $LaSrCoO_{4-x}H_x$ thin film and reported that it had a disordered hydride/oxide ion arrangement, in contrast to the bulk phase with completely ordered Co-H^- bonds parallel to only one axis [79]. Other expected advantages of topotactic reactions using thin film samples are

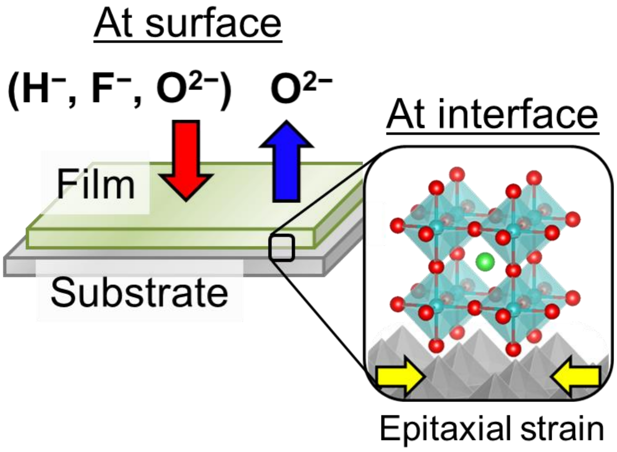

Figure 1-10. Two characteristics of thin film samples: large surface area/volume ratio, and epitaxial strain from the substrate.

considerably higher reactivity than bulk samples owing to the larger surface area/volume ratio and stabilization of the perovskite-based framework arising from the epitaxial effect.

1.7 Purpose of this study

As mentioned above, topotactic reactions are very useful to control anions in transition metal oxides. Especially, the reactions on thin film samples would be a promising method to synthesize new mixed anion compounds, such as oxyhydrides and oxyfluorides, and to expand the range of oxygen content in the oxides because of the two characteristics of thin films: the large surface area/volume ratio and epitaxial effect from substrate. In order to expand the availability of topotactic reactions, in this study, I attempted four types of topotactic reactions on perovskite transition metal oxide thin films: topotactic hydridation of $SrCoO_{2.5}$ and $SrVO_3$ films using CaH_2 (in Chapter 3), topotactic fluorination of $SrFeO_{3-\delta}$ and $SrCoO_{2.5}$ films using PVDF (in Chapter 4), topotactic reduction of $SrFeO_{3-\delta}$ and $Sr_{1-x}Sm_xFeO_{2.5}$ films using CaH_2 (in Chapter 5), and topotactic oxidation/reduction of $YBaCo_2O_x$ films using NaClO and CaH_2, respectively (in Chapter 6), and investigated the properties.

Chapter 2 Experimental techniques

2.1 Sample preparation

In this study, thin film samples were prepared by two steps: fabrication of precursor oxide thin films and topotactic reaction on the precursors. The precursor oxide thin films were grown on single-crystalline substrates by using pulsed laser deposition methods. The obtained precursor films were further subjected to topotactic hydridation and fluorination reactions by using CaH_2 and polyvinylidene fluoride, respectively. On the other hand, topotactic reduction and oxidation were conducted by reacting the precursor films with CaH_2 and NaClO, respectively.

2.1.1 Pulsed laser deposition [80,81]

Pulsed laser deposition (PLD) is a physical vapor deposition technique for fabricating high quality thin films, including oxides and hetero-structure films. Figure 2-1(a) shows a schematic image of the PLD apparatus. There are mainly four parts: (1) ultraviolet pulsed laser with high energy density, (2) a ceramic pellet (PLD target), (3) vacuum chamber, and (4) a substrate. During the PLD process, the PLD target is ablated by the pulsed laser, resulting in generation of plasma which is composed of species of the PLD target. When the plasma reaches to the surface of the substrate, the species in the plasma deposit as a thin film. The main advantage of PLD equipped with high vacuum system is that the cation ratio of the deposited film is usually the same as that in the PLD target and the amounts of impurity atoms are rather small.

In this work, I used fourth harmonic of a Nd-YAG laser (wavelength λ = 266 nm) and a KrF excimer laser (λ = 248 nm) for target ablation. Temperature at substrate could be controlled up to 1000ºC by semiconductor laser heating from backside of substrate. Pressure could be controlled precisely by introducing oxygen gas via variable leak valve, where the back pressure during film fabrication was about 10^{-7} Torr.

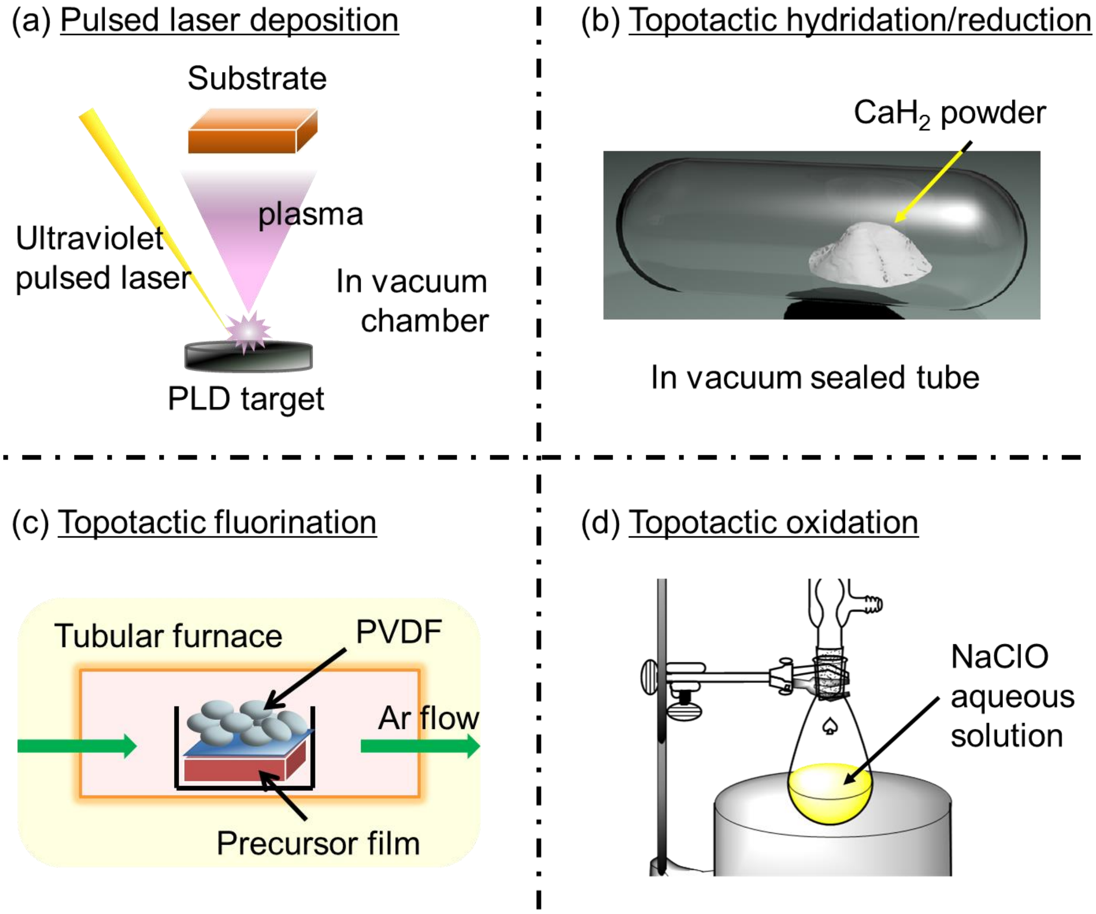

Figure 2-1. Schematic illustrations of (a) pulsed laser deposition and topotactic (b) hydridation/reduction, (c) fluorination and (d) oxidation.

2.1.2 Topotactic hydridation using CaH_2 [54]

Topotactic hydridation is a technique to dope hydride anions into oxide materials maintaining the cation frameworks (see Chapter 1.2). In this work, I used CaH_2 powder (Wako Pure Chemical Industries, Ltd.) as a source of hydride anions. CaH_2 was handled in a glovebox, because it is unstable in air. The chemical reaction between a perovskite ABO_3 and CaH_2 is formulated as:

$$ABO_3 + x\,CaH_2 \rightarrow ABO_{3-x}H_y + x\,CaO + (x - y/2)\,H_2$$

Thus, CaO and H_2 are yielded as the byproducts of the topotactic hydridation using CaH_2. The reaction is conducted in an evacuated sealed tube to prevent a reaction between CaH_2 and air.

Figure 2-1(b) shows a schematic illustration of the topotactic hydridation process using CaH_2 in this work. A precursor oxide thin film was embedded in CaH_2 powder and heated at 100–700 °C for 24 h in an evacuated sealed tube. As the evacuated sealed tubes, Pyrex and Quartz tubes were used when the reaction temperature was below 400 °C and above 450 °C, respectively. After the CaH_2-treatment, the films were rinsed by ethanol or 2-butanone to remove unreacted CaH_2 powder.

2.1.3 Topotactic fluorination using polyvinylidene fluoride [23]

Topotactic fluorination is a technique to dope fluoride anions into oxide materials maintaining the cation frameworks (see Chapter 1.3). In this work, I used polyvinylidene fluoride (PVDF, monomer unit CH_2CF_2, Fluorochem Ltd.) as a fluoride source. PDVF is stable in air and has a melting temperature of ~170 °C. The chemical reaction between a perovskite ABO_3 and PVDF is:

$$ABO_3 + y/2\ CH_2CF_2 \rightarrow ABO_{3-x}F_y + (3y/2 - x)\ C + y/2\ H_2O + (x - y/2)\ CO$$

Thus, C, H_2O and CO are generated as the byproducts of the topotactic fluorination using PVDF.

Figure 2-1(c) shows a schematic illustration of the topotactic fluorination process using PVDF in this work. A precursor oxide film was heated with 1–2 mm-size PVDF pellets at 100–450 °C for 12–24 h under Ar gas flow. In order to reduce adhesion of carbon impurities on the sample surface, the film was covered with Al foil during the reaction so as not to contact with PVDF directly.

2.1.4 Topotactic reduction using CaH_2 [54]

Topotactic reduction is a technique to introduce oxygen vacancies into oxide materials maintaining the cation frameworks (see Chapter 1.4). In this work, CaH_2 powder was used as a reducing agent. The chemical reaction between a perovskite ABO_3 and CaH_2 is:

$$ABO_3 + x\ CaH_2 \rightarrow ABO_{3-x} + x\ CaO + x\ H_2$$

CaH_2 was also used as a hydride source. The method of topotactic reduction using CaH_2 was the same as the topotactic hydridation. Thus, see Chapter 2.1.2 for detail of topotactic reduction using CaH_2.

2.1.5 Topotactic oxidation using NaClO [72]

Topotactic oxidation is a technique to introduce oxide anions into oxide materials maintaining the cation frameworks (see Chapter 1.5). In this work, I used NaClO solution (Wako Pure Chemical Industries, Ltd.) as an oxidizing agent. Because NaClO is easily decomposed into NaCl and O_2 by light, NaClO solution needs be handled in a dark place. In NaClO solution, three species (Cl_2, HOCl, and OCl^-) are in equilibrium as follows [82]:

$$OCl^- + H^+ \leftrightarrow HOCl\ (pK_a = 7.5 \text{ at } 25\ ^\circ C)$$

$$HOCl + H^+ + Cl^- \leftrightarrow Cl_2 + H_2O$$

The ratio of Cl_2, HOCl, and OCl^- can be controlled by pH; Cl_2, HOCl, and OCl^- are dominant when $pH < 1$, $2 < pH < 7$, and $8 < pH$, respectively. Because Cl_2 easily vaporizes, HOCl and OCl^- are usually used as oxidizing agents. Especially, HOCl has strong oxidizing power. pH value of the NaClO solution can be adjusted by adding HCl solution, while that of the commercial one is about 9. The chemical reaction between an oxygen vacant perovskite ABO_{3-x} and NaClO is:

$$AB\mathrm{O}_{3-x} + x\,\mathrm{NaClO} \rightarrow AB\mathrm{O}_3 + x\,\mathrm{NaCl}$$

Figure 2-1(d) shows a schematic illustration of the topotactic oxidation process using NaClO in this work. Precursor oxide films were annealed in NaClO solution at 25–80 °C for 20–80 h with pH of 6–9. The commercial NaClO solution (effective Cl concentration 5%) was diluted 2.5 times with water.

2.2 Crystallography analysis

2.2.1 X-ray diffraction [83]

X-ray diffraction (XRD) is a well-established technique for structural investigation of inorganic materials, including oxides. In XRD measurements, X-ray beam with constant wavelength (λ) is directed onto a sample. If the sample is crystallized, the X-ray is diffracted by the atomic layers of the crystal, resulting in a diffraction pattern according to the Bragg's law:

$$2d \sin\theta = n\,\lambda$$

where d is the distance of lattice plane, θ is the diffraction angle, n is an integer and λ is the wavelength of X-ray beam. From the peak position, intensity and shape of the XRD pattern, crystallographic information including lattice parameters and crystalline orientation can be obtained.

In this work, a four-axis diffractometer with Cu K_α radiation ($\lambda = 0.1542$ nm) was used for XRD measurements (Bruker D8 discover, Fig. 2-2). In this system, 2θ, ω, ϕ and χ angles can be adjusted, where ω is the angle between incident X-ray and sample, and χ and ϕ are the sample out-of-plane and in-plane tilting angles, respectively. Out-of-plane and in-plane lattice constants, crystalline orientation, and crystallinity of thin film samples were determined by using the following techniques:

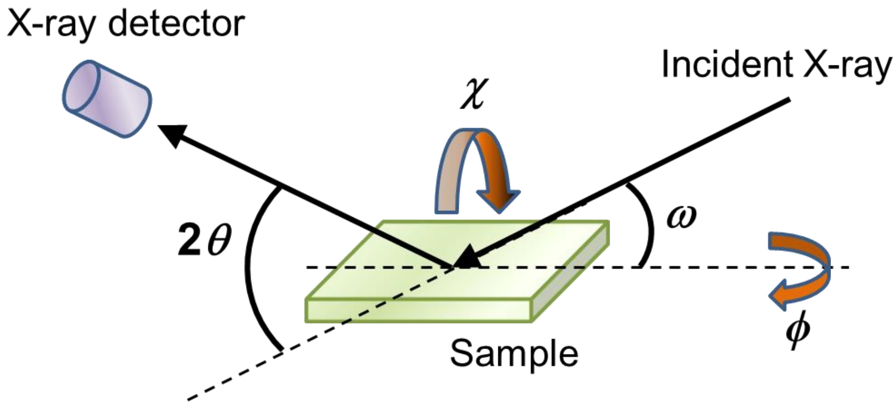

Figure 2-2. Schematic illustration of four-axis XRD apparatus.

- ✓ 2θ-θ XRD pattern: This is the most common XRD method to determine the lattice constants. It detects the intensity of the diffraction as a function of 2θ angle. In this mode, ω is set to be half of the 2θ angle, and χ is fixed. From the 2θ-θ XRD pattern, the distance of lattice plane, including out-of-plane and in-plane lattice constants, can be calculated according to the Bragg's law.

- ✓ 2θ-χ 2D XRD image: This is a method to determine the crystalline orientation of thin film samples. It detects the intensity of the diffraction from the sample with changing the 2θ, ω and χ angles. To observe diffraction patterns, the normal vector of the lattice plane should be in parallel with vector $\boldsymbol{a}$, which is defined as $\boldsymbol{a} = (\boldsymbol{b}/|\boldsymbol{b}|) - (\boldsymbol{c}/|\boldsymbol{c}|)$ where vectors $\boldsymbol{b}$ and $\boldsymbol{c}$ are the incident X-ray vector and the vector from an X-ray irradiated point on the sample to an X-ray detector, respectively. Thus, the crystalline orientation can be analyzed.

- ✓ Rocking curve: This is a method to determine the crystallinity of thin film samples. It detects the intensity of the diffraction with changing the ω angle. Usually, the 2θ and χ angles are fixed at out-of-plane XRD peak angle and 90°, respectively. If the sample has crystalline orientation, an intensity curve as a function of ω (rocking curve) is obtained. The full width at half maximum (FWHM) of the rocking curve corresponds to the crystallinity.

- ✓ Reciprocal space mapping (RSM): This is a method to determine the epitaxial relationship between a deposited film and the substrate. It detects the intensity of the diffraction from the sample with changing the 2θ, ω angles. The obtained 2θ-ω XRD patterns at various ω are usually converted into a reciprocal space map, which shows XRD intensity as a function of the reciprocal lattices q_x and q_z. Thus, epitaxial relationship is determined by comparing the q_x values between film and substrate.

2.2.2 Atomic force microscopy [84]

Atomic force microscopy (AFM) is a scanning probe technique for investigation of nano-scale surface morphology of samples. It scans a cantilever with a very sharp tip (AFM scanning tip). When the AFM scanning tip approaches to a sample surface, atomic force is acted between them according to Lennard-Jones potential:

$$V = A/r^{12} - B/r^{6}$$

where A and B are constants and r is the distance between AFM scanning tip and surface. In AFM measurements, the cantilever responses to the atomic force resulting in up or down motion of the cantilever depending on the sign of the force. This process is measured with moving the sample stage along the scanning direction and the distance r can be calculated, resulting in surface topography and roughness information.

In this work, commercial AFM apparatus (SPI-4000, Hitachi High-Technologies) was used with the lateral resolution of about 10 nm. The scanning area was in a range of $0.5 \times 0.5 - 10 \times 10$ μm^2.

2.2.3 Transmission electron microscopy [85]

Transmission electron microscopy (TEM) is a microscopic technique to observe the inner structure of samples. In TEM measurements, accelerated electrons are irradiated to a sample, and some of the electrons are transmitted through the sample. By detecting the density of the transmitted electrons depending on kinds of crystal structures and elements, structural images of the sample are obtained. To observe cross-sectional TEM images of thin film samples, they need be sliced thin enough for electrons to transmit by using techniques such as a focused ion beam method.

In this work, TEM measurements were performed by Kobelco Research Institute. Inc. The magnification of TEM images was in a range of 500,000 – 5,000,000 times.

2.2.4 Scanning electron microscope [86]

Scanning electron microscope (SEM) is a technique to observe the surface morphology of samples. In SEM measurements, accelerated electrons are irradiated to a sample, resulting in generation of secondary electrons, backscattered electrons, and characteristic X-ray from the sample. Generally, SEM images are obtained by detecting the secondary electrons because of the two characteristics; the escape depth of the secondary electrons is small, and the amount of the secondary electrons depends on an angle between the surface and the incident electron beam, which are advantageous to surface morphology observation.

In this work, SEM apparatus (JEOL Ltd., JSM-7100F) was used. The electron accelerating voltage was set to be in a range of 2.5–15 keV. The magnification of SEM images was in a range of 500 – 15,000 times.

2.2.5 Stylus surface profiler

Thickness of thin film samples can be determined by using a stylus surface profiler. In the measurements, a tip in contact with a sample surface was moved in lateral directions. By detecting the vertical movement of the tip, a difference in height between surface of the film and that of the substrate, i.e., thickness of the film is determined.

In this work, a commercial stylus surface profiler (Bruker, Dektak) was used for thickness determination.

2.3 Composition analysis

2.3.1 Energy dispersive X-ray spectroscopy [87]

Energy dispersive X-ray spectroscopy (EDS) is a measurement technique for chemical composition. There are mainly three parts in EDS equipment: an accelerated electron generator, a sample stage and an X-ray detector. In EDS measurements, accelerated electrons with energy of 1–25 keV are directed onto a sample. The accelerated electrons eject an inner-shell electron of the constituent element in the sample, yielding an electron hole where the electron was. When an outer-shell electron fills the hole, characteristic X-ray from the element is emitted. By detecting the energy and intensity of the characteristic X-ray, the chemical composition is determined.

In case of thin film samples, the penetration depth of EDS should be considered because it tends to be longer than the thickness of the film. The penetration depth as a function of energy can be calculated by using a Monte Carlo simulation of electron trajectory in solids [88]. For example, Figs. 2-3(a) and 2-3(b) show the calculated depth dependence of fluorescence radiation of Sr $L\alpha$, Fe $L\alpha$, Fe $K\alpha$, O $K\alpha$, and F $K\alpha$ for $SrFeO_2F$ with an electron accelerating voltage of 2.5 keV and 8 keV, respectively, where the intensity at the surface (0 nm) is set to 1. As shown in Fig. 2-3(a), the penetration depth of EDS for an electron accelerating voltage of 2.5 keV is about 50 nm, which is smaller than typical thickness of films in this work (50–90 nm). On the other hand, by using 8 keV as the electron accelerating voltage, the penetration depth of EDS is longer than the thickness of films, resulting in large signal from $SrTiO_3$ substrate. This suggests that oxygen content will be overestimated if 8 keV is used as the electron accelerating voltage. From the Monte Carlo simulation, EDS intensity ratio of elements can be calculated.

In this work, I used 2.5 keV as electron accelerating voltage to reduce any substrate contribution. The EDS is attached to the SEM apparatus (JEOL Ltd., JSM-7100F).

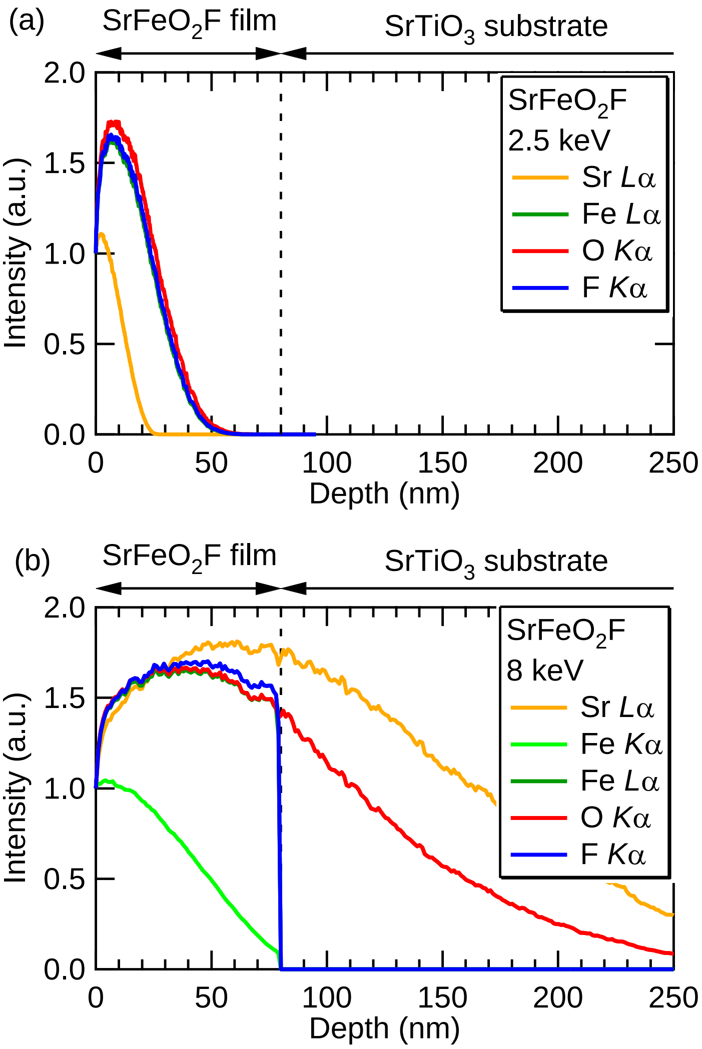

Figure 2-3. Depth profiles of fluorescence radiation of Sr *L*α, Fe *L*α, Fe *K*α, O *K*α, and F *K*α for $SrFeO_2F$ calculated assuming the electron accelerating voltage as (a) 2.5 keV and (b) 8 keV.

2.3.2 Secondary Ion Mass Spectrometry [87]

Secondary Ion Mass Spectrometry (SIMS) is a well-established measurement technique for determination of hydrogen content in samples. In the SIMS measurements, accelerated ion beam (such as Cs^+) is directed to a sample, resulting in sputtering the surface of the sample. By detecting the mass and the amount of the secondary hydrogen ions emitted from the sample, depth profile of hydrogen is determined.

In this work, SIMS measurements were carried out by Foundation for the Promotion of Material Science and Technology of Japan. H-implanted $SrTiO_3$ samples were used as standard references to determine the hydrogen content quantitatively.

2.3.3 Nuclear reaction analysis [89]

Nuclear reaction analysis (NRA) is a measurement technique for determination of fluorine content in samples. In NRA measurements, accelerated protons are directed to a sample, resulting in emission of α-ray and γ-ray from the sample according to $^{19}F(p, \alpha\gamma)^{16}O$ resonant nuclear reaction [90]:

$$^{19}\mathrm{F} + \text{proton } (p) \rightarrow {}^{16}\mathrm{O} + \alpha\text{-ray} + \gamma\text{-ray (902 keV)}$$

By detecting the γ-ray intensity, the fluorine amount in the sample is determined. Notably, the penetration depth of the accelerated protons is much larger than the thickness.

In this work, NRA measurements were performed by using 1 MV Tandetron accelerator at Tandem Accelerator Complex, University of Tsukuba. For quantitative measurements of the fluorine content, a CaF_2 single crystal was used as a reference.

2.3.4 Elastic recoil detection analysis [89]

Elastic recoil detection analysis (ERDA) is an ion beam analysis technique to determine oxygen content in samples. In ERDA measurements, accelerated Cl^- ion beam is directed to a sample, resulting in emission of atoms from the sample due to the elastic recoil. The energy of the emitted atom (recoil atom), E_2, is given as follows:

$$E_2 = \frac{4m_1m_2}{(m_1 + m_2)^2} E_1\cos^2\emptyset$$

where E_1 is the energy of the incident ion, m_1 and m_2 are the masses of the incident ion and recoil atom, respectively, and ϕ is the recoil angle. In general, m_2 should be lighter than m_1 for ERDA measurements. In case of thin film samples, the incident ions lose their energy when the ions pass the sample, yielding a variation of E_1 as a function of depth. Thus, the energy of recoil oxygen atoms from the film and substrate is different. By detecting the energy, mass and number of recoil atoms, the difference of oxygen content between film and substrate can be determined.

In this work, ERDA measurements were performed by using Pelletron™ 5UD Accelerator at Micro Analysis Laboratory, Tandem accelerator, The University of Tokyo. Cl^- ion beam with 38.4 MeV was used as an ion beam.

2.3.5 Rutherford backscattering spectrometry [89]

Rutherford backscattering spectrometry (RBS) is an ion beam analysis technique to determine chemical composition in thin film samples. In RBS measurements, accelerated He^{++} ion beam is directed to a sample. When the incident ion collides with an atomic nucleus, the incident ion is backscattered. The energy of backscattered ion (E_1) is given as follows:

$$E_1 = \left\{ \frac{m_1 \cos\theta + \sqrt{{m_2}^2 - {m_1}^2 \sin^2\theta}}{m_1 + m_2} \right\}^2 E_0$$

where E_0 is the energy of the incident ion, m_1 and m_2 are the masses of the incident ion and collided nucleus, respectively, and θ is the scattering angle. In general, m_1 should be smaller than m_2 for RBS measurements. Similar to ERDA measurements, E_0 depends on depth. Thus, by detecting the energy of the backscattered ions, depth profile of the element concentration is determined.

In this work, RBS measurements were obtained by Foundation for the Promotion of Material Science and Technology of Japan. He^{++} ion beam with energy of 2.275 MeV was used as an ion beam.

2.4 Valence state and electronic structure analysis

2.4.1 Soft X-ray absorption spectroscopy [91]

Soft X-ray absorption spectroscopy (XAS) is an absorption spectroscopy technique for determining the electronic structure and local structure of samples. In XAS measurements, X-ray beam is directed to a sample with varying photon energy, and the magnitude of absorbed X-ray is measured as a function of photon energy. The X-ray absorption is associated with the excitation of inner shell electrons which have characteristic energies specific to each element. Thus, from the position and shape of the XAS spectrum, oxidation state, spin state, and local structure of each element are determined. The photon energy is in a range of 0.1–2 keV, resulting in a smaller penetration depth than typical thickness of films in this work (50–90 nm).

In this work, the magnitude of X-ray absorption was detected by using two detection modes: total electron yield (TEY) and fluorescence yield (FY) mods. In the TEY mode, number of electrons emitted from the sample were counted. In the FY mode, the intensity of fluorescence from the sample were detected. In general, the TEY mode is surface sensitive, while the FY mode is bulk sensitive. The TEY-XAS measurements were conducted at the BL-2A beamline of Photon Factory, KEK. The FY-XAS measurements were performed at BL07LSU of SPring-8.

2.4.2 X-ray photoelectron spectroscopy [91]

X-ray photoelectron spectroscopy (XPS) is a spectroscopic technique to investigate the electronic structure and oxidation state of samples. In XPS measurements, X-ray beam is irradiated to a sample, resulting in emission of electrons from the sample. By detecting the number and kinetic energy of the emitted electrons, an XPS spectrum is obtained. The kinetic energy (E_k) is converted to the binding energy (E_b) from the Fermi energy (E_F) as follows:

$$E_b = h\nu - E_k - \Phi$$

where $h\nu$ is the X-ray photon energy and Φ is the work function related to the sample and instrument. When the X-ray photon energy is high, electronic states in core level can be detected as well as valence band structure. From the shape and peak position of the XPS spectrum, oxidation and bonding states of each element are determined.

XPS is a surface-sensitive technique. The penetration depth of XPS is a nanoscale order. Thus, by alternating XPS detection and sputtering of the surface, depth profile of element concentration is obtained.

In this work, XPS measurements were conducted at the BL-2A beamline of Photon Factory, KEK. XPS spectra were detected using a VG-SCIENTA SES-2002 electron-energy analyzer at a photon energy of 1,000 eV. XPS with Ar^+-ion sputtering is performed by using a commercial XPS system (PHI5000 VersaProbe, ULVAC-PHI) with monochromatized Al K_α radiation.

2.4.3 Ultra violet-visible-near infrared spectroscopy [87]

Ultra violet-visible-near infrared spectroscopy (UV-VIS) is a spectroscopic technique for investigating optical properties of samples. In UV-VIS measurements, reflectance (R) and transmittance (T) of a sample are recorded as functions of wavelength (λ). From the R and T values, extinction coefficient (k) can be calculated by using Murmann's method, which considers the multiple internal reflection effects [92]. The obtained k value was converted into the absorption coefficient (α) by using the relation as follows:

$$\alpha = \frac{4\pi k}{\lambda}$$

In general, the α value of a semiconductor sample obeys the following relation near bandgap (E_g):

$$(\alpha h\nu)^n \propto h\nu - E_g$$

where $h\nu$ is the photon energy and n is a constant. When the sample has a direct (or indirect) bandgap, n is 2 (or 1/2).

In this work, UV-VIS spectra were measured by using a UV-VIS spectrometer with λ = 250–2000 nm.

2.5 Magnetic and transport properties analysis

2.5.1 Electric resistivity measurement [93]

Two- and four-probe methods are well-established techniques to evaluate electrical resistivity of samples. Usually, the two-probe method is used for characterizing high-resistance samples, while the four-probe method is used for low-resistance samples. In these methods, electrical current (I) is applied between two electrodes, yielding voltage in the current-flow direction (V_{xx}). The relation of I and V_{xx} gives electrical resistivity (ρ) as follows:

$$\rho = \frac{V_{xx}}{I}\frac{wt}{L}$$

where w and t are the current path width and thickness, respectively, and L is the length between electrodes for voltage detection. Therefore, resistivity of the film is determined by detecting the voltage value as a function of current. The electrodes for voltage detection are the same as those for current injection for the two-probe method, but are different for the four-probe method.

In this work, resistivity was determined as a function of temperature and magnetic field in ranges of 2–300 K and ±9 T, respectively, by using physical properties measurement system (PPMS, Quantum Design) apparatus.

2.5.2 Hall effect measurements [93]

Hall effect measurement is an electrical technique to characterize transport properties, including carrier type, carrier density and mobility. In Hall effect measurements, electrical current [$\boldsymbol{I}$ = (I_x, 0, 0)] is applied along the x direction under a magnetic field [$\boldsymbol{B}$ = (0, 0, B_z)] in the vertical (z) direction. The moving charges are affected by a magnetic field according to the Lorentz force law, yielding voltage in the y direction (Hall voltage, V_H) as follows:

$$V_\mathrm{H} = \frac{I_x B_z}{nqt} = R_\mathrm{H} \frac{I_x B_z}{t}$$

where n and q are the carrier density and the charge of carrier, respectively, t is the thickness of the sample, and R_H is the Hall coefficient. By plotting V_H/I_x against B_z, carrier type, carrier density and Hall mobility (μ) can be determined where μ is calculated as:

$$\mu = \frac{1}{nq\rho}$$

where ρ is the electrical resistivity.

In this work, the Hall effect measurements were performed as a function of temperature and magnetic field in ranges of 2–300 K and ±9 T, respectively, by using PPMS apparatus.

2.5.3 Superconducting quantum interference device [94]

Superconducting quantum interference device (SQUID) magnetometer is a device to evaluate magnetization of samples. This contains a superconducting ring with two Josephson junctions. In the measurement, steady bias current is applied to the device. When the magnetic flux through the ring changes by moving the sample position, output voltage changes due to the Josephson effect. By detecting the change of voltage, the magnetization of the sample can be determined.

In this work, the SQUID measurements were performed by using magnetic properties measurement system (MPMS, Quantum Design) apparatus. Temperature and magnetic field can be controlled in ranges of 2–300 K and ±9 T, respectively. Magnetization value of thin-film sample (in units of μ_B/formula unit) was determined from the obtained magnetization value, the number of unit cells in the sample, and the substrate magnetization.

2.6 Density functional theory calculation [95]

Density functional theory (DFT) calculation is a well-established computational technique to predict crystal structure and electronic structure of metal oxides. In the calculation, electron density with minimized energy is calculated from initial structure and interactions according to Kohn and Hohenberg theorems and set of Kohn-Sham equations.

In this study, DFT calculations were performed using the Vienna *ab initio* simulation package [106]. The Perdew–Burke–Ernzerhof functional of the generalized gradient approximation (GGA) was adapted with a Hubbard +*U* term.

Chapter 3 Topotactic hydridation: perovskite $SrCoO_xH_y$ and $SrVO_2H$ films

3.1 Introduction

Recently, substitution by a hydride anion (H^-) has gained considerable attention as a new technique for changing the electrical and magnetic properties of transition metal oxides through the construction of new cation-anion networks and anion-ordered structures. The analogous H^- substitution into perovskite transition metal oxides has also been conducted, resulting in two types of oxide/hydride ion arrangements; randomly disordered oxide/hydride ion arrangements were observed in $BaTiO_{2.4}H_{0.6}$ [15] and $SrCrO_2H$ [16], and a one-dimensionally ordered V-H^--V bond network was discovered in $SrVO_2H$ [12]. So far, however, Co oxyhydrides with non-layered perovskite structure have not been synthesized due to their inherently less-stable frameworks.

In general, topotactic reactions for thin film samples have two advantages: considerably higher reactivity than bulk samples owing to the larger surface area/volume ratio, and stabilization of the perovskite-based framework arising from the epitaxial effect. Thus, the topotactic introduction of hydrogen into precursor cobalt oxide thin films on appropriate substrates using CaH_2 is a promising synthetic route for obtaining this type of cobalt oxyhydride. However, a previous attempt by Ichikawa *et al.* [96] to dope hydrogen into a $SrCoO_{2.5}$ film deposited on a $(La_{0.3}Sr_{0.7})(Al_{0.65}Ta_{0.35})O_3$(001) (LSAT) substrate resulted in the film becoming amorphous upon CaH_2 treatment.

In this chapter, I present the topotactic hydridation synthesis of new $SrCoO_xH_y$ films with a non-layered perovskite structure. Brownmillerite $SrCoO_{2.5}$ films grown on a $SrTiO_3$ (001) (STO) substrate were used as the precursors for topotactic hydrogen doping by CaH_2. The cation framework in the obtained films was maintained during the reaction, owing to the epitaxial stabilization effect. It was found that the perovskite lattice is orthorhombically distorted, indicating that the doped hydride ions form a Co-H^--Co two-dimensional (2D) network, in contrast to other reported perovskite oxyhydrides, $SrMO_{3-x}H_x$ (M = Cr, Ti, V). The electrical resistivity and band gap energy were also investigated and compared to those of the $SrCoO_{2.5}$ precursor film. In addition, I also present topotactic synthesis of single crystalline $SrVO_2H$ films on STO substrates. The doped H^- anions formed 1D ordered V-H bond along the out-of-plane direction because of the epitaxial strain. The synthesis temperature could be lower by reducing thickness of films.

3.2 Method

3.2.1 Method for $SrCoO_xH_y$ films

Precursor $SrCoO_{2.5}$ films were grown on STO (Shinkosha Co.) substrates through the PLD technique. A $SrCoO_{3-\delta}$ ceramic pellet (20 mm in diameter and 5 mm in thickness, Toshima Manufacturing Co.) was used as a target. The fourth harmonic of a Nd-YAG laser (wavelength $\lambda = 266$ nm) with an energy of 0.3 $J\cdot cm^{-2}$/shot and repetition rate of 10/3 Hz was employed to ablate the target. Substrate temperature and oxygen partial pressure were kept at 700 °C and 5×10^{-6} Torr, respectively, during each deposition run. The obtained $SrCoO_{2.5}$ precursor films were further subjected to the solid-phase reaction using ~0.2 g CaH_2 powder at 250 °C for 24 h in evacuated Pyrex tubes. The surface of the obtained films was washed with 2-butanone to remove any unreacted CaH_2. The typical film thickness measured by a stylus surface profiler was 50–60 nm.

Crystal structures of the films were examined by an X-ray diffractometer equipped with a 2D detector using Cu $K\alpha$ radiation. The amount of hydrogen in the films was estimated by dynamic SIMS with a depth resolution of ~10 nm. For quantitative measurements of the hydrogen content, H-implanted $SrTiO_3$ samples were used as standard references. The oxygen content in the films was estimated using an EDS fitted with a scanning electron microscope, which was operated at an electron accelerating voltage of 2.5 keV to reduce any substrate contribution. The oxidation states of the Co ions in the films were determined from XAS measurements at the Co *L*-edges in fluorescence yield (FY) mode, which were performed at BL07LSU of SPring-8. All the FY spectra were measured with a silicon drift detector at room temperature. The electrical resistivity and optical band gap were measured by the conventional two-probe method and ultraviolet-visible spectrometry, respectively.

3.2.2 Method for $SrVO_2H$ films

Perovskite $SrVO_3$ thin films were fabricated on STO substrates by using PLD technique. A $SrVO_3$ ceramic pellet, used as a target, was ablated by a KrF excimer laser with ~2 J/cm^2/shot and a 2 Hz repetition rate. The substrate temperature, and oxygen partial pressure were kept at 900 °C, and 5×10^{-7} Torr, respectively, during each deposition run. The precursor film thicknesses measured by a stylus surface profiler was about 15 and 55 nm. The obtained $SrVO_3$ precursor films were further reacted with CaH_2 powder at temperature ranges (T_r) of 250-700 °C for 24 h in vacuum sealed quartz glass tubes. After the reaction with CaH_2, the films prepared below T_r = 450 °C were washed with ethanol to remove unreacted CaH_2, while the films prepared above T_r = 500 °C were rinsed in water to remove both unreacted CaH_2 and CaO layers which were formed on the films.

Crystal structures of the films were examined by an X-ray diffractometer using Cu $K\alpha$ radiation. Hydrogen content in the films was estimated by dynamic SIMS, where H-implanted $SrTiO_3$ samples were used as a standard references. The XAS measurements were conducted at the BL-2A beamline of Photon Factory, KEK, by using the total electron-yield method at room temperature. The XPS measurements were performed at BL47XU of SPring-8 with a photon-energy of 7940 eV. The Fermi levels of the samples were referred to that of Au foil in electrical contact with the samples.

3.3 Results and discussion

3.3.1 Synthesis of $SrCoO_xH_y$

Crystal structure analysis

Figure 3-1(a) shows the 2θ-θ X-ray diffraction (XRD) pattern at χ = 90° measured for the $SrCoO_{2.5}$ precursor film deposited on an STO substrate. The film exhibits the 006, 008, and 00$\underline{10}$ diffraction peaks corresponding to the brownmillerite structure, indicating that the $SrCoO_{2.5}$ precursor film has a *c*-axis-oriented brownmillerite structure, where CoO_4 tetrahedral and CoO_6 octahedral sub-layers are alternately stacked [97]. From the XRD reciprocal space map measurements for the 11$\underline{12}$ diffraction of the $SrCoO_{2.5}$ structure, the $SrCoO_{2.5}$ film was confirmed to be coherently grown on the STO substrate with $a/\sqrt{2} = b/\sqrt{2}$ = 0.3905 nm and $c/4$ = 0.3937 nm (cell volume = 0.06004 nm^3).

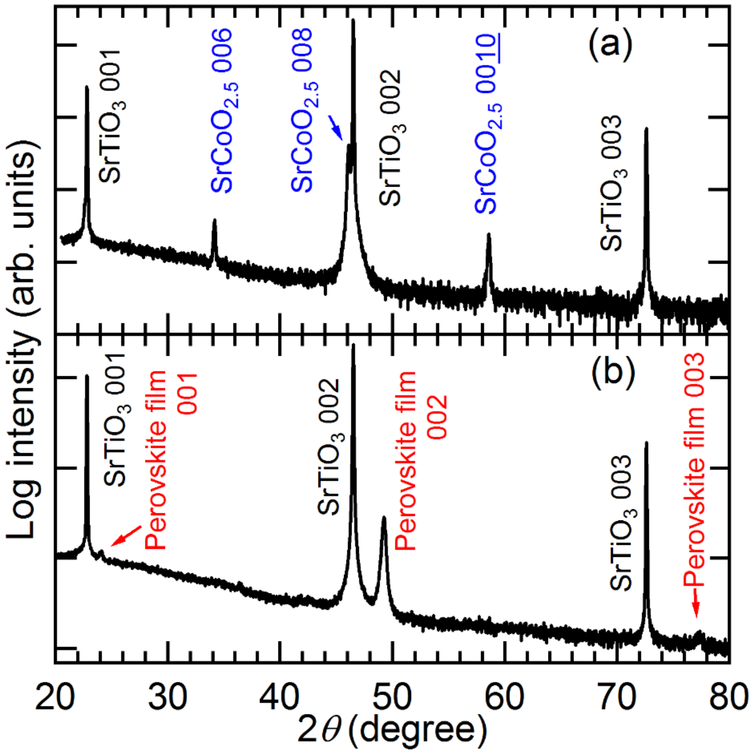

Figure 3-1. 2θ–θ XRD patterns of the (a) $SrCoO_{2.5}$ precursor and (b) CaH_2-treated films on STO (001) substrates.

Figure 3-1(b) shows the 2θ-θ XRD pattern at χ = 90° measured for the film after CaH_2 treatment. New diffraction peaks attributed to the 001, 002, and 003 diffraction of the perovskite structure are clearly observed at 2θ = 24.0°, 49.2°, and 77.3°, respectively, while the peaks corresponding to the brownmillerite $SrCoO_{2.5}$ disappeared. This proves that the crystalline phase is completely changed from brownmillerite to perovskite by CaH_2 treatment at 250 °C.

Figure 3-2 shows the 2θ-χ 2D XRD image around the STO 011 diffraction peak observed for the perovskite film after CaH_2 treatment. As can be seen from the figure, in addition to the STO 011 diffraction peak, 101 and 011 diffraction peaks appear at (2θ, χ) = (32.4°, 48.2°) and (34.3°, 45.0°), respectively. These peaks indicate that the film has an orthorhombic lattice with a = 0.416 nm, b = 0.370 nm, and c = 0.3702 nm. The estimated cell parameters are very different from those of the precursor $SrCoO_{2.5}$ or oxygen-vacant $SrCoO_{2.5-\delta}$ ($0.21 < \delta < 0.29$) with a cubic structure [98]. The cell volume of the obtained film is 0.0570 nm^3, which is somewhat smaller than that of the precursor film, 0.06004 nm^3. The χ value of the 101 peak is close to that of the 011 peak, indicating that the film

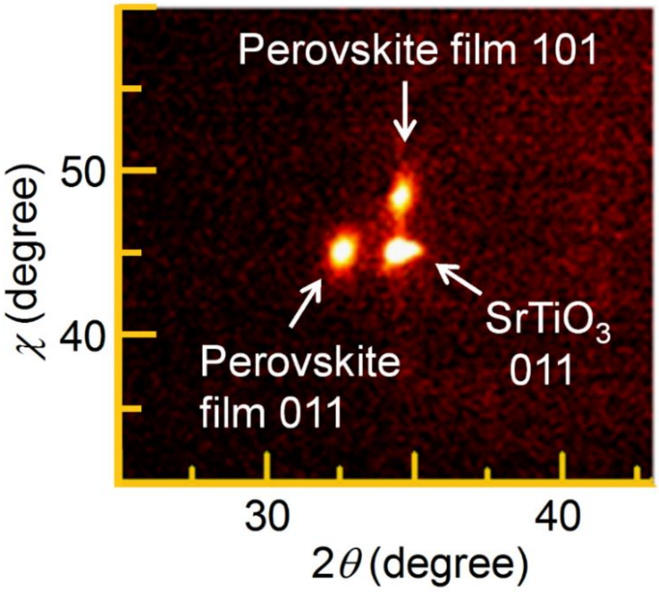

Figure 3-2. XRD image of a 2D 2θ-χ scan around the STO 011 diffraction peak of the CaH_2-treated film.

is composed of different domains with *a*-axes parallel to either STO [100] or STO [010], while the *c*-axes of all domains are aligned in the out-of-plane (STO [001]) direction. Furthermore, the calculated in-plane area of the unit cell for the CaH_2-treated film ($S = a \times b$) is 0.154 nm^2, which is close to that of the STO substrate (S = 0.1525 nm^2) but fairly larger than that of the LSAT substrate (S = 0.1497 nm^2). Therefore, these results suggest that the cation framework is maintained during the topotactic reaction with CaH_2 owing to epitaxial stabilization on the STO substrate.

Compositional analysis

To confirm hydrogen doping into the CaH_2-treated film, SIMS measurements were performed. Figure 3-3(a) shows dynamic SIMS depth profiles of H secondary ions in the $SrCoO_{2.5}$ precursor film and perovskite film after CaH_2 treatment. The average concentration of hydrogen (n_H) in the latter film is ~2.1 × 10^{22} atom cm^{-3}, which is approximately two orders of magnitude higher than that in the former (n_H ~6 × 10^{20} atom cm^{-3}), verifying that the film was doped with hydrogen during the CaH_2 treatment. The n_H of the CaH_2-treated film corresponds to y ~1.2 atom/unit cell for $SrCoO_xH_y$, although the H ion densities determined by using the H-$SrTiO_3$ standards have some uncertainty owing to the chemical matrix effect. Interestingly, this n_H is equivalent to those of bulk $BaTiO_{2.4}H_{0.6}$ (n_H ~9 × 10^{21} atom cm^{-3}) and bulk $SrVO_2H$ (n_H ~1.8 × 10^{22} atom cm^{-3}), and higher than those of bulk layered cobalt oxyhydrides, $LaSrCoO_3H_{0.7}$ (n_H ~4 × 10^{21} atom cm^{-3}) and $Sr_3Co_2O_{4.33}H_{0.84}$ (n_H ~3 × 10^{21} atom cm^{-3}) [9,12,14,15]. Figure 3-3(b) shows the EDS spectra for the precursor and CaH_2-treated films. The oxygen content x in the $SrCoO_xH_y$ film was roughly estimated as 1.6 ± 0.3 from the peak area ratio of the O Kα/Co Lα peaks by simulating the electron trajectory using the Monte Carlo method [88]. This value is much smaller than that of the $SrCoO_{2.5}$ precursor film, x ~2.5, suggesting that oxygen ions were removed during the CaH_2 treatment simultaneously with the insertion of hydrogen. Thus, it is naturally assumed that the doped hydrogen atoms occupy the oxygen sites in the perovskite $SrCoO_3$ and exist as H^-.

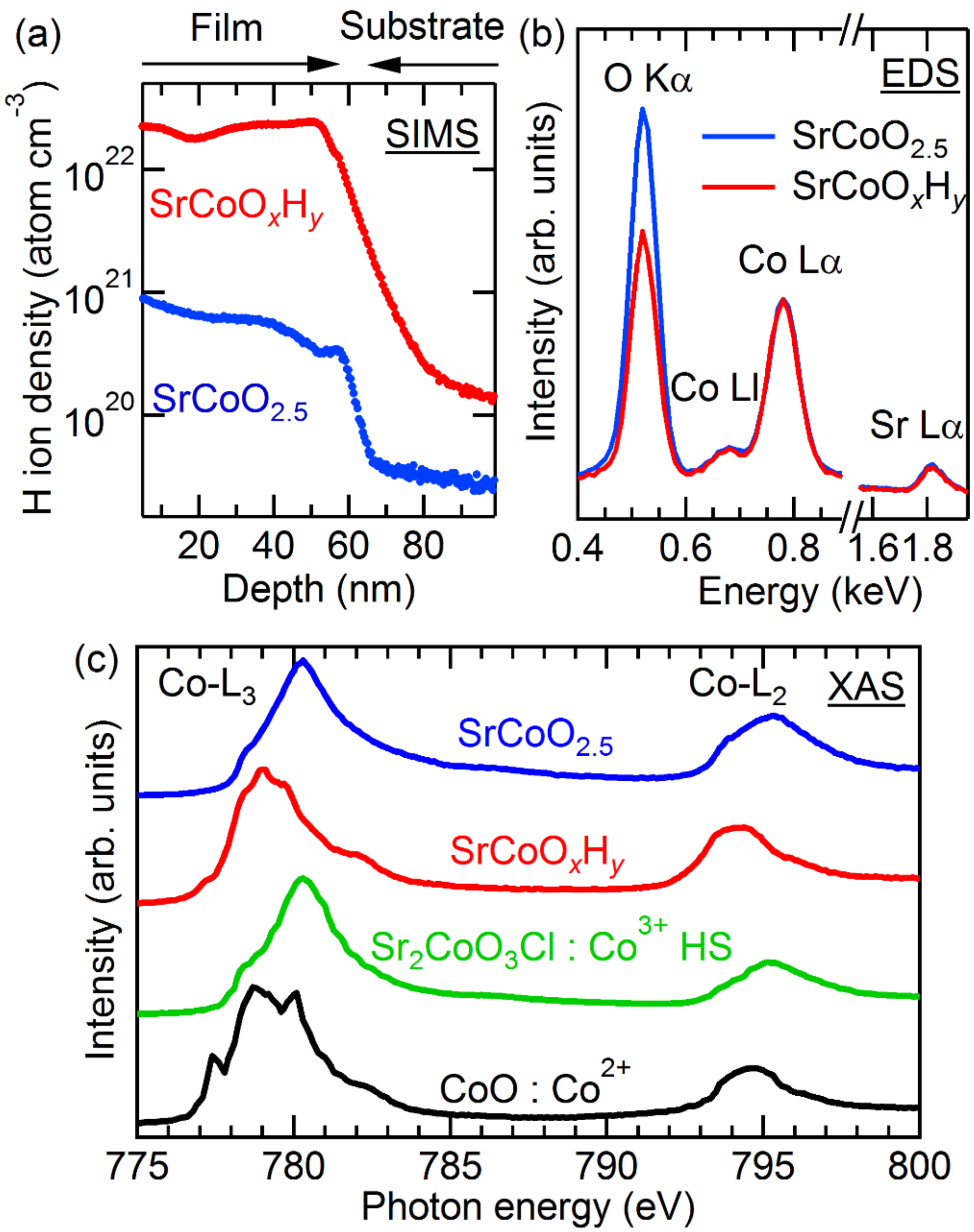

Figure 3-3. (a) Dynamic SIMS depth profiles of H secondary ions and (b) EDS spectra for the precursor and CaH$_2$-treated films on STO (001) substrates. (c) Co L$_{2,3}$-edge XAS spectra of the precursor SrCoO$_{2.5}$ and SrCoO$_x$H$_y$ films obtained in the FY mode, and the relevant spectra of Sr$_2$CoO$_3$Cl (Co^{3+} HS state) and CoO (Co^{2+}) [99].

Oxidation state analysis

In order to investigate the oxidation states of Co ions in the $SrCoO_xH_y$ film, I performed Co $L_{2,3}$-edge XAS measurements in the bulk-sensitive FY mode. Figure 3-3(c) shows the Co $L_{2,3}$-edge XAS spectra of the precursor $SrCoO_{2.5}$ and $SrCoO_xH_y$ films with Sr_2CoO_3Cl as a high-spin (HS) Co^{3+} reference and CoO as a Co^{2+} reference [99]. Each spectrum has peaks around 780 eV and 795 eV, which correspond to the Co L_3 and Co L_2 edges, respectively. By comparing the spectrum of the precursor $SrCoO_{2.5}$ film with that of the reference, I determined the Co oxidation states in the film to be HS trivalent. On the other hand, the spectrum of the $SrCoO_xH_y$ film is similar in peak position to the referenced spectrum of CoO, proving that Co^{2+} ions are dominant in the film.

State and position of hydrogen ions

Based on the SIMS, EDS, and XAS results, I discuss the chemical state of hydrogen in the $SrCoO_xH_y$ film. As mentioned above, the x and y values in the $SrCoO_xH_y$ film were estimated to be 1.6 ± 0.3 and 1.2 ± 0.2, respectively, from the SIMS and EDS measurements. In addition, the Co oxidation state of the film is roughly evaluated to be divalent from the XAS measurements. Thus, the oxidation state of hydrogen can be calculated to be negative, which suggest that the doped hydrogen exists as hydride ion (H^-). Based on the observations that hydrogen content is 1.2 ± 0.2 and the Co valence state is almost divalent, the oxygen content can be estimated to be 1.4 ± 0.1. If the hydrogen exists as proton (H^+), it follows that the Co ions must have an extremely low oxidation state of almost zero, which is obviously inconsistent with the XAS results.

I then discuss the local hydrogen arrangement in the $SrCoO_xH_y$ film with a perovskite structure. In transition metal oxyhydrides, the metal-H^- bond is known to be much shorter than the metal-oxygen bond, whereas the latter lengthens after hydride substitution [9-14]. For example, in the case of $LaSrCoO_3H_{0.7}$ having Co-H^--Co bonds parallel to the b-axis and Co-O^{2-}-Co bonds along the a and c-axes, the b-axis length decreases from 0.3805 to 0.3603 nm accompanied by a change in composition from

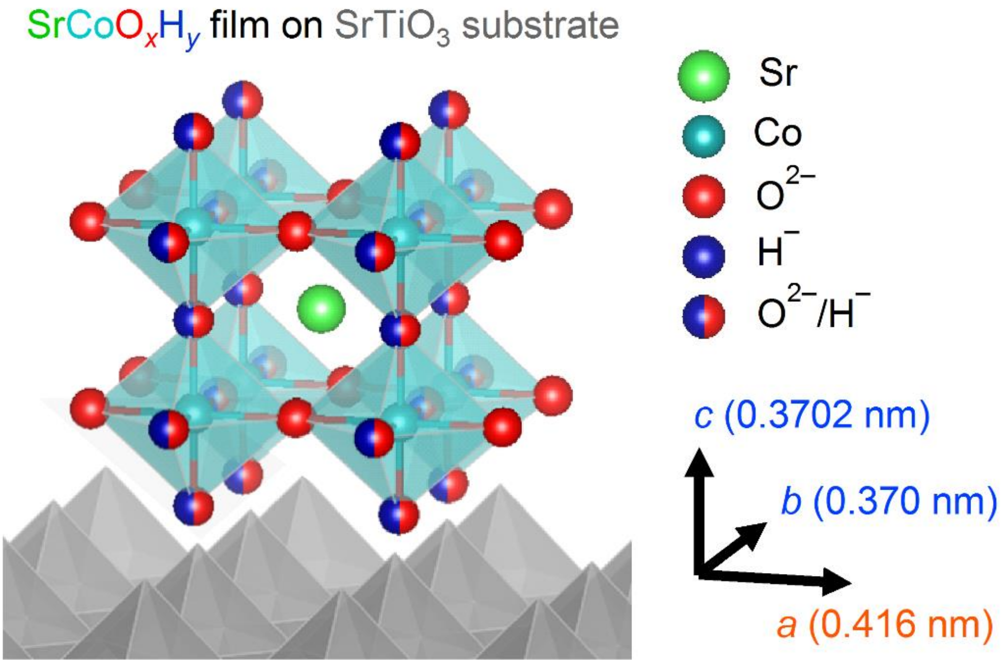

Figure 3-4. Expected crystal structure of the $SrCoO_xH_y$ film on an STO substrate (gray polyhedral).

$LaSrCoO_4$ to $LaSrCoO_3H_{0.7}$, while the a- and c-axis lengths increased from 0.3805 to 0.3871 nm and from 1.254 to 1.302 nm, respectively [10]. This $SrCoO_xH_y$ film is characterized by substantially longer a-axis (0.416 nm) and shorter b- and c-axes (0.370 and 0.3702 nm, respectively) than those of the precursor $SrCoO_{2.5}$ ($a/\sqrt{2} = b/\sqrt{2} =$ 0.3905 nm and $c/4 = 0.3937$ nm). This indicates that the Co-H^--Co bonds in the $SrCoO_xH_y$ film are extended parallel to the b- and c-axes, as illustrated in Fig. 3-4. In other words, the Co-H^--Co bonds form a 2D network. It is interesting to note that the presently proposed hydrogen arrangement forming the 2D Co-H^--Co bond network differs from those observed in other hydrogen-doped perovskite transition metal oxides, $AMO_{3-x}H_x$; in perovskite $SrVO_2H$, V-H^--V bonds form a one-dimensional (1D) chain-like structure, whereas in $BaTiO_{2.4}H_{0.6}$ and $SrCrO_2H$, M-H^--M bonds (M = Ti or Cr) are randomly distributed [12,15,16].

3.3.2 Properties of $SrCoO_xH_y$

The obtained $SrCoO_xH_y$ film was found to be insulating with a resistivity ρ of $>10^4$ Ωcm at 300 K, while the $SrCoO_{2.5}$ precursor film showed semiconducting behavior with $\rho(300\ K) = 18$ Ωcm. To explain the high ρ of the $SrCoO_xH_y$ film, the optical absorptance spectrum was measured, as shown in Fig. 3-5(a), where the absorptance is calculated as 1 – reflectance – transmittance. The $SrCoO_xH_y$ film shows a strong absorptance peak at ~2.3 eV, corresponding to the red color of the film. The optical band gap (E_g) was estimated by plotting $(\alpha h\nu)^2$ against the photon energy ($h\nu$), where the absorption coefficient α was calculated from the reflectance and transmittance spectra of the $SrCoO_xH_y$ film and STO substrate [92]. As shown in Fig. 3-5(b), the linear dependence of $(\alpha h\nu)^2$ on $h\nu$ suggests that $SrCoO_xH_y$ film has a direct band gap. The E_g of the $SrCoO_xH_y$ film was ~2.1 eV, which is much larger than that of $SrCoO_{2.5}$ film (E_g ~0.35 eV) [100]. Thus, the widened band gap is responsible for the extremely high electrical resistivity of the $SrCoO_xH_y$ film. The $SrCoO_xH_y$ film with Co^{2+} ($t_{2g}^5e_g^2$) has a large structural distortion with $a/c = 1.12$, owing to the oxide/hydride ordering. The structural

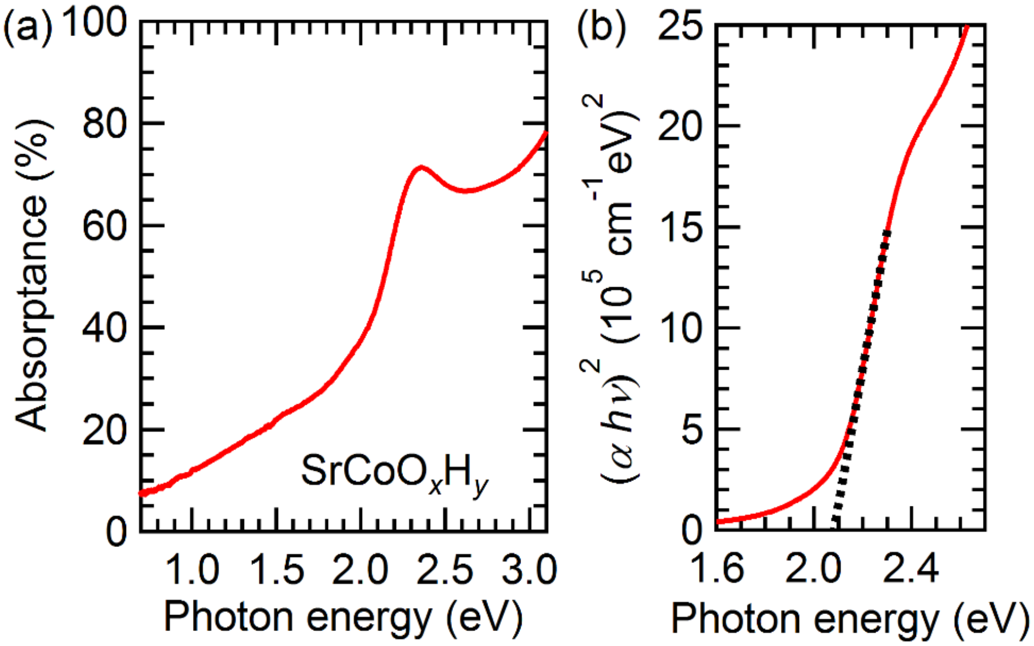

Figure 3-5. (a) Absorptance spectra of the $SrCoO_xH_y$ film. (b) $(\alpha h\nu)^2$ as a function of photon energy for the $SrCoO_xH_y$ film.

distortion would result in the opening of an energy gap between the occupied (d_{xy}, and d_{zx}) and unoccupied (d_{yz}) Co 3*d* states in the t_{2g} bands, which might partially account for the insulating characteristics of the $SrCoO_xH_y$ film.

3.3.3 Synthesis of $SrVO_2H$ films

Brief introduction of $SrVO_2H$

Recently, oxyhydride $SrVO_2H$ is synthesized from the parent oxide $SrVO_3$ via topotactic reaction using CaH_2 as shown in Fig. 3-6 [12]. In $SrVO_2H$, the doped H^- anions were coordinated in the axial positions of VO_4H_2 octahedral units, resulting in 1D ordered V-H^- bond networks. Because of the anion coordination, it has a tetragonal structure with a large a/c lattice ratio (a = 3.93, c = 3.66 Å). $SrVO_2H$ has a V $3d^2$ configuration, and the occupied d_{xz} and d_{yz} orbitals interact with not H 1*s* but O 2*p* orbitals because of the orbital symmetry effect [12,20]. This V 3*d* – O 2*p* bonding system in $SrVO_2H$ leads to strong antiferromagnetic coupling with Néel temperature above 300 K [12], and theoretical prediction that $SrVO_2H$ has a quasi-2D Mott insulator electronic structure [20].

Although there has been no report of thin film preparation of $SrVO_2H$, topotactic film synthesis techniques would produce two advantages. The first one is that single crystals can be obtained owing to the substrate-induced epitaxial effect. In order to realize

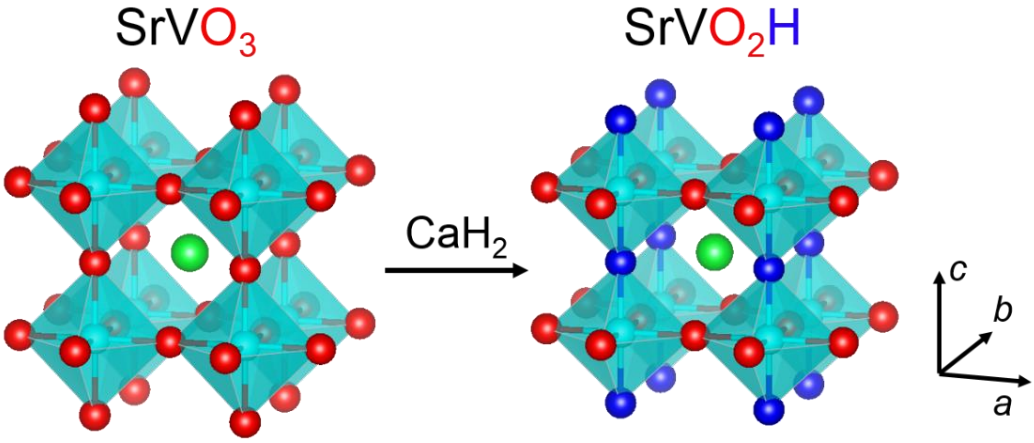

Figure 3-6. Crystal structures of $SrVO_3$ and $SrVO_2H$.

it, STO substrate (*a* = 3.905 Å) seems to be suitable for $SrVO_2H$, because it has a small lattice mismatch with *a* of $SrVO_2H$ (0.6%) but has a large lattice mismatch with *c* of $SrVO_2H$ (−6.3%), which would lead to aligned V-H^- bonds. The second advantage is the lowering of synthesis temperature due to the higher reactivity of thin film samples. As mentioned below, the synthesis temperature of bulk $SrVO_2H$, 610 °C, is so high that byproduct CaO layer is formed on the $SrVO_2H$ surface, resulting in failure of surface sensitive XPS and XAS measurements. Thus, lowering of the synthesis temperature is desired to investigate the electronic structure of $SrVO_2H$.

Crystal structure analysis

Figure 3-7(a) shows the 2θ–θ XRD pattern measured at $\chi = 90°$ for the $SrVO_3$ precursor film with a thickness of ~55 nm. The 002 XRD diffraction peak of perovskite structure proved that perovskite $SrVO_3$ precursor film was successfully obtained. The full-width half-maximum of the rocking curves for the 002 diffraction, $\Delta\omega(002)$, was 0.07°, indicating good crystallinity. From the XRD reciprocal space map measurements for 103 diffraction of the film, the $SrVO_3$ precursor film was confirmed to be coherently grown on STO substrate with *a* = 3.905 and *c* = 3.826 Å, similar to the previous report [101].

After reacting the precursor film on STO substrate with CaH_2 at $T_r = 600°C$, the 002 diffraction peak of $SrVO_3$ disappeared and a new peak appeared at $2\theta = 49.6°$ (Fig. 3-7(b)), which is assignable to 002 diffraction of $SrVO_2H$ ($2\theta = 49.9°$ in [12]). Figure 3-7(c) shows the RSM for the CaH_2-treated film. 103 diffraction peak of $SrVO_2H$ was clearly observed at $q_x = 2.55$ and $q_z = 8.15$ nm^{-1}, indicating that the film was epitaxial. From these peaks, the obtained film was calculated to have a tetragonal structure with *a* = 3.92 and *c* = 3.68 Å, which is close to bulk $SrVO_2H$ lattice (tetragonal with *a* = 3.93 and *c* = 3.66 Å [12]). Therefore, the obtained film was *c*-axis orientated $SrVO_2H$; i.e., the $SrVO_2H$ film possesses 1D ordered V-H bonds along the out-of-direction direction and VO_2 plane in the in-plane direction as illustrated in Fig. 3-6. This *c*-axis orientation is

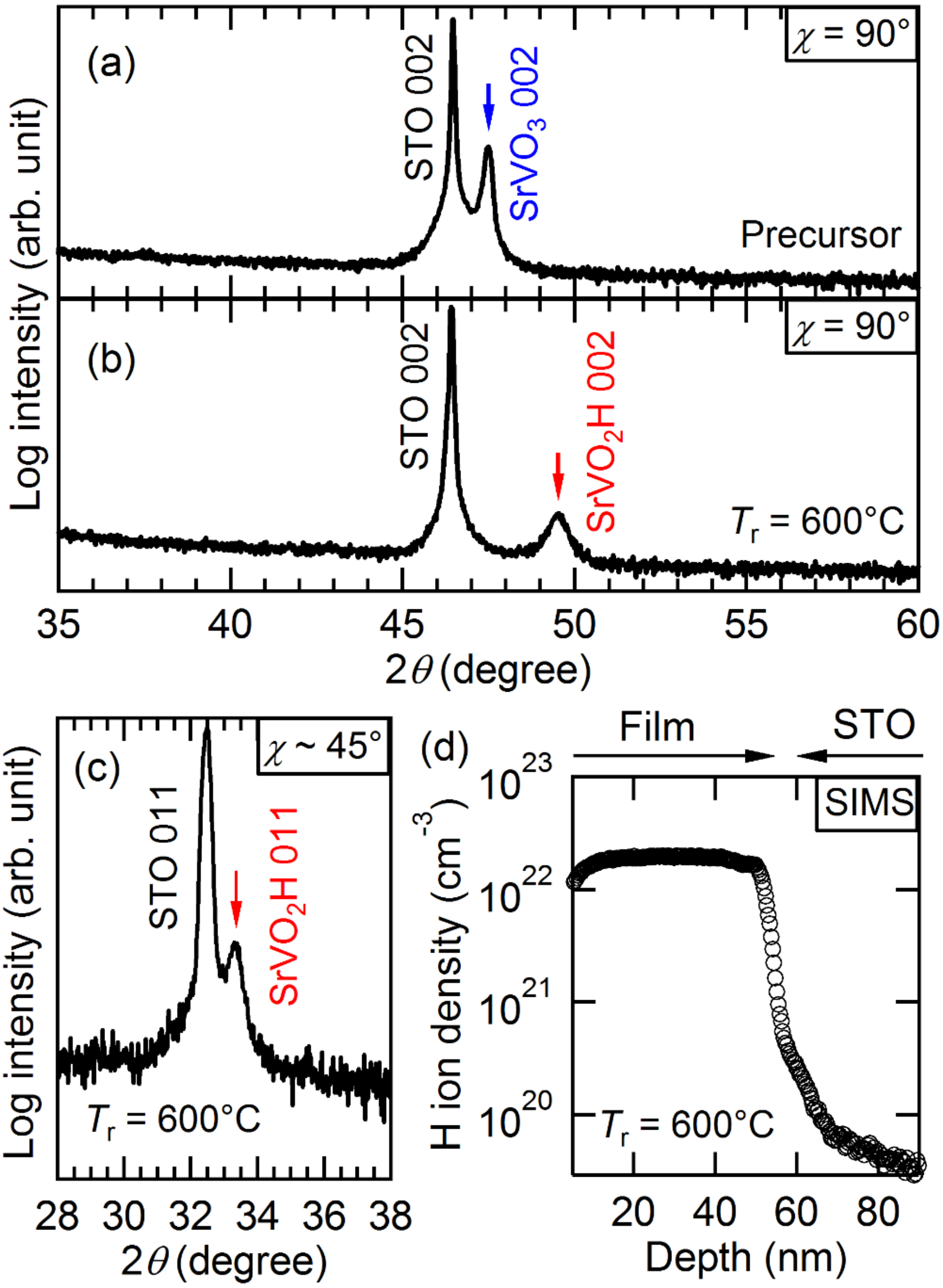

Figure 3-7. 2θ–θ XRD patterns measured at χ = 90° for (a) the ~55 nm thick $SrVO_3$ precursor film and (b) the $SrVO_2H$ film obtained by reacting the precursor with CaH_2 at T_r = 600 °C. (c) 2θ–θ XRD pattern measured at χ ~ 45° and (d) dynamic SIMS depth profile of H ions for the $SrVO_2H$ film.

reasonable because STO substrate has a small lattice mismatch with *a* of bulk $SrVO_2H$ (−0.6%) but has a large lattice mismatch with *c* of bulk $SrVO_2H$ (6.3%). The $\Delta\omega(002)$ value of the $SrVO_2H$ film was 0.26°, which was wider than that of the precursor.

In order to confirm the hydrogen doping in the film, SIMS measurement was performed. Figure 3-7(d) shows the SIMS depth profile of hydrogen ions for the $SrVO_2H$ film. Hydrogen ions were doped almost homogeneously in the film with the concentration of $\sim 1.9 \times 10^{22}$ atom/cm^3, which was much higher than that in STO substrate. The hydrogen concentration in the film was very similar to that of bulk $SrVO_2H$, $\sim 1.8 \times 10^{22}$ atom/cm^3, which also supports the formation of $SrVO_2H$.

Figure 3-8 shows the *c*-axis lengths as a function of T_r for the films prepared from the ~15 (black triangle) and ~55 (green square) nm thick $SrVO_3$ precursor films. For the ~55 nm thick films, the *c*-axis lengths increased from 3.826 to 3.85 Å with increasing T_r up on 350°C, probably due to the formation of oxygen vacancies in $SrVO_3$. This suggests that removal of oxygen ions from $SrVO_3$ occurred before hydride doping. At T_r

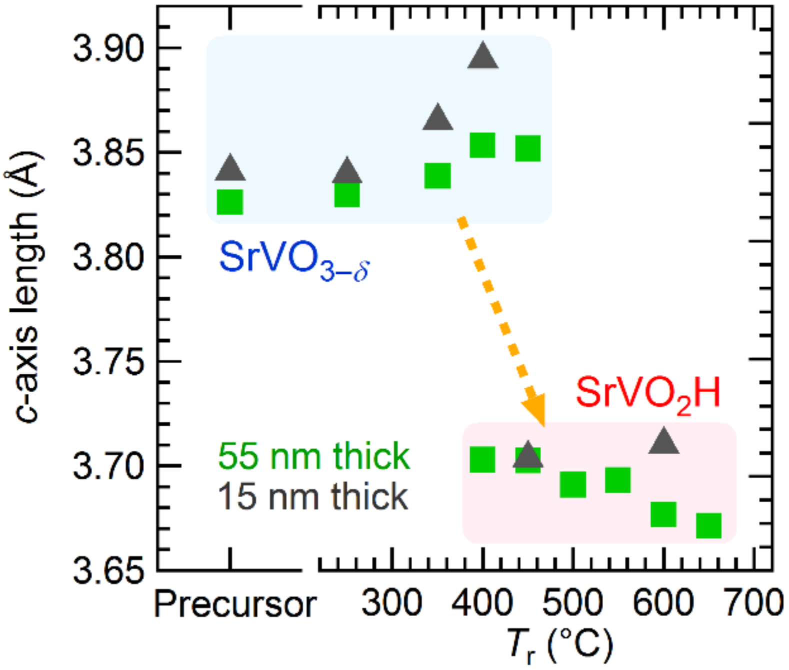

Figure 3-8. *c*-axis lengths for the films as a function of CaH_2-treatment temperature (T_r). The films were obtained from the $SrVO_3$ precursors with 55 (green square) and 15 (black triangle) nm thick.

= 400−450°C, *c*-axis oriented $SrVO_2H$ phase appeared, although a small amount of oxygen vacant $SrVO_{3-\delta}$ still remains. At T_r = 500−650°C, $SrVO_2H$ was obtained without $SrVO_{3-\delta}$ phase as shown in Fig. 2, while the films prepared at $T_r \geq$ 700°C became amorphous. Thus, the synthesis temperature of the ~55 nm thick $SrVO_2H$ film is in a range of 500–650°C. On the other hand, by decreasing the thickness to ~15 nm, single phase of $SrVO_2H$ was obtained at 450°C, which was lower as compared to the ~55 nm thick films ($T_r \geq$ 500°C) and the bulk ($T_r \geq$ 600°C). These results suggest that the synthesis temperature could be reduced by decreasing length of diffusion path.

The surface of the obtained $SrVO_2H$ films for both thicknesses was investigated. At $T_r \geq$ 450°C some MgO particles were formed on the film surface due to the reaction between CaH_2 and quartz glass tube, while at higher temperature, $T_r \geq$ 500°C, CaO layer was generated as a byproduct of CaH_2 and completely covered the $SrVO_2H$ film surface. Although, the CaO layer can be removed by washing with deionized water, surface oxidization occurs during the process and alters result of $SrVO_2H$ electronic structure. Therefore, the evaluation of electronic structure by surface sensitive measurements, XPS and XAS, was limited to the $SrVO_2H$ film with 15 nm thickness obtained at T_r = 450°C.

Oxidation state analysis

Figure 3-9(a) shows V 2*p* XAS spectra for the precursor $SrVO_3$ and $SrVO_2H$ films together with the spectra of $CaVO_3$ and YVO_3 as references of V^{4+} and V^{3+}, respectively [102]. The V L_3 and L_2 peaks were clearly observed in all spectra. The spectra of the $SrVO_3$ and $SrVO_2H$ films are very similar in peak shape and position to those of the $CaVO_3$ and YVO_3 references, respectively, proving that the vanadium oxidation states in the film changed from 4+ to 3+ after the topotactic reaction. From these results, the oxidation state of H in the $SrVO_2H$ film can be calculated to be –1, i.e., the doped H exists as hydride in the film. XPS is more surface-sensitive than XAS. Figure 3-9(b) shows V 2*p* XPS spectra for the $SrVO_3$ and $SrVO_2H$ films. The V $2p_{3/2}$ peak of the $SrVO_2H$ film was located at 515.3 eV, which is close to that of V_2O_3 (V^{3+}, 515.5 eV) rather than those

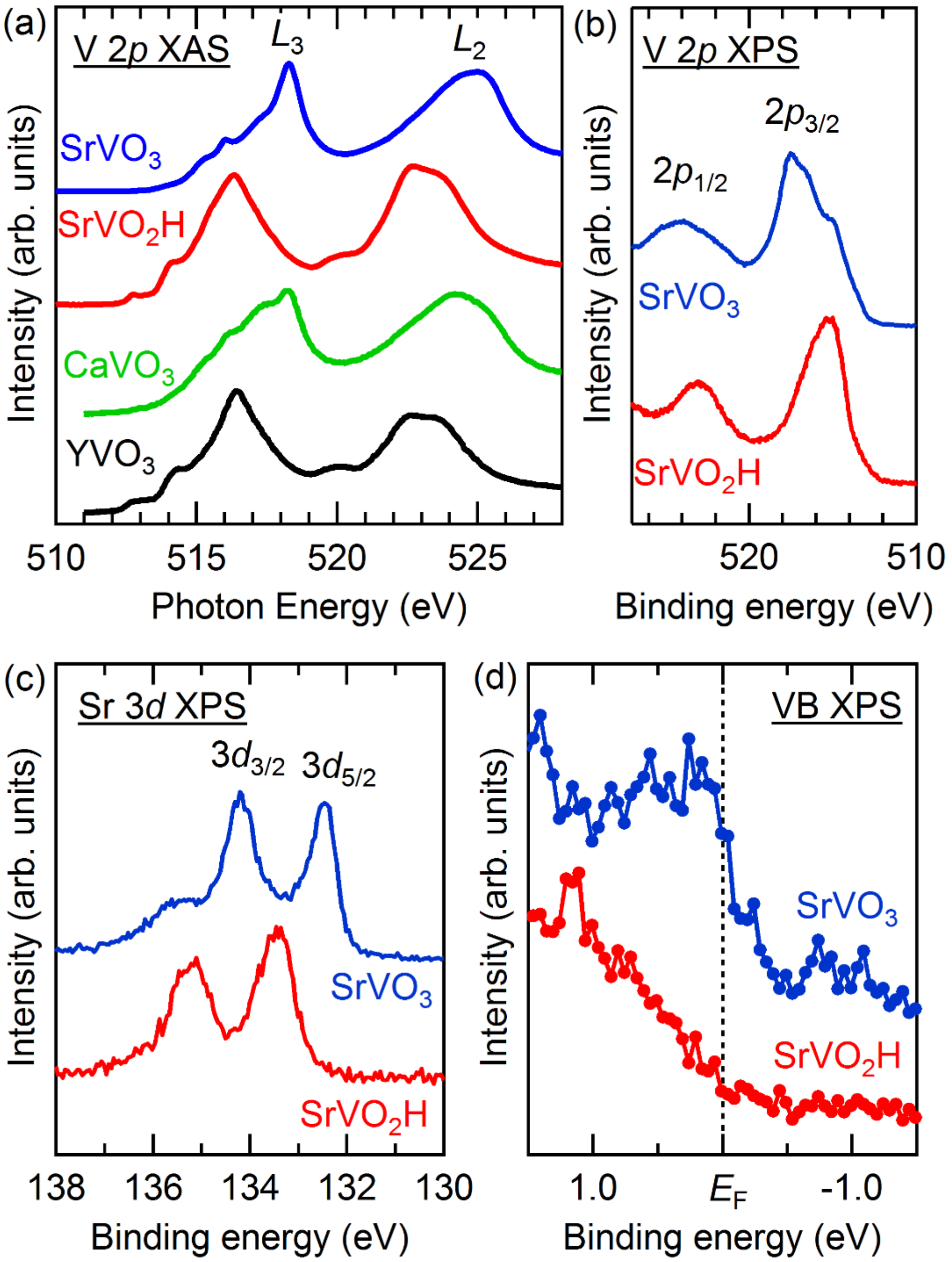

Figure 3-9. (a) V L-edge XAS spectra of the precursor $SrVO_3$ and $SrVO_2H$ films, and the relevant spectra of $CaVO_3$ (V^{4+}) and YVO_3 (V^{3+}) [102]. XPS spectra of (b) V 2p, (c) Sr 3d, and (d) valence band (VB) near E_F for the $SrVO_3$ and $SrVO_2H$ films with a photon-energy of 7940 eV.

of VO (V^{2+}, 512.7 eV) and VO_2 (V^{4+}, 516.0 eV) [103], indicating that the V^{3+} oxidation state survives even at the surface of the $SrVO_2H$ film. On the other hand, the precursor film displayed a mixed valence feature of V^{4+} and V^{5+}, suggesting that the surface of the precursor was oxidized.

It is known that the position of Sr 3*d* peak is sensitive to the surrounding anions [104]. Figure 3-9(c) shows Sr 3*d* XPS spectra for the films. The Sr $3d_{5/2}$ peak of the $SrVO_2H$ film was located at 133.4 eV, which is ~1 eV higher than those of the $SrVO_3$ film (132.4 eV) and oxide SrO (132.6 eV), but is ~0.9 eV lower than that of hydride SrH_2 (134.3 eV) [104]. This indicates that strontium ion forms bonds to oxide and hydride anions in the $SrVO_2H$ film.

For the $SrVO_2H$ film, the density of state (DOS) at the Fermi energy was negligibly low, in contrast to the metallic $SrVO_3$ precursor (Fig. 3-9(d)). This is consistent with the theoretical prediction that $SrVO_2H$ is a Mott insulator [20]. The $SrVO_2H$ film with V^{3+} ($3d^2$) has a tetragonal structure with a large a/c ratio, resulting in opening of an energy gap between the occupied $(d_{xz}, d_{yz})^2$ and unoccupied $d_{xy}{}^0$ bands. This probably induces a Mott transition from the metallic $SrVO_3$ to insulating $SrVO_2H$ [20].

3.4 Conclusion

I successfully fabricated perovskite $SrCoO_xH_y$ thin films via the topotactic hydride doping of brownmillerite $SrCoO_{2.5}$ epitaxial thin films with CaH_2. The perovskite-type cation framework was maintained during the topotactic treatment owing to epitaxial stabilization. Structural and chemical analyses accompanied by the XAS measurements revealed that the doped hydride ions form a 2D network of Co-H^--Co bonds, in contrast to other reported perovskite oxyhydrides, $SrMO_{3-x}H_x$ (M = Cr, Ti, V). The $SrCoO_xH_y$ thin film exhibited insulating behavior and had a direct band gap of 2.1 eV. I also succeeded in topotactic hydridation synthesis of single crystalline $SrVO_2H$ films with 1D V-H^--V bonds along the out-of-plane direction. The temperature of the topotactic synthesis could be lowered by reducing the film thickness. XPS and XAS measurements of the $SrVO_2H$ film revealed V^{3+} oxidation state, proving that hydrogen exists as hydride. Furthermore, I observed binding energy shift of Sr and metal-insulator transition, originating from the H^- substitution. Thus, topotactic hydride doping of transition-metal-oxide thin films on suitable substrates is a promising way for the synthesis of new transition metal oxyhydrides.

Chapter 4 Topotactic fluorination: perovskite $SrFeO_{3-x}F_x$ and $SrCoO_xF_y$ films

4.1 Introduction

Since the discovery of superconductivity (transition temperature of $T_c = 46$ K) in non-ordinary oxyfluorides $Sr_2CuO_2F_{2+x}$ [21], the replacement of O^{2-} by F^- in transition-metal oxides has attracted a great deal of attention as a chemical technique that can considerably modify the electronic properties of their mother compounds. Among these compounds, novel oxyfluoride $SrFeO_2F$ has gained considerable interest owing to the simple crystal structure and strong antiferromagnetic interaction [31,32,40]. The oxyfluoride compound is reported to be synthesized from $SrFeO_{3-\delta}$ via topotactic fluorination using polyvinylidene fluoride (PVDF) at 400 °C in form of bulk [32].

It is expected that the reactivity of thin-film samples with PVDF should be much higher than that of bulk samples because thin films have larger surface areas and smaller volumes than bulk samples. More recently, the fluorination technique using PVDF was applied to $SrFeO_{3-\delta}$ thin films, where a PVDF solution was spin-coated on the film and the film/polymer bilayer was annealed at 600 °C, though the $SrFeO_{3-\alpha}F_\gamma$ films thus obtained had relatively low fluorine contents ($\gamma < 1$) despite of higher synthesis temperature than that for bulk $SrFeO_2F$ [105].

In this chapter, I present topotactic fluorination synthesis of $SrFeO_{3-x}F_x$ epitaxial thin films using PVDF. The fluorine content (x) of the films was controllable over a wide range ($0.8 \leq x \leq {\sim}1.5$) by means of the heat-treatment temperature. The fluorination reaction was conducted at 150–270 °C, which was much lower than the reaction temperature reported for bulk, 400 °C. Furthermore, it is found that the value of x is dependent on the amount of oxygen vacancies present in the precursor film. The electronic structure of the $SrFeO_{3-x}F_x$ films was also investigated by optical absorption, photoemission, and X-ray absorption spectroscopy, as well as density functional theory (DFT)-based calculations. In addition, I also present topotactic reductive fluorination synthesis of $SrCoO_xF_y$ epitaxial thin films with $Co^{2+/3+}$ oxidation states from precursor $SrCoO_{2.5}$ films by using PVDF.

4.2 Method

4.2.1 Method for $SrFeO_{3-x}F_x$ films

Synthesis

Three types of precursor $SrFeO_x$ films with different oxygen contents ($x \approx 2$, 2.5, and 3) were prepared. Precursor $SrFeO_{2.5}$ films were grown on STO(001) substrates by a PLD technique, with a $SrFeO_{3-\delta}$ ceramic pellet (20 mm in diameter and 5 mm in thickness, TOSHIMA Manufacturing Co.) used as a PLD target. The fourth harmonic of a Nd-YAG laser (wavelength $\lambda = 266$ nm) with an energy of 0.3 J/cm^2/shot and a repetition rate of 10/3 Hz was employed for ablation. The substrate temperature and oxygen partial pressure were kept at 700 °C and 5×10^{-5} Torr, respectively, during each deposition run, and coherent growth of the precursor $SrFeO_{2.5}$ films on STO(001) substrates was confirmed. Oxidized $SrFeO_x$ ($x \approx 3$) films with perovskite structure were fabricated by annealing $SrFeO_{2.5}$ films at 700 °C in air for 2 h. Additional reduced $SrFeO_x$ ($x \approx 2$) films with infinite-layer structures were obtained by heating $SrFeO_{2.5}$ films with CaH_2 (Wako Pure Chemical Industries, Ltd.) at 280 °C for 24 h in evacuated Pyrex tubes.

The obtained precursor $SrFeO_x$ ($x \approx 2$, 2.5, and 3) films were further subjected to fluorination with 0.1 g of PVDF (Fluorochem Ltd.) at temperatures (T_f) ranging from 100 to 450 °C for 24 h under an Ar gas flow of 70 cc/min (with the films covered by Al foil so as not to contact with PVDF directly). Typical film thickness, as measured by a stylus surface profiler, was ~80 nm.

Structural and chemical composition

Crystal structures of the films were determined by XRD and TEM measurements. The chemical composition of the films was analysed by EDS equipped with SEM in which the electron accelerating voltage was set at 2.5 keV to reduce the background signal from the substrate. The amount of fluorine was evaluated by NRA using the $^{19}F(p,\alpha\gamma)^{16}O$ resonant nuclear reaction at 902 keV. In NRA measurements, a CaF_2 single crystal was used as a reference for fluorine. The EDS and NRA results included experimental errors of ~20%. The depth profiles of the chemical compositions were evaluated by XPS with Ar^+-ion sputtering. The core levels of iron were also observed by XPS. The surface morphology was characterized by AFM.

Electronic structure

Optical bandgaps were measured using a UV–VIS spectrometer. I adapted Murmann's method, which considers the interference of multiple reflected beams, in order to estimate the extinction coefficient k according to the transmittance and reflectance spectra of the films and STO substrate [92]. The obtained k was converted into the absorption coefficient α by using the relation $\alpha = 4\pi k/\lambda$, where λ is the wavelength of light. XPS and XAS measurements were conducted at the BL-2A beamline of Photon Factory, KEK. To reduce the charge-up effect, the $SrFeO_{3-x}F_x$ films were fabricated on conductive Nb:STO substrates. The XPS spectra were measured using a VG-SCIENTA SES-2002 electron-energy analyzer at a photon energy of 1,000 eV. The energy offset was calibrated using the carbon signal. The XAS spectra were measured by the total electron-yield method.

DFT calculations were performed for bulk $SrFeO_2F$ and $LaFeO_3$ using the Vienna *ab initio* simulation package [106]. The Perdew–Burke–Ernzerhof functional of the generalized gradient approximation (GGA) was adapted with a Hubbard $+U$ term of $+U$ (Fe 3d) = 4.0 eV. This $+U$ value was adopted from theoretical reports on similar iron oxides, such as $SrFeO_2$, $BiFeO_3$, and Fe_2O_3 [107-109]. To represent the octahedral rotations, I constructed a $\sqrt{2} \times \sqrt{2} \times 2$ supercell of a simple perovskite unit cell. The supercell contained 20 atoms, with FeO_4F_2 (FeO_6) octahedra for $SrFeO_2F$ ($LaFeO_3$). For the magnetic structures of $SrFeO_2F$ and $LaFeO_3$, *G*-type antiferromagnetic spin arrangement is assumed, according to previous neutron-diffraction studies [41,110]. The effects of the core electrons were treated with the projector augmented-wave method, as described in Ref. 111. The cutoff energy of the plane-wave basis was set as 560 eV. Brillouin-zone integration was performed using the Monkhorst–Pack scheme with a **k**-point mesh of 8 × 8 × 6. The atomic positions were optimized according to the Hellman–Feynman forces acting on the atoms. The band structure was calculated using the same GGA +*U* functional, pseudopotential, and cut-off energy that were used for the supercell.

4.2.2 Method for $SrCoO_xF_y$ films

Brownmillerite $SrCoO_{2.5}$ precursor films were grown on STO(001) substrates in the same way as the precursor of the $SrCoO_xH_y$ films (see Chapter 3.2.1). The obtained $SrCoO_{2.5}$ precursor films were further subjected to fluorination using PVDF at T_f ranging from 150 to 250 °C for 12 h under a flow of Ar gas. The films were covered with Al foil to prevent direct contact with the PVDF. A typical film thickness was 50–60 nm.

Crystal structures of the films were characterized using an X-ray diffractometer with Cu-$K\alpha$ radiation. The chemical composition of the films was determined by EDS in which the electron accelerating voltage was set at 2.5 keV to reduce any substrate contribution. The F content was determined by NRA using the $^{19}F(p,\alpha\gamma)^{16}O$ resonant nuclear reaction at 902 keV, in which a CaF_2 single crystal plate was used as a standard reference for F concentration. The EDS and NRA results included experimental errors of ~20 %. The core levels of Co were observed by XPS. In-plane magnetization measurements were performed using a SQUID magnetometer.

4.3 Results and discussion

4.3.1 Synthesis of $SrFeO_{3-x}F_x$ films

Crystal structure analysis

Figure 4-1(a) shows the 2*θ*–*θ* XRD patterns of films obtained by fluorination of $SrFeO_{2.5}$ precursor film at T_f = 100–450 °C for 24 h. The XRD pattern of the $SrFeO_{2.5}$ precursor film has also been included in the figure for comparison. The film treated with PVDF at 100 °C showed a diffraction peak at $2\theta \approx 45.8°$, corresponding to the 002 reflection of the $SrFeO_{2.5}$ structure, which means that PVDF did not react with the $SrFeO_{2.5}$ film below 100 °C. The films fluorinated at 150–270 °C exhibited only the 002 diffraction peaks of the perovskite structure, indicating that $SrFeO_{3-x}F_x$ can be obtained at 150–270 °C. Additionally, the position of the 002 peak was shifted to lower-angle side (from 45.5° to 45.1°) on increasing T_f from 150 to 270 °C. At 300 °C, the diffraction peak of perovskite $SrFeO_{3-x}F_x$ disappeared, and a peak assignable to SrF_2 002 appeared. Above 350 °C, the peaks corresponding to SrF_2 002 and Fe_3O_4 002 evolved, reflecting the complete decomposition of perovskite $SrFeO_{3-x}F_x$ into SrF_2 and Fe_3O_4.

Figure 4-1(b) shows an XRD reciprocal space map for asymmetric 103 diffraction of the $SrFeO_{3-x}F_x$ film fluorinated at 250 °C. Notably, the q_x value of the $SrFeO_{3-x}F_x$ 103 peak coincides with that of STO 103. This implies that the *a*-axis of the $SrFeO_{3-x}F_x$ film was completely locked to the STO lattice, even after treatment with PVDF. In other words, the perovskite-like cation network was maintained during the topotactic fluorination reaction promoted by PVDF.

Figure 4-1(c) shows the plots the lattice parameters for the $SrFeO_{3-x}F_x$ films as a function of T_f. The *c*-axis length increased from 3.989 to 4.022 Å upon increasing T_f from 150 to 270 °C in a nonlinear manner, whereas the *a*-axis length was essentially independent of T_f. In the case of bulk $SrFeO_2F$, it was reported that the cell volume was greatly increased upon fluorination of precursor $SrFeO_{3-\delta}$ because of the simultaneous occurrence of fluorine insertion and substitution [32,112]. Therefore, in this case, the

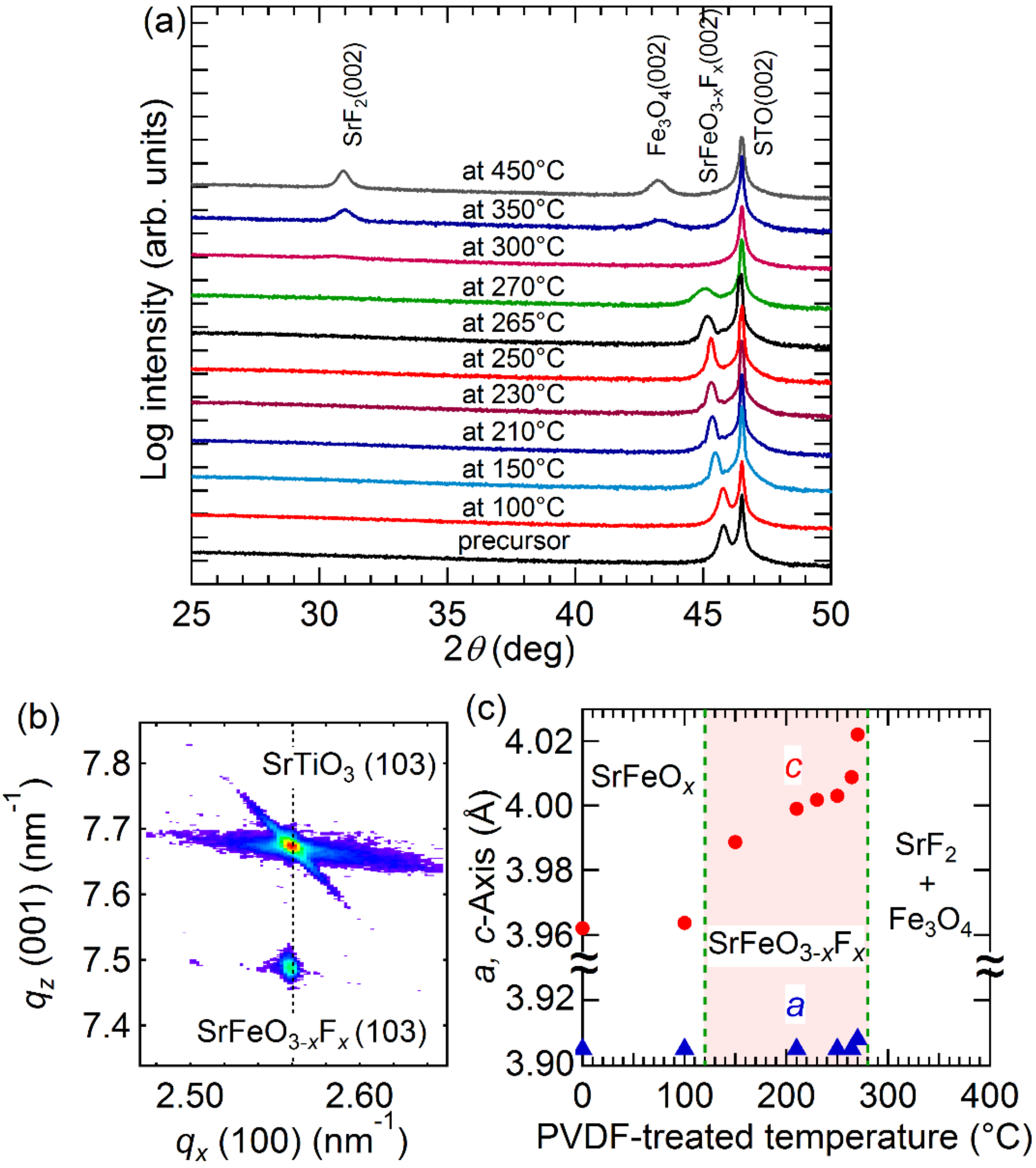

Figure 4-1. (a) 2*θ*–*θ* X-ray diffraction patterns of $SrFeO_{2.5}$ precursor film and films fluorinated at 100–450 °C with PVDF for 24 h. (b) Logarithmic contour mapping in reciprocal space for asymmetric (103) peaks of $SrFeO_{3-x}F_x$ film on $SrTiO_3$ substrate fluorinated at 250 °C. (c) Lengths of *a*- and *c*-axes of $SrFeO_{3-x}F_x$ films as a function of fluorination temperature.

increase in the *c*-axis length suggests that fluorine insertion and substitution reactions take place.

Figure 4-2(a) shows a wide-view cross-sectional TEM image of the $SrFeO_{3-x}F_x$ film fluorinated at 270 °C. Neither segregated impurities nor amorphous phases were recognized from the TEM observations. Figure 4-2(b) is a magnified view of the same image. The image clearly indicates a tetragonal perovskite structure with lattice constants of a ~ 3.9 Å and c ~ 4.0 Å, which is consistent with those obtained from XRD (a = 3.908 Å, c = 4.022 Å).

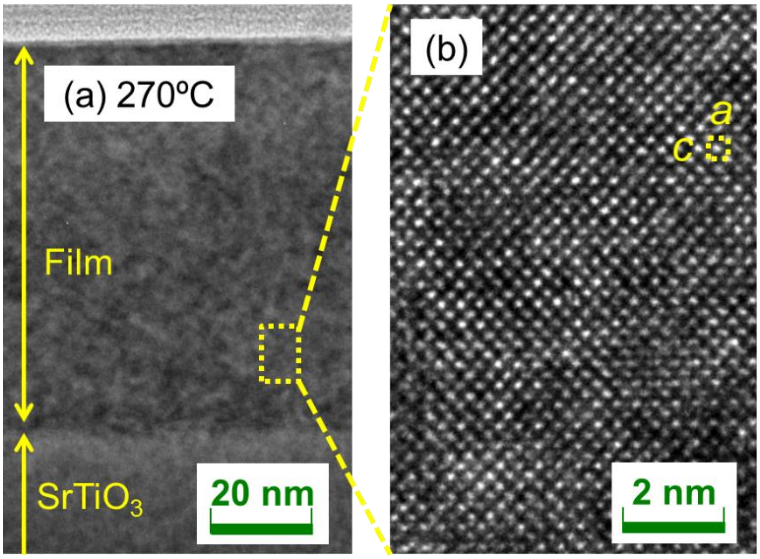

Figure 4-2. Cross-sectional transition electron microscopy images of $SrFeO_{3-x}F_x$ film fluorinated at 270 °C with (a) wide-range view and (b) magnified view.

Compositional analysis

To verify fluorine doping and investigate the relationship between the doped fluorine content and T_f, EDS measurements were performed for O $K\alpha$, F $K\alpha$, and Fe $L\alpha$. Figure 4-3(a) depicts the EDS spectra near the O $K\alpha$ and F $K\alpha$ peaks of the $SrFeO_{2.5}$ precursor and $SrFeO_{3-x}F_x$ films fluorinated at 150, 250, and 270 °C, where the spectral intensity was normalized by the area of Fe $L\alpha$ peak. As seen in the figure, the peak area of F $K\alpha$ increased with increase in T_f, while that of O $K\alpha$ showed a tendency to decrease.

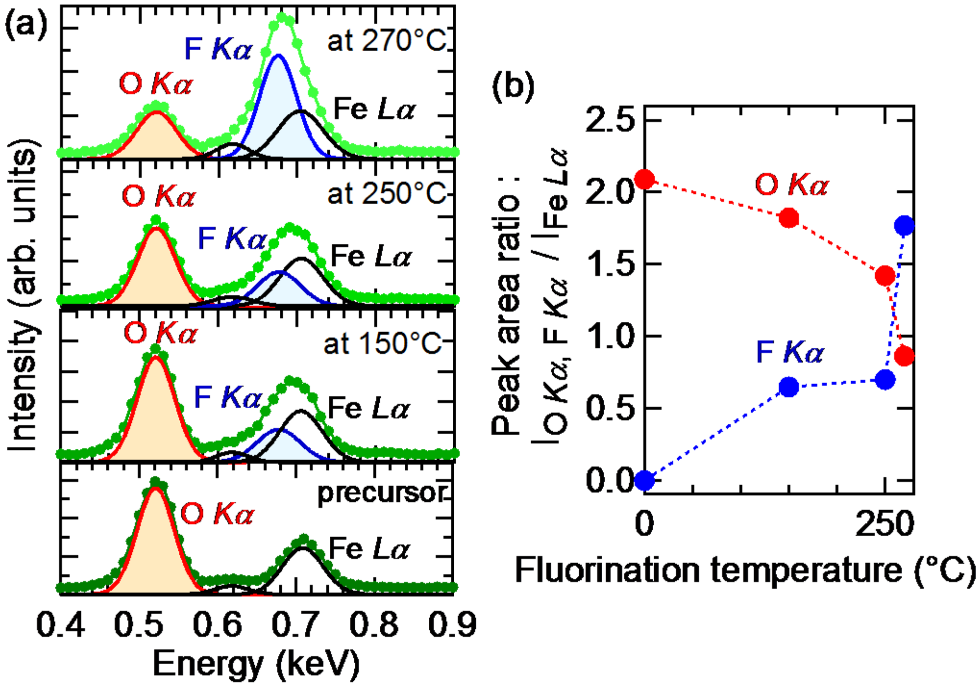

Figure 4-3. Energy dispersive X-ray spectra (EDS) near (a) O *Kα*, F *Kα*, and Fe *Lα* peaks of $SrFeO_{2.5}$ precursor film and $SrFeO_{3-x}F_x$ films fluorinated at 150, 250, and 270 °C. (b) EDS peak area of F *Kα* and O *Kα* as a function of fluorination temperature.

Figure 4-3(b) shows the plots of the areas of the F *Kα* and O *Kα* peaks, S_F and S_O, respectively, against T_f. The S_F/S_O ratio of the film fluorinated at 250 °C is 1:2, whereas that of the film fluorinated at 270 °C is enhanced to 2:1. This implies that the fluorine content of the $SrFeO_{3-x}F_x$ films can be controlled by T_f.

NRA measurements were conducted so as to quantitatively determine the fluorine content of the films. Figure 4-4(a) shows the NRA spectrum of the $SrFeO_{3-x}F_x$ film fluorinated at 250 °C. The γ-ray emitted by the nuclear reaction of $^{19}F(p,\alpha\gamma)^{16}O$ was clearly observed in the $SrFeO_{3-x}F_x$ film, and the x value was determined to be 0.92 ± 0.18. Figure 4-4(b) shows the correlation between the c-axis length and x values in $SrFeO_{3-x}F_x$, where the x values were evaluated from EDS and NRA measurements independently, referred to as x(EDS) and x(NRA), respectively. For the evaluation of x(EDS), the relation $x = 3 \times S_F / (S_F + a \times S_O)$ was used in an assumption of O : F = $3 - x : x$, where the relative

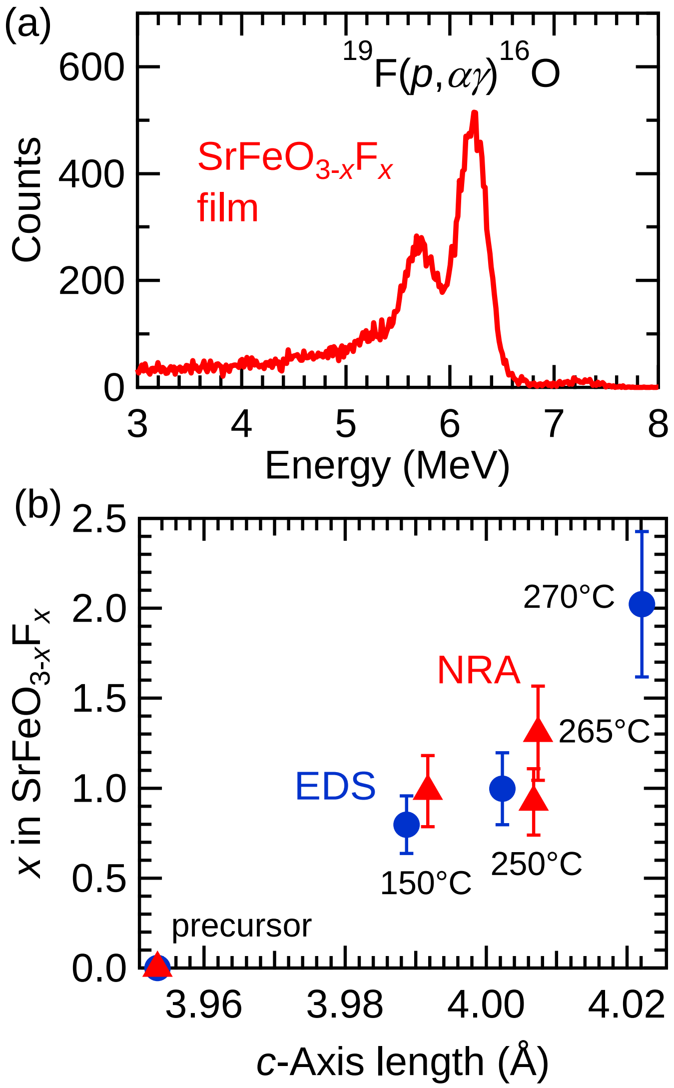

Figure 4-4. (a) Nuclear reaction analysis (NRA) spectra of $SrFeO_{3-x}F_x$ film fluorinated at 250 °C. (b) c-Axis length dependence of x in $SrFeO_{3-x}F_x$ film, estimated from energy dispersive X-ray spectra (EDS) and NRA measurements. Different samples were used for NRA and EDS measurements.

sensitivity factor (a) was estimated as 0.989 based on a Monte Carlo simulation of electron trajectory in solids [92]. As seen in Figure 4-4(b), both x(EDS) and x(NRA) are in good agreement with each other, which indicates that the assumption mentioned above (O:F = $(3 - x) : x$) is reasonable, although I cannot deny the possibility that a certain amount of oxygen vacancies remain in the film (in other words, the doped fluorine atoms were substituted for the oxygen sites of the perovskite lattice). Notably, the c-axis length of the $SrFeO_{3-x}F_x$ film increased as the value of x increased, despite the fact that F^- has a smaller ionic radius than O^{2-}. This can be rationalized by taking the chemical reduction of the Fe ions into consideration. The shrinkage of cell volume associated with F^- substitution is overwhelmed by cell expansion upon the reduction of Fe ions [32,112]. The x value of the $SrFeO_{3-x}F_x$ film fluorinated at 270 °C was ~2, which is twice that of bulk $SrFeO_2F$, though I cannot deny the possibility that the fluorine contents were overestimated because carbon impurities on the surface may adsorb fluorine ions during the PVDF treatment.

Because fluorination proceeds at the film surface, the population of fluorine ions is potentially higher closer to the surface. Figure 4-5 shows the fluorine depth profile of the $SrFeO_{3-x}F_x$ ($x \approx 1$) film obtained at 250 °C, measured by XPS with Ar^+-ion sputtering, where the peak area of F 1s relative to that of O 1s, A_F/A_O, at the surface (0 nm) was set to 1. Near the surface (0–15 nm), the A_F/A_O decreased with increasing depth, reaching ~0.8 at 15 nm. The A_F/A_O value was virtually constant at 15–80 nm, and slightly increased

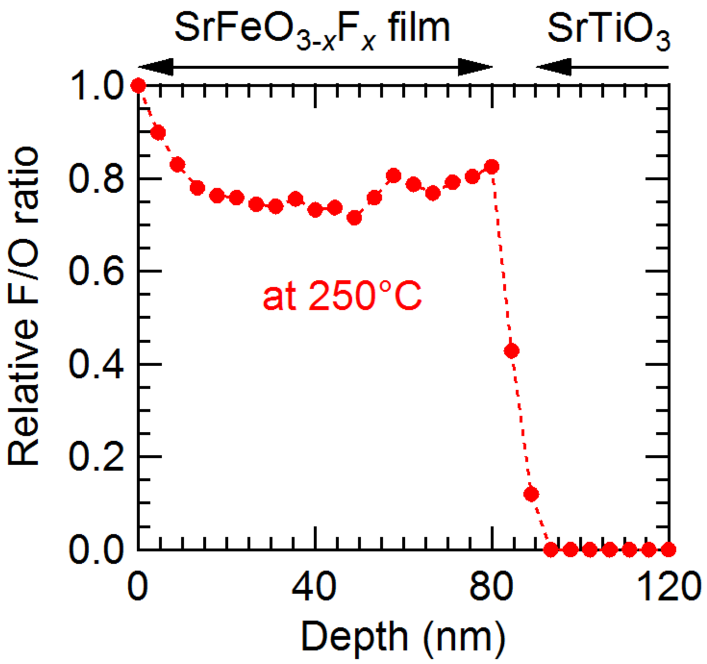

Figure 4-5. Fluorine depth profile of $SrFeO_{3-x}F_x$ ($x \approx 1$) film fluorinated at 250 °C, obtained from $SrFeO_{2.5}$ precursor film, measured by X-ray photoemission spectroscopy with Ar^+-ion sputtering.

near the interface of the film and the substrate. These results suggest that fluorine ions diffused not only in the vicinity of surface, but also over the entire film. On the other hand, in the STO substrate region (>90 nm), fluorine was not detected, indicating that the diffusion of fluorine into the STO substrate is negligible.

Oxidation state of iron and surface morphology

Figure 4-6 depicts the Fe 2p core-level XPS spectra of the $SrFeO_{3-x}F_x$ films fluorinated at 150, 250, and 270 °C. Each spectrum showed Fe 2$p_{3/2}$ and 2$p_{1/2}$ peaks, and a satellite peak located between the Fe 2$p_{1/2}$–Fe 2$p_{3/2}$ doublet. Notably, the locations of the satellite peaks, which are known to be very sensitive to the oxidation state of Fe, differ from one sample to another. The satellite peaks in the $SrFeO_{3-x}F_x$ films fluorinated at 150 and 250 °C were located at an E_b of ~719 and ~718 eV, respectively, which are equivalent to the peak in $LaFeO_3$ with Fe^{3+} (E_b = 718.7 eV) [113]. That is, the valences of the Fe ions in the films are almost trivalent. Meanwhile, the satellite peak of the film fluorinated at 270 °C was located at an E_b of 712–719 eV, between the doublet peaks, suggesting that the Fe ion has a mixed valence state of Fe^{2+}/Fe^{3+} [114]. The Fe^{2+}/Fe^{3+} ratio was further evaluated by comparing the XPS data of the $SrFeO_{3-x}F_x$ film fluorinated at 270 °C and $SrFeO_{2.5}$ film reported in Ref. 115. The area-intensity of Fe^{3+} satellite peak relative to Fe 2$p_{3/2}$ main peak for the fluorinated film was approximately half of that for the $SrFe^{3+}O_{2.5}$ film, implying that ~50% of Fe exists as Fe^{3+} in the $SrFeO_{3-x}F_x$ film. Thus, I can roughly deduce the fluorine content (x) as $x \approx 1.5$.

Figure 4-7 shows the AFM images of the $SrFeO_{2.5}$ precursor film and the $SrFeO_{3-x}F_x$ films fluorinated at 250 and 270 °C. The root mean square values of surface roughness were found to be 0.35, 0.64, and 0.81 nm, respectively. Thus, the film surface became rougher with increasing fluorination temperature, however, the fluorination process does not cause severe surface roughing.

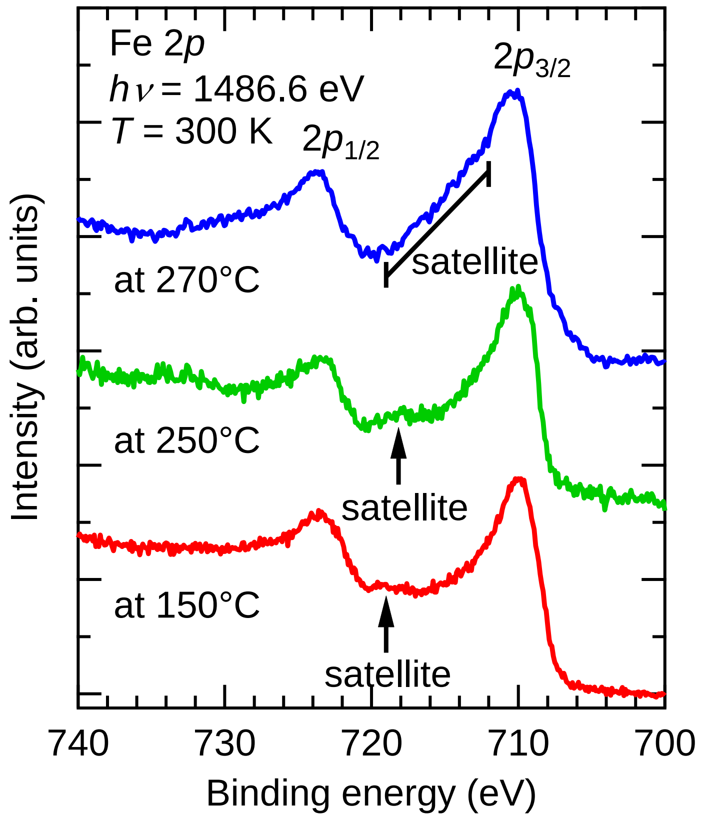

Figure 4-6. Fe 2*p* core-level X-ray photoemission spectra of $SrFeO_{3-x}F_x$ films fluorinated at 150, 250, and 270 °C, obtained from $SrFeO_{2.5}$ precursor films.

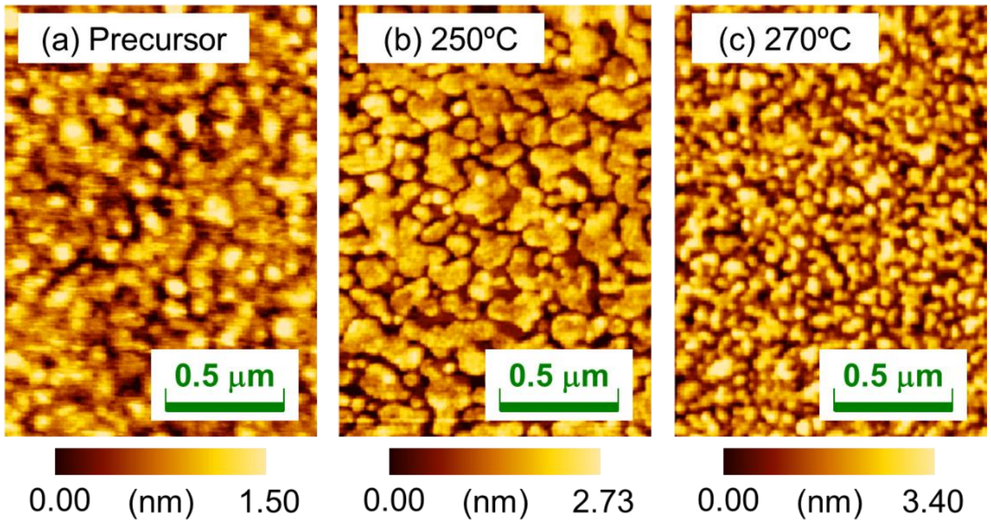

Figure 4-7. Atomic force microscope images of (a) $SrFeO_{2.5}$ precursor film and $SrFeO_{3-x}F_x$ films fluorinated at (b) 250 and (c) 270 °C.

Dependence on oxygen vacancies of precursor film

The relationship between the fluorine content (x) and oxygen vacancies in the precursor films is another important consideration. Figures 4-8(a) and 4-8(b) compare the XRD patterns of the oxidized $SrFeO_x$ ($x \approx 3$) and reduced $SrFeO_x$ ($x \approx 2$) precursor films fluorinated at 150 °C for 24 h. The oxidized and reduced precursor films show the 002 diffraction peaks of perovskite-type and infinite-layer structures with $c = 3.835$ and 3.490 Å, respectively. The c-axis length of the oxidized $SrFeO_x$ ($x \approx 3$) film is close to that of

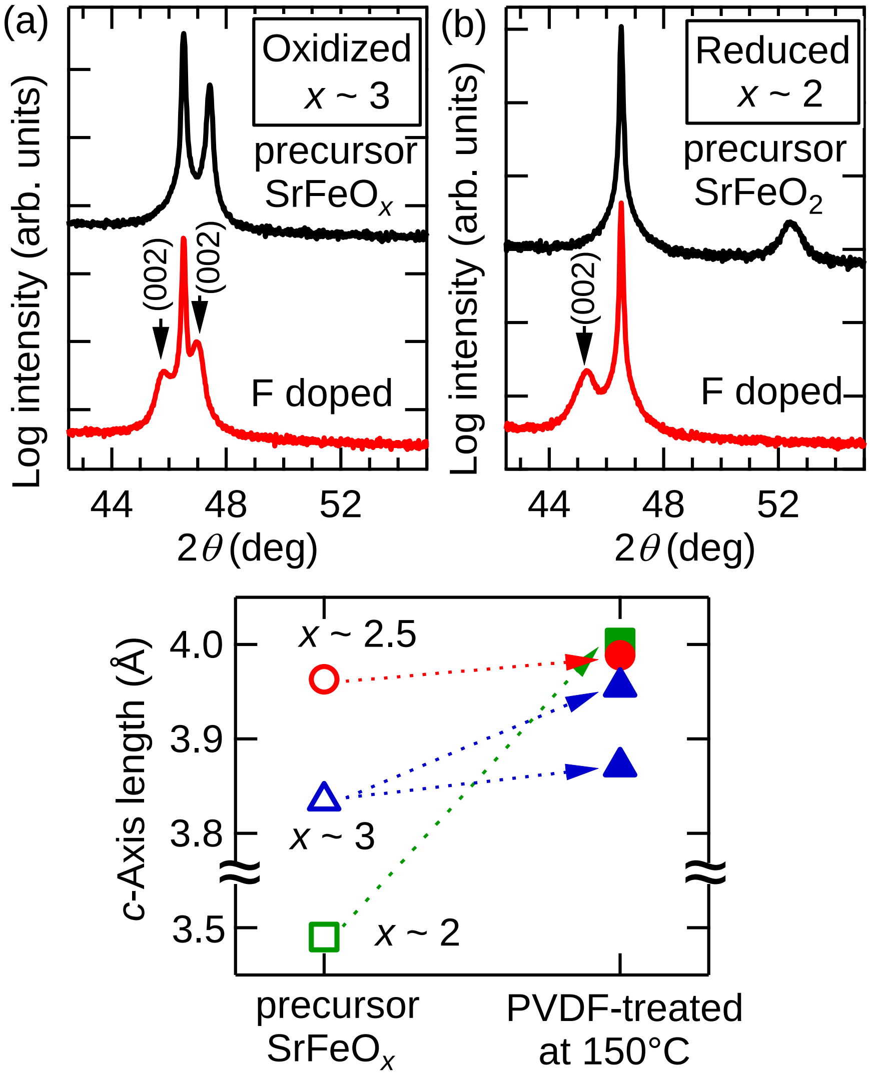

Figure 4-8. X-ray diffraction patterns of (a) oxidized $SrFeO_x$ ($x \approx 3$) and (b) reduced $SrFeO_x$ ($x \approx 2$) precursor films, and films fluorinated at 150 °C with PVDF for 24 h. (c) c-Axis lengths of $SrFeO_x$ ($x \approx 2$, 2.5, and 3) precursor and fluorinated films.

the strained $SrFeO_3$ film on the STO substrate, 3.823 Å [116]. After treatment with PVDF, the film prepared from the $SrFeO_x$ ($x \approx 3$) precursor showed two 002 diffraction peaks corresponding to c = 3.871 and 3.955 Å, whereas the film prepared from $SrFeO_x$ ($x \approx 2$) exhibited one peak with c = 4.002 Å. Figure 4-8(c) shows a plot of the c-axis lengths of the $SrFeO_x$ ($x \approx 2$, 2.5, and 3) precursor and fluorinated films. As seen in Fig. 4-8(c), the c-axis length of the film fluorinated at 150 °C becomes longer as the oxygen content in the precursor $SrFeO_x$ film is decreased from $x \approx 3$ to 2. Because the c-axis lengths of the fluorinated films reflect the fluorine content, this result suggests that precursor films containing more oxygen vacancies tend to incorporate more fluorine ions into the film.

To investigate the origin of the two 002 peaks, the fluorine and oxygen depth profiles of the $SrFeO_{3-x}F_x$ film obtained from the oxidized $SrFeO_x$ ($x \approx 3$) precursor were measured in detail (Fig. 4-9). As seen from the figure, the A_F/A_O vs. depth plot shows two plateaus: ~0.8 at 5–40 nm and ~0.4 at 40–80 nm. These fluorine-rich and fluorine-poor regions correspond to the two 002 diffraction peaks at $2\theta \approx 45.9°$ and 47.0°, respectively

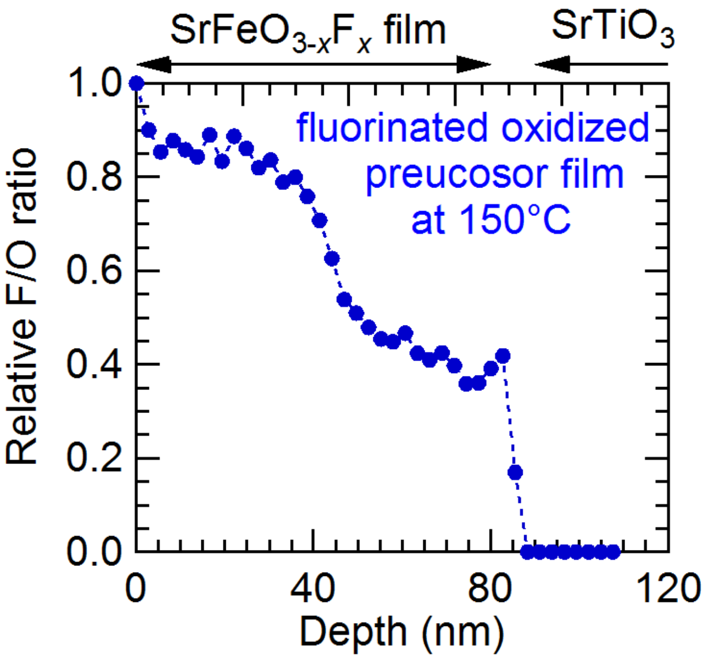

Figure 4-9. Fluorine depth profile of $SrFeO_{3-x}F_x$ film fluorinated at 150 °C obtained from oxidized $SrFeO_x$ ($x \approx 3$) precursor film by X-ray photoemission spectroscopy with Ar^+-ion sputtering.

(Fig. 4-8(a)). These results imply that the diffusion of fluorine ions is considerably slowed as the concentration of oxygen vacancies decreases.

Comparison with diffusion mechanism

As stated above, the $SrFeO_{3-x}F_x$ films were obtained at much lower temperatures (150–270 °C) than the bulk sample (400 °C) [32]. Now, I will discuss the difference in the reactivity between thin film and bulk based on the diffusion equation [117]. The fluorine ions were not diffused into the STO substrates (Fig. 4-5). In such a case, the relative fluorine concentration, *C*(*x*), is given by following equation:

$$C(x) = 1 - \sum_{\mathrm{n}=1}^{\infty} \frac{2L \cdot \cos\left(\beta_{\mathrm{n}} \cdot \frac{l-x}{l}\right) \cdot \exp\left(\frac{-\beta_{\mathrm{n}}^2 \cdot D \cdot t}{l^2}\right)}{(-\beta_{\mathrm{n}}^2 + L^2 + L) \cdot \cos\beta_{\mathrm{n}}} \qquad (x \le l)$$

where *x* is the distance from the surface, *t* is the time, *D* is the diffusion coefficient, *k* is the surface exchange coefficient, *l* is the thickness of the film, and $L = l \cdot k/D$ [117]. The

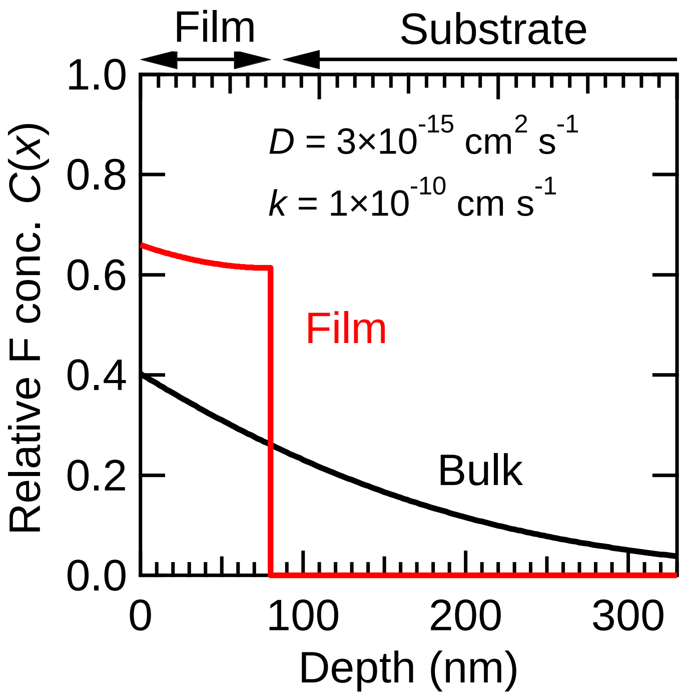

Figure 4-10. Relative fluorine concentration (*C*(*x*)) vs. depth (*x*) curves at $t = 24$ h, calculated for thin film with $l = 80$ nm and for bulk sample with $l \to \infty$. *D* and *k* were assumed to be 3×10^{-15} cm^2 s^{-1} and 1×10^{-10} cm s^{-1}, respectively.

β_n values are the positive roots of the equation: $\beta_n \cdot \tan \beta_n = L$. Approximately, the value of D describes the overall shape of the $C(x)$ curve, while k determines the $C(x)$ value at $x = 0$. Figure 4-10 shows the depth dependence of $C(x)$ for a thin film with $l = 80$ nm, and for a bulk sample with $l \rightarrow \infty$ at $t = 24$ h, where D was set to 3×10^{-15} cm^2 s^{-1}, so as to reproduce the fluorine depth profile measured by XPS (Fig. 4- 5). In the case of the bulk sample, $C(x)$ decreases with x in an exponential manner, with the diffusion length of 3×10^2 nm. That is, only fluorine diffuses into the surface regions, which means that the higher fluorine contents experimentally observed in thin films are attributable to smaller grain sizes, representing the maximum length of the diffusion path.

4.3.2 Properties of $SrFeO_{3-x}F_x$ films

Optical properties

Figure 4-11(a) shows optical-absorption spectra of the $SrFeO_{3-x}F_x$ ($x \approx 0.6$, 0.8, and 1) films on STO substrates. The $SrFeO_{3-x}F_x$ ($x \approx 1$) film exhibited an absorption peak at 2.7 eV (labeled *A* in Fig. 4-11(a)). As the fluorine content decreased from 1 to 0.6, α increased in the visible-light region of 1.8–3.0 eV, and a new absorption peak appeared around 1 eV (labeled *B*). This peak was speculated to originate from the hole-induced state within the energy gap of $SrFe^{3+}O_2F$ (Fig. 4-11(b)), as reported for Sr-doped $LaFe^{3+}O_3$ [113,118,119].

The optical coefficient is known to follow the relation $(\alpha h\nu)^n = A(h\nu - E_g)$ near the band edge, where E_g is the bandgap energy, $h\nu$ is the photon energy, and n is a constant. In the inset of Fig. 1(a), $(\alpha h\nu)^2$ is plotted as a function of $h\nu$ for the $SrFeO_{3-x}F_x$ ($x \approx 1$) and $LaFeO_3$ films. The linear $(\alpha h\nu)^2$ vs. $h\nu$ relations suggest that both of the compounds have direct bandgaps. By extrapolating the linear part of the $(\alpha h\nu)^2 - h\nu$ curve to $(\alpha h\nu)^2 = 0$, the optical bandgaps of the $SrFeO_{3-x}F_x$ ($x \approx 1$) and $LaFeO_3$ films were evaluated as 2.4 and 2.1 eV, respectively. These values are larger than that of the $SrFeO_{2.5}$ precursor film (1.7 eV) [115].

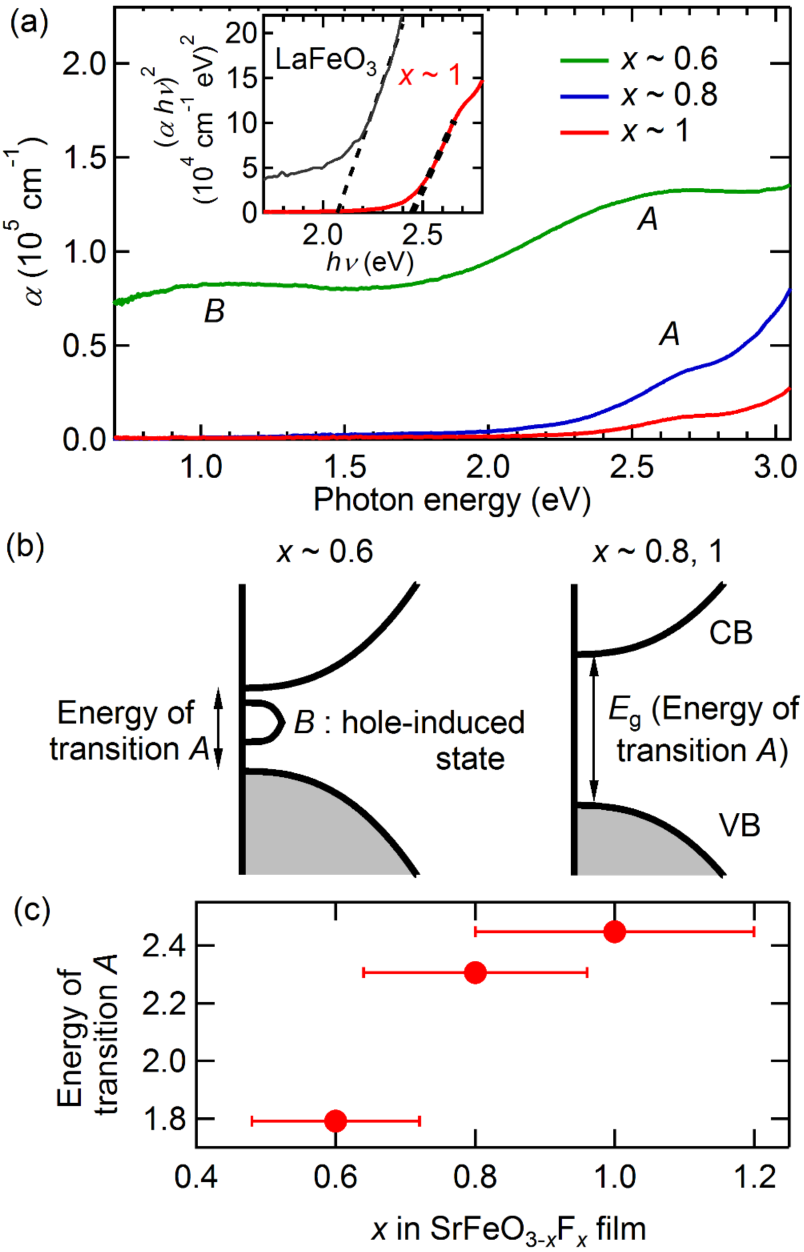

Figure 4-11. (a) Optical-absorption spectra of the $SrFeO_{3-x}F_x$ ($x \approx 0.6$, 0.8, and 1) films on the $SrTiO_3$ substrates. The inset shows $(\alpha h\nu)^2$ vs. $h\nu$ curves for the $SrFeO_{3-x}F_x$ ($x \approx 1$) and $LaFeO_3$ films. (b) Schematic showing the DOS for the $SrFeO_{3-x}F_x$ films with $x \sim 0.6$ as well as $x \sim 0.8$ and 1. (c) Energy of transition A estimated from the $(\alpha h\nu)^2$ - $h\nu$ curves for the $SrFeO_{3-x}F_x$ ($x \approx 0.6$, 0.8, and 1) films.

Figure 4-11(c) shows the energy of transition *A* estimated according to the $(\alpha h\nu)^2$ - $h\nu$ curves for the $SrFeO_{3-x}F_x$ ($x \approx 0.6$, 0.8, and 1) films. For the $SrFeO_{3-x}F_x$ ($x \approx 0.8$ and 1) films, the energy of transition *A* can be regarded as the optical bandgap (Fig. 4-11(b)). As shown in Fig. 4-11(c), the energy of transition *A* increased as the fluorine content increased to $x = 1$. The enlarged bandgap obtained with fluorine substitution is attributed not only to the electronegativity difference between the oxygen and fluorine ions but also to the reduction of iron ions, as observed in $La_{1-x}Sr_xFeO_3$ [113,118].

Theoretical calculation analysis

To investigate the band structure in detail, I performed DFT +*U* calculations for $SrFeO_2F$. Figures 4-12(a) and 4-12(b) show structural models of *cis*- and *trans*-type FeO_4F_2 octahedra in $SrFeO_2F$, respectively. The *cis*-type FeO_4F_2 cluster had an F–Fe–F bond with an angle slightly less than 90° and several distorted O–Fe–O bonds with angles ranging from 161° to 168°. The distortion is considered to originate from the F^- substitution, as the Fe–O and Fe–F bonds have different bond distances [112]. On the other hand, the F–Fe–F and O–Fe–O bond angles in *trans*-type FeO_4F_2 were not altered from 180°.

Previous X-ray diffraction studies showed that bulk $SrFeO_2F$ mainly comprises *cis*-type FeO_4F_2 octahedra [32,120]. The ratio of the *cis* and *trans* configurations was evaluated to be (87 : 13) [120] or (65 : 35) [32] for the bulk $SrFeO_2F$ specimens synthesized by the fluorination of $SrFeO_2$ with XeF_2 and the annealing of $SrFeO_{3-\delta}$ with PVDF, respectively. Figure 4-12(c) depicts the total energies and bandgaps calculated for twelve different $\sqrt{2} \times \sqrt{2} \times 2$ model $SrFeO_2F$ cells with various FeO_4F_2 octahedral orientations. The bandgaps were determined from the difference in the Kohn–Sham orbital energies with +*U* (Fe 3*d*) = 4 eV. The total energy of $SrFeO_2F$ with *cis*-type FeO_4F_2 (*cis* $SrFeO_2F$) was ~1.2 eV lower than that of $SrFeO_2F$ with *trans*-type FeO_4F_2 (*trans* $SrFeO_2F$), indicating that *cis* $SrFeO_2F$ is more energetically favorable than *trans* $SrFeO_2F$. This is consistent with the results of the local structural analysis. Moreover, the calculated

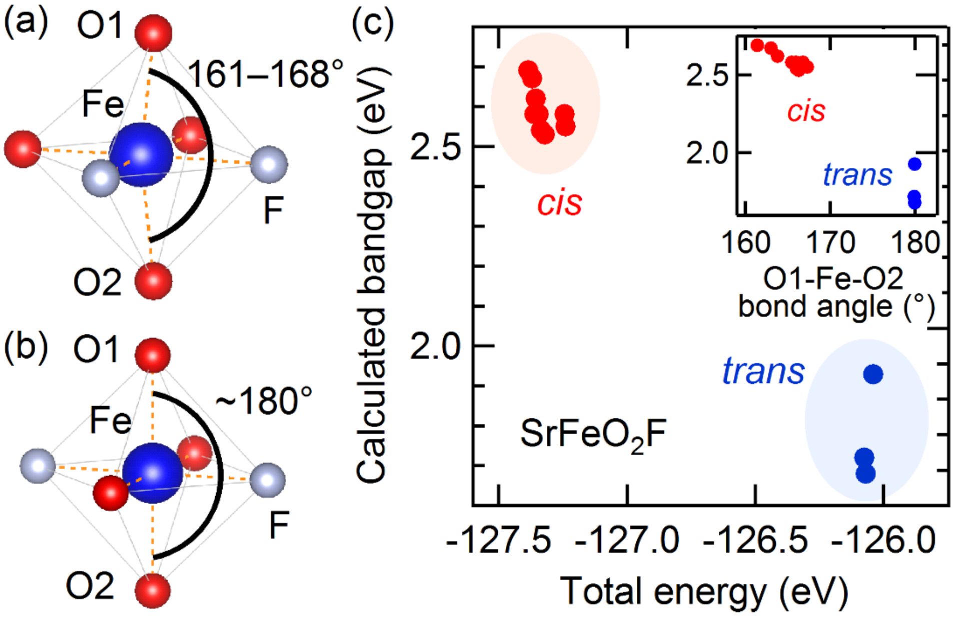

Figure 4-12. Local structures of FeO$_4$F$_2$ octahedra in the (a) *cis* and (b) *trans* SrFeO$_2$F model cells optimized by the GGA +*U* calculation. (c) Calculated bandgap as a function of the total energy. $\sqrt{2} \times \sqrt{2} \times 2$ supercells of SrFeO$_2$F with *cis*-type (red points) and *trans*-type (blue points) FeO$_4$F$_2$ octahedra were assumed. The inset shows the calculated bandgap as a function of the O1–Fe–O2 bond angle.

bandgap of *cis* SrFeO$_2$F (2.5−2.7 eV) was larger than that of LaFeO$_3$ (2.4 eV), whereas that of *trans* SrFeO$_2$F (1.7−1.9 eV) was smaller. Experimentally, the SrFeO$_2$F film has a larger bandgap (2.4 eV) than LaFeO$_3$ (2.1 eV), as shown in Fig. 4-11. These results suggest that the amount of *cis*-type FeO$_4$F$_2$ octahedra is larger than that of *trans*-type one in the SrFeO$_{3-x}$F$_x$ ($x \approx 1$) film.

Figure 4-13(a) shows the calculated band dispersion of *cis* SrFeO$_2$F with the smallest total energy of Fig. 4-12(c). The calculation predicts an insulating band structure with a DFT bandgap of 2.7 eV, where the Fe^{3+} ions have 3d^5 high-spin electron configurations. The top of the valence band is positioned along the X−R line, and the bottom of the conduction band is located at the point X. The dispersion of the conduction band is very small, as expected from the localized character of the Fe 3*d* orbital. Accordingly, there is a very small energy difference (~0.02 eV) between the direct and indirect bandgap values. Thus, *cis* SrFeO$_2$F can be regarded as a direct-bandgap insulator, which agrees with the results of the optical measurements. Figure 4-13(b) shows the calculated total density of states (DOS) and partial DOS for the O 2*p*, F 2*p*, and Fe 3*d* states in *cis* $SrFeO_2F$. The F 2*p* states reside in the energy range of −5.7 to −3.3 eV, which is lower than that of the O 2*p* states. The energetic order of these states is rational considering their electronegativities [121]. The valence band is separated into three regions—upper ($-3.4 < E < 0$ eV), middle ($-5.3 < E < -3.5$ eV), and bottom ($-7.0 < E < -5.3$ eV)—which mainly comprise hybridized O 2*p*−Fe 3*d* states, hybridized F 2*p*−Fe 3*d* states, and Fe 3*d* states, respectively. The conduction band ($2.7 < E < 3.9$ eV) is composed of Fe 3*d* states hybridized with O 2*p*. Thus, the nature of the conduction band and upper valence band is dominated by O–Fe–O bonds.

Next, I discuss the reason why the calculated bandgap differs greatly between

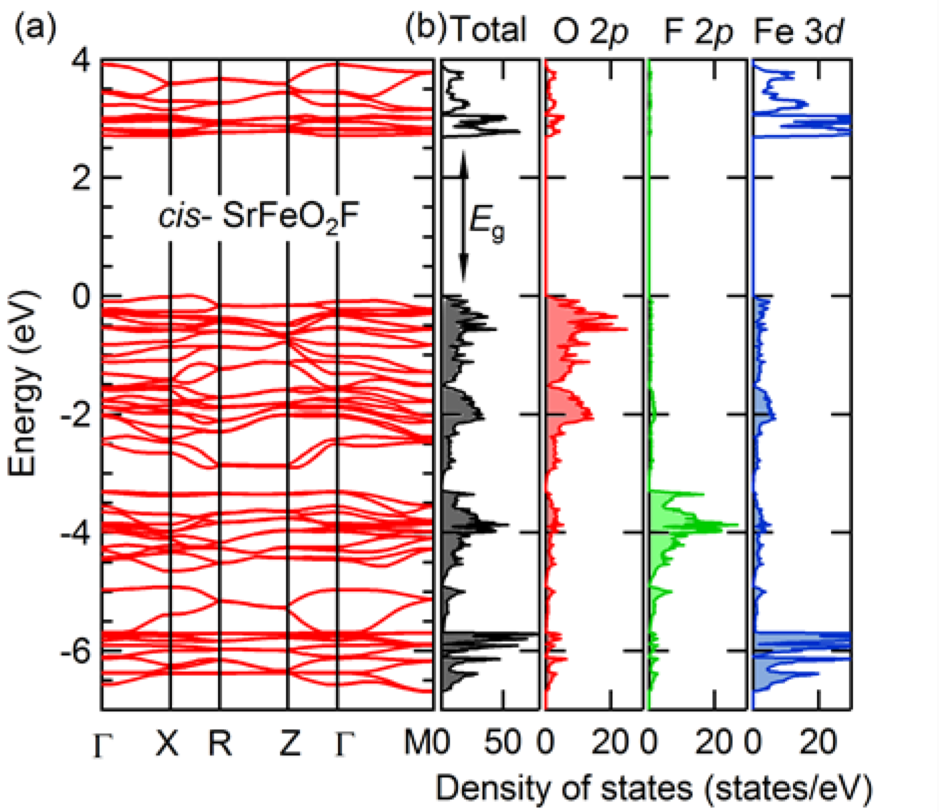

Figure 4-13. (a) Band dispersion of the electronic states and (b) the total DOS and partial O 2*p*, F 2*p*, and Fe 3*d* DOS for *cis* $SrFeO_2F$ obtained by the GGA +*U* calculation. The origin of the orbital energy is set at the Fermi energy.

cis and *trans* $SrFeO_2F$ despite their identical chemical compositions. Figure 4-14 compares the calculated DOS of the conduction band and upper valence band for *cis* and *trans* $SrFeO_2F$. The upper valence band of *trans* $SrFeO_2F$ is a hybrid of O 2*p* and Fe 3*d* states as well. As shown in the figure, the bandwidths of the conduction and upper valence bands for *cis* $SrFeO_2F$ are smaller than those of *trans* $SrFeO_2F$, yielding the larger bandgap of *cis* $SrFeO_2F$. The smaller bandwidths of *cis* $SrFeO_2F$ are attributed to the larger distortion of the O–Fe–O bonds in the FeO_4F_2 octahedra, as shown in Fig. 4-12, because the distortion suppresses the orbital overlaps between iron and oxygen. A similar bandgap widening due to the decreased bond angle was reported for other perovskite-type oxides, such as $ASnO_3$ (A = alkali earth metal) and $LnNiO_3$ (Ln = lanthanide) [122,123].

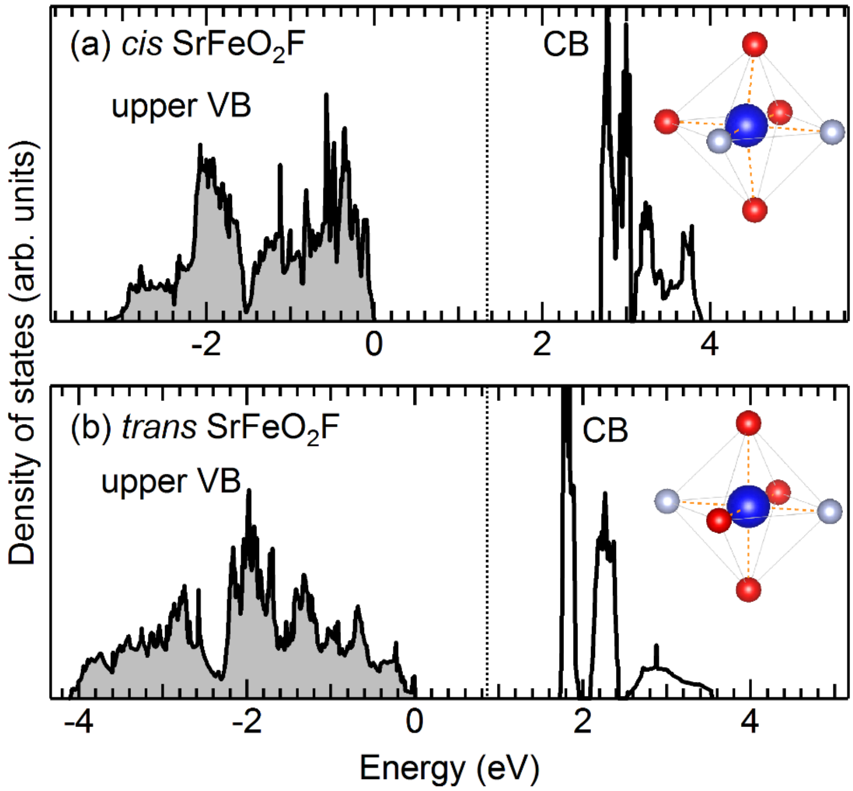

Figure 4-14. DOS of the upper valence band (VB) and conduction band (CB) for (a) *cis* $SrFeO_2F$ and (b) *trans* $SrFeO_2F$ obtained by the GGA +*U* calculation. The dotted lines are drawn at the midpoint between the conduction-band minimum and valence-band maximum. The insets show the local structures of the FeO_4F_2 octahedra.

Experimental electronic structure analysis

To experimentally observe the valence and conduction bands of the $SrFeO_{3-x}F_x$ ($x \approx 1$) film, XPS and XAS measurements were performed. Figure 4-15 shows the valence-band XPS and O *K*-edge XAS spectra of the $SrFeO_{3-x}F_x$ ($x \approx 1$) film. The valence band was spread in the range of −(0−10) eV, which is broader than that of the DFT-based calculated valence band, as shown in Fig. 4-14(b). By comparing the valence-band XPS spectrum with the DFT-based calculations in detail, I assigned the experimental DOS at −(0−5.5) eV, ~ −6.5 eV, and ~ −8 eV to the hybridized O 2*p*−Fe 3*d* states, hybridized F 2*p*−Fe 3*d* states, and Fe 3*d* states, respectively. The O *K*-edge XAS spectrum for the $SrFeO_{3-x}F_x$ ($x \approx 1$) film corresponds to the transitions to the unoccupied O 2*p* states hybridized with Fe 3*d* and Sr 4*d*. As shown in Fig. 4-15, the peaks at 2−6 eV are assigned to Fe 3*d*-derived states, and those at ~10 eV are assigned to Sr 4*d*-derived states. The Fe 3*d*-derived states exhibit a doublet structure, which is also indicated by the DFT-based calculations. This is attributed to the crystal-field splitting of Fe 3*d* into t_{2g} and e_g orbitals [113].

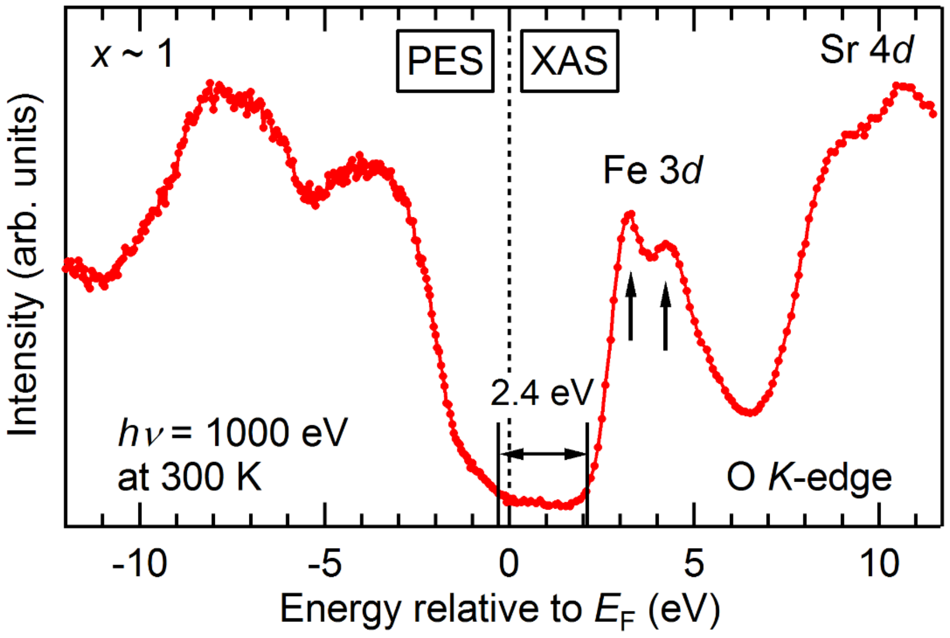

Figure 4-15. Valence-band photoemission and O *K*-edge X-ray absorption spectra of the $SrFeO_{3-x}F_x$ ($x \approx 1$) film.

4.3.3 Synthesis of $SrCoO_xF_y$ films

Brief introduction of $SrCoO_xF_y$

Recently, some perovskite-related Co oxyfluorides displaying antiferromagnetic spin ordering have been synthesized, including $SrCoO_{2.5}F_{0.5}$ [27] and $LaSrCoFeO_5F$ [43], hexagonal perovskite-type $Ba_6Co_6F_{0.93}O_{16}$ and $Ba_5Co_5F_{0.77}O_{12.88}$ [22,44], layered-type Sr_2CoO_3F [25,124], and cation ordered $Ba_2YCoO_5F_{0.42}$ [125]. These Co oxyfluorides tend to have higher Co valence states between +3 and +4. For instance, bulk $SrCo^{3.5+}O_{2.5}F_{0.5}$ can be obtained by fluorination of the $SrCo^{3+}O_{2.5}$ precursor using F_2 gas [27]. During this fluorination process, F^- ions are inserted into the oxygen vacancy sites of $SrCoO_{2.5}$ and the Co ions are oxidized from Co^{3+} to $Co^{3.5+}$. The wide variation in the Co valence state is expected to lead to interesting electronic properties, as seen in hole- or electron-doped perovskite cobalt oxides $La^{3+}{}_{1-x}A_xCoO_3$ (A = Sr^{2+} or Ce^{4+}) [126,127]. However, a perovskite Co oxyfluoride with relatively lower-valent $Co^{2+/3+}$ has not yet been reported.

Topotactic fluorination technique using PVDF, which promotes not only insertion of $F^–$ but also substitution of $F^–$ for $O^{2–}$, would enable to fabricate new perovskite-related Co oxyfluorides with relatively lower-valent $Co^{2+/3+}$. Thus, I attempted topotactic fluorination on $SrCoO_{2.5}$ epitaxial thin films using PVDF.

Crystal structure analysis

Figure 4-16(a) shows the measured 2θ–θ X-ray diffraction (XRD) pattern (χ = 90°) for the $SrCoO_{2.5}$ precursor film. The 006, 008, and $00\underline{10}$ diffraction peaks were clearly observed, indicating that the $SrCoO_{2.5}$ precursor film had a c-axis-oriented brownmillerite structure, in which the tetrahedral CoO_4 and octahedral CoO_6 sub-layers were alternately stacked. The XRD reciprocal space map (RSM) for $11\underline{12}$ diffraction of the $SrCoO_{2.5}$ film is shown in Fig. 4-17(a). Notably, the q_x value of the $SrCoO_{2.5}$ $11\underline{12}$ peak coincided with that of STO (103), proving that the $SrCoO_{2.5}$ film had coherently grown on the STO substrate. Thus, the structure of the $SrCoO_{2.5}$ films was defined by a pseudo-tetragonal cell with lattice constants of $a/\sqrt{2}$ = 3.905 Å and $c/4$ = 3.937 Å.

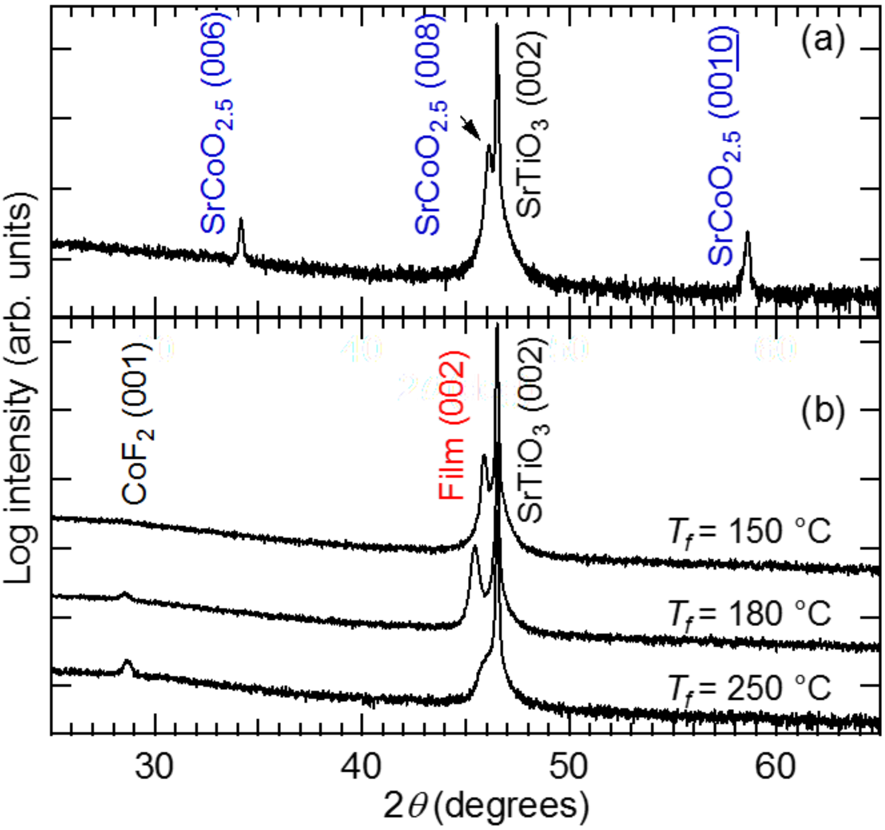

Figure 4-16. 2θ–θ X-ray diffraction patterns of (a) $SrCoO_{2.5}$ precursor film and (b) $SrCoO_xF_y$ films fluorinated with PVDF at T_f = 150, 180, and 250 °C for 12 h.

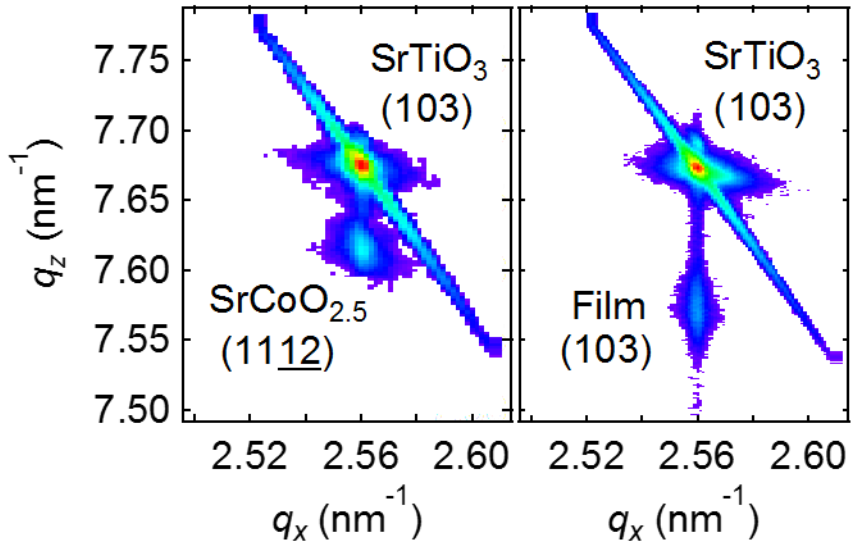

Figure 4-17. Reciprocal space maps around $SrTiO_3$ (103) diffraction peaks measured for (a) $SrCoO_{2.5}$ precursor film, and (b) $SrCoO_xF_y$ film fluorinated at T_f = 150 °C.

Figure 4-16(b) compares the 2θ–θ XRD patterns (χ = 90°) of the $SrCoO_xF_y$ films obtained by fluorination of the $SrCoO_{2.5}$ precursor at T_f = 150, 180, and 250 °C, for 12 h. The $SrCoO_xF_y$ film prepared at 150 °C exhibited only the 002 diffraction peak of the perovskite structure without that of the brownmillerite $SrCoO_{2.5}$, implying that the fluorination reaction proceeded at 150 °C. As seen from the RSM in Fig. 4-17(b), the *a*-axis of the film was completely locked to the STO lattice after the reaction with PVDF. Therefore, the perovskite-type cation network was maintained during the PVDF fluorination process. The lattice constants of the fluorinated film were estimated to be a = 3.905 Å and c = 3.955 Å. At 180 °C, an impurity peak assignable to CoF_2 001 appeared, and the perovskite phase decomposed above 250 °C.

Composition Analysis

In order to verify F doping, EDS measurements were conducted for K_α of O and F, and L_α of Co and Sr. Figures 4-18(a) and 4-18(b) depict EDS spectra near the O and F K_α peaks of the $SrCoO_{2.5}$ precursor film and the $SrCoO_xF_y$ film fluorinated at 150 °C, respectively, where the spectral intensity was normalized by the area of Co L_α peak. After PVDF fluorination, the F K_α peak emerged and the peak area intensity of O K_α peak decreased by ~24%. This suggested that fluorine ions were not only inserted into the oxygen vacancy sites, but also partially substituted for oxygen ions during the fluorination reaction. From the peak area ratio of O K_α / Co L-lines, the O content (x) of the $SrCoO_xF_y$ film was estimated to be ~1.9. Furthermore, the F content of the film was quantitatively determined using NRA measurements. Figure 4-18(c) shows an NRA spectrum of the $SrCoO_xF_y$ film fluorinated at 150 °C. The γ-ray emitted by the nuclear reaction of $^{19}F(p,\alpha\gamma)^{16}O$ was clearly observed in the $SrCoO_xF_y$ film, and the F content (y) was deduced to be 0.51 ± 0.10. Therefore, the chemical composition of the film fluorinated at 150 °C was formulated as $SrCoO_{1.9\pm0.4}F_{0.5\pm0.1}$.

As seen from Figs. 4-17(a) and 4-17(b), the q_z value of 103 diffraction for the $SrCoO_{1.9\pm0.4}F_{0.5\pm0.1}$ film was smaller than that of $11\underline{12}$ diffraction for the $SrCoO_{2.5}$

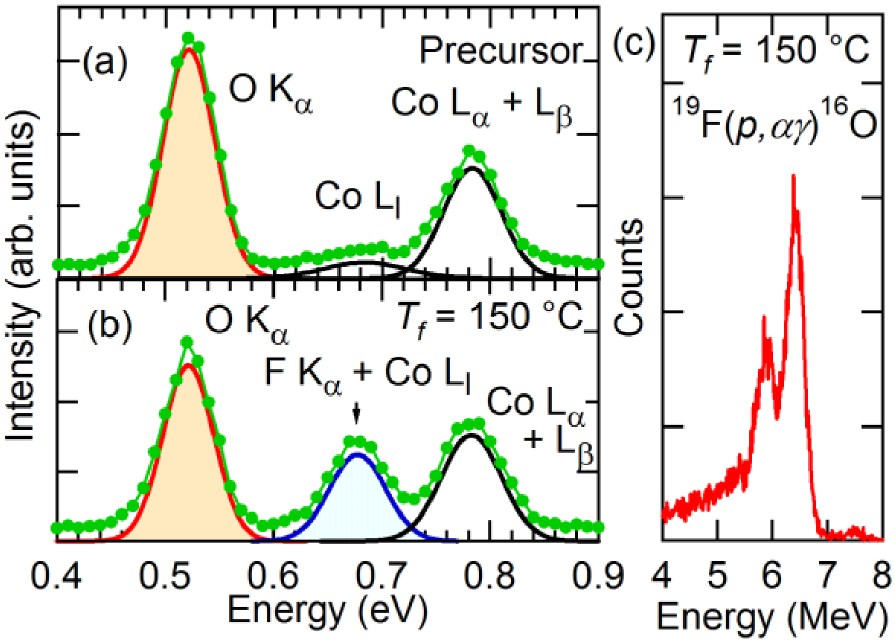

Figure 4-18. EDS near the O K_α, F K_α, and Co L_α peaks of (a) $SrCoO_{2.5}$ precursor film and (b) $SrCoO_xF_y$ film fluorinated at T_f = 150 °C. (c) A nuclear reaction analysis spectrum of $SrCoO_xF_y$ film fluorinated at 150 °C.

precursor film. This implied that the expansion of the *c*-axis length occurred during the PVDF fluorination. The cell volume (V) increased from $V/8$ = 60.0 Å^3 for the $SrCoO_{2.5}$ film to V = 60.3 Å^3 for the $SrCoO_{1.9\pm0.4}F_{0.5\pm0.1}$ film. In contrast, bulk $SrCoO_{2.5}F_{0.5}$ prepared by fluorination of $SrCoO_{2.5}$ using F_2 gas was reported to have a smaller cell volume (V = 57.4 Å^3) than the precursor $SrCoO_{2.5}$ ($V/8$ = 60.0 Å^3) because of the increase of the Co valence state from +3 to +3.5 [27,112]. This data suggested that the mechanism of PVDF fluorination was different from that using F_2 gas.

Oxidation state analysis

To analyze the Co valence state, XPS measurements were performed of the Co core levels. Figure 4-19 compares the Co 2*p* spectra of the $SrCoO_{2.5}$ precursor film and the $SrCoO_{1.9\pm0.4}F_{0.5\pm0.1}$ film fluorinated at 150 °C. Each spectrum showed Co $2p_{3/2}$ and $2p_{1/2}$ peaks at binding energies (E_b) of ~780 and ~795 eV, respectively. In addition, the $SrCoO_{2.5}$ precursor film exhibited two weak satellite peaks at ~785 and ~789 eV. A weak satellite feature at ~789 eV has often been observed in perovskite cobalt oxides with Co^{3+}, such as $La_{1-x}Sr_xCoO_3$ ($x = 0.0–0.4$) and $LaCoO_{3-\delta}$ [128,129]. On the other hand, the weak satellite peak at ~785 eV was possibly due to Co^{2+}, as seen in CoO ($E_b = 785.5$ eV) [130]. This suggests that the majority of the Co ions in the $SrCoO_{2.5}$ precursor film have trivalent states, however, a fraction of the Co ions are divalent, due to the formation of O vacancies. Meanwhile, in the $SrCoO_{1.9\pm0.4}F_{0.5\pm0.1}$ film, the satellite peak at ~786 eV was more enhanced, indicating that the fraction of divalent Co ions was increased by the PVDF fluorination. In other words, the PVDF was acting as a reducing agent for the $SrCoO_{2.5}$ film, in sharp contrast to F_2 gas, which oxidizes the Co ions in the same film. The c-axis length expansion, as mentioned above, can be reasonably explained by the PVDF reduction of Co, because Co^{2+} has a larger ionic radius than Co^{3+} [131]. Assuming that the chemical composition of the film was $SrCoO_{1.9}F_{0.5}$, the Co valence state was calculated to be +2.3.

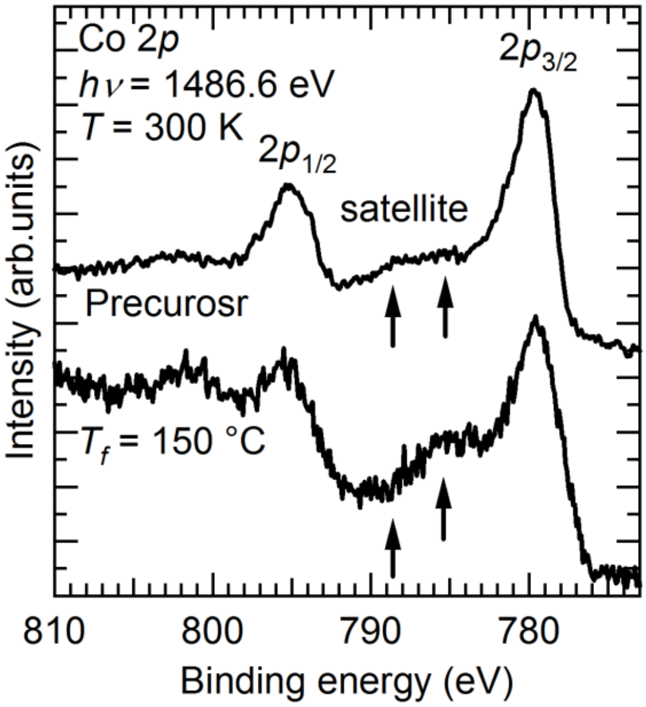

Figure 4-19. Co $2p$ core-level X-ray photoemission spectra of the $SrCoO_{2.5}$ precursor film and $SrCoO_xF_y$ film fluorinated at $T_f = 150$ °C.

4.3.4 Magnetic properties of $SrCoO_xF_y$ films

Figure 4-20 shows the magnetic field dependence of the in-plane magnetization of the $SrCoO_{1.9\pm0.4}F_{0.5\pm0.1}$ film at 10 K. No clear hysteresis was observed and the saturation magnetization was smaller than 0.02 μ_B/Co, indicating no sign of ferromagnetism. The precursor material $SrCoO_{2.5}$ is known to be antiferromagnetic [97]. I speculate that the $SrCoO_{1.9\pm0.4}F_{0.5\pm0.1}$ film has antiferromagnetic properties, as reported in the Co-based oxyfluorides with higher valence states of Co, though at present I have no direct evidence for the antiferromagnetism in this film.

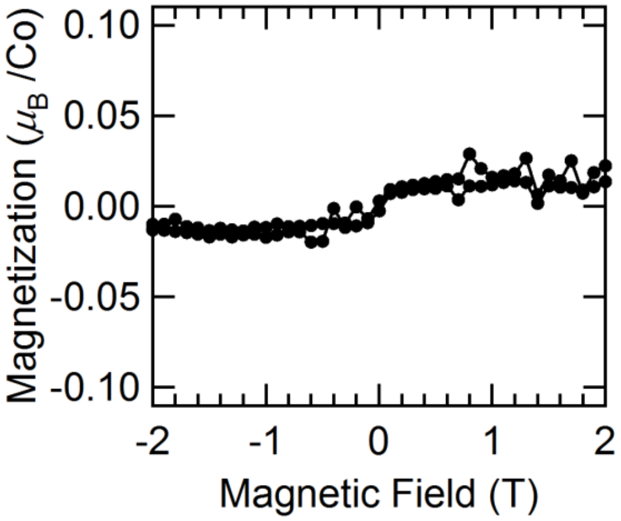

Figure 4-20. In-plane magnetization vs magnetic field at 10 K measured for the $SrCoO_xF_y$ film fluorinated at 150 °C.

4.4 Conclusion

I successfully synthesized the $SrFeO_{3-x}F_x$ epitaxial thin films on STO substrates via topotactic fluorination of $SrFeO_{3-\delta}$ precursor films using PVDF. The $SrFeO_{3-x}F_x$ thin films were obtained at a lower temperature than polycrystalline bulk samples. Furthermore, the fluorine content in the $SrFeO_{3-x}F_x$ films was controllable by adjusting the fluorination temperature and/or the amount of oxygen vacancies in the precursor film. The higher fluorination reactivity in the $SrFeO_{3-\delta}$ precursor film, compared with that observed in bulk samples, can be rationalized by taking smaller grain sizes, being the maximum length of the diffusion path, into account within the framework of the fluorine-diffusion model via oxygen vacancy. In addition, the electronic structure of the perovskite $SrFeO_{3-x}F_x$ ($0.6 \leq x \leq 1$) films was investigated by optical absorption, XPS, and XAS measurements, as well as DFT-based calculations. The optical bandgap of the $SrFeO_{3-x}F_x$ film increased systematically as the fluorine content increased, and the $SrFeO_2F$ film exhibited a direct optical bandgap of 2.4 eV, which is larger than the direct gap of 2.1 eV for a $LaFeO_3$ film. The DFT calculations suggested that the wider bandgap of the $SrFeO_2F$ film originated from the O–Fe–O bond distortion in the *cis*-type FeO_4F_2 octahedra. The valence-band XPS spectrum of the $SrFeO_{3-x}F_x$ ($x \approx 1$) film showed finite DOS at $-(0-5.5)$ eV, ~ -6.5 eV, and ~ -8 eV, which were assigned to the hybridized O 2*p*−Fe 3*d* states, hybridized F 2*p*−Fe 3*d* states, and Fe 3*d* states, respectively. The O *K*-edge XAS spectrum of the $SrFeO_{3-x}F_x$ ($x \approx 1$) film exhibited two peaks in the Fe 3*d*-derived conduction band, which were attributed to the splitting of Fe 3*d* into t_{2g} and e_g orbitals.

I also successfully fabricated anion-vacant perovskite $SrCoO_xF_y$ epitaxial thin films with $Co^{2+/3+}$ on STO substrates via topotactic fluorination of $SrCoO_{2.5}$ precursor films using PVDF at 150 °C. The Co valence state of the $SrCoO_{1.9\pm0.4}F_{0.5\pm0.1}$ film was smaller than that of the $SrCoO_{2.5}$ precursor film, indicating that the PVDF acted as a reducing agent. With the reduction of Co, the cell volume increased. The $SrCoO_{1.9\pm0.4}F_{0.5\pm0.1}$ film did not show ferromagnetism down to 10 K, suggesting the presence of antiferromagnetic interactions between the Co ions.

Chapter 5 Topotactic reduction: metallic conductivity in infinite layer $SrFeO_2$ films

5.1 Introduction

Iron oxides with square planar coordination, e.g., $SrFeO_2$, can be synthesized via topotactic low-temperature reduction of $SrFeO_{3-\delta}$ using metal hydrides such as CaH_2 (Fig. 5-1) [58]. $SrFeO_2$ is categorized as a Mott insulator in which the Fe spins (Fe^{2+}: d^6, S = 2) are antiferromagnetically ordered, and exhibits a high Néel temperature of T_N = 473 K [58]. Single-crystalline epitaxial $SrFeO_2$ thin films were also grown on $SrTiO_3$(001) or $KTaO_3$(001) substrates by combining a PLD method with low-temperature reduction using CaH_2 [76,132]. Importantly, since $SrFeO_2$ is isostructural with the infinite-layer cuprate, $SrCuO_2$, in which high-temperature superconductivity can be induced via carrier doping [133], intensive efforts have been made to realize metallic conduction in $SrFeO_2$ through chemical substitution. Such chemical pressure has been investigated in $AFeO_2$ (A = Ca^{2+} and Ba^{2+}) [59,60]. The B-site substitutions have been also investigated in $SrFe_{0.7}M_{0.3}O_2$ (M = Co^{2+} and Mn^{2+}) [134,135] and $SrFe_{0.5}Ru^{2+}{}_{0.5}O_2$ [61]. In both cases, chemical substitution tended to weaken the antiferromagnetic interaction, similar to the effect of physical pressure [136], but the obtained compounds remained insulating. To

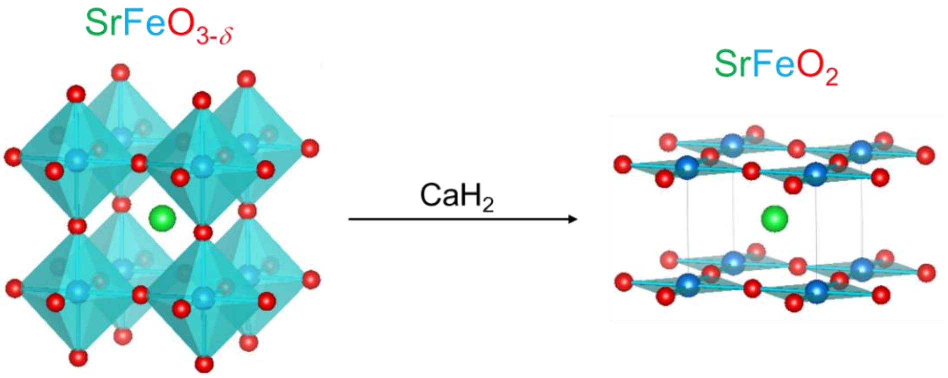

Figure 5-1. Crystal structures of $SrFeO_{3-\delta}$ and $SrFeO_2$.

introduce carriers directly, Matsuyama *et al.* attempted to substitute Eu^{3+} for Sr^{2+} in $SrFeO_2$ thin films and found that 10 % Sr/Eu replacement could generate *n*-type carriers at concentrations on the order of 10^{19} cm^{-3} [137]. Although the resistivity (ρ) of the films substantially decreased upon carrier doping, the ρ vs. temperature (ρ–T) curve was characterized by a negative $d\rho/dT$ slope at low temperatures, indicating an insulating state.

Ideally, doping of a considerably small amount of carriers can destabilize a Mott insulator and cause an insulator-to-metal (I-M) transition. However, real materials generally contain disorders, such as defects and substituted ions, which prevent the I-M transition. Therefore, to induce the I-M transition in $SrFeO_2$ by carrier doping, high quality single crystalline samples with less disorders are needed.

In this chapter, I have investigated the structural and transport properties of single-crystalline $SrFeO_2$ thin films grown on perovskite substrates with various lattice parameters. I found that the film with the highest crystallinity on lattice-matched $KTaO_3$(001) substrate exhibits metallic transport behavior with a carrier density of 3.1 × 10^{18} cm^{-3}. Additionally, I also tried to improve conductivity and crystallinity of the $SrFeO_2$ films by Sm substitution. Based on the results, I will discuss the structural and transport properties of the $SrFeO_2$ and $Sr_{1-x}Sm_xFeO_2$ films.

5.2 Method

Synthesis method for $SrFeO_2$ film

$SrFeO_{3-\delta}$ ($0 < \delta \leq 0.5$) precursor films were grown on STO(001), $DyScO_3$(110) (DSO, CrysTec GmbH), and $KTaO_3$(001) (KTO, MTI Corporation) substrates by PLD technique. STO and KTO have cubic structures with lattice constants of a = 3.905 Å and 3.995 Å, respectively, while DSO has a slightly distorted cubic lattice (pseudo-cubic) with a = 3.944 Å. As a PLD target, I used a $SrFeO_{3-\delta}$ ceramic pellet prepared by a solid-state reaction from mixed powders of $SrCO_3$ and α-Fe_2O_3 (pre-sintering at 800 °C for 24 h and sintering at 1200 °C for 12 h). The fourth harmonic of a Nd-YAG laser (wavelength = 266 nm) with an energy of 0.3 J cm^{-2}/shot and a frequency of 10/3 Hz was employed for ablation. Substrate temperature and partial oxygen pressure were kept at 700 °C and 5 × $10^{–5}$ Torr, respectively, during each deposition run. The obtained precursor $SrFeO_{3-\delta}$ films were further subjected to solid-phase reduction using ca. 0.2 g CaH_2 at a temperature of 240–280 °C, for 24 h in evacuated Pyrex tubes. The reduced films were rinsed with 2-butanone to remove any unreacted CaH_2 on the film surfaces. Film thicknesses were measured by a stylus surface profiler (Bruker, Dektak 6M) with typical film thicknesses of ca. 70–80 nm. The $SrFeO_2$ thin films on STO, DSO, and KTO substrates are hereafter referred to as $SrFeO_2$/STO, $SrFeO_2$/DSO, and $SrFeO_2$/KTO, respectively.

Synthesis method for Sm-substituted $SrFeO_2$ films

Brownmillerite $Sr_{1-x}Sm_xFeO_{2.5}$ (x = 0, 0.01, 0.03, 0.05, and 0.1) films were grown on KTO and DSO substrates by PLD technique. As PLD targets, I used $Sr_{1-x}Sm_xFeO_{3-\delta}$ ceramic pellets from mixed powders of Sm_2O_3, $SrCO_3$, and α-Fe_2O_3 by a solid-state reaction (pre-sintering at 800 °C for 24 h and sintering at 1200 °C for 12 h). The fourth harmonic of a Nd-YAG laser (266 nm, 10/3 Hz) with an energy of 0.3 J/cm^2/shot was employed for ablation. Substrate temperature and partial oxygen pressure were kept at 700 °C and 5 × $10^{–5}$ Torr, respectively, during each deposition run. The obtained precursor $Sr_{1-x}Sm_xFeO_{2.5}$ films were further subjected to solid-phase reaction with CaH_2 at a temperature (T_r) of 250–280 °C for 24 h in evacuated Pyrex tubes. The CaH_2-treated films were rinsed with 2-butanone to remove any unreacted CaH_2 on the film surfaces. The typical film thickness measured by a stylus surface profiler was ~70 nm.

Characterization method

Crystal structures of the films were examined by an X-ray diffractometer equipped with a two-dimensional detector (Bruker AXS, Vantec-500) using Cu-$K\alpha$

radiation. In-plane electrical resistivity was measured by the four-probe method, using Al electrodes. Before measurement, samples were cut into rectangular shapes with a size of 1 mm width by 3 mm length. The distance between the voltage electrodes was 2 mm. Carrier density and Hall mobility were characterized on the basis of six-terminal geometry under an external magnetic field up to 9 T, perpendicular to the film surface. XPS and XAS measurements carried out at beamline 2C of the Photon Factory, KEK, Japan. The XPS spectra were acquired with an energy resolution of ca. 0.25 eV at a photon-energy range of 1000 eV. The Fermi levels of the samples were referred to that of Au foil in electrical contact with the samples. The XAS spectrum was measured by the total-electron-yield method. All spectra were measured at room temperature. The chemical composition of the films was analyzed by dynamic SIMS with a depth resolution of ca. 10 nm. For quantification of the hydrogen content, H-implanted $SrTiO_3$ samples were used as references.

5.3 Results and discussion

5.3.1 Synthesis of $SrFeO_2$

Figure 5-2(a) shows 2θ–θ XRD patterns at $\chi = 90°$ measured for $SrFeO_2$/STO, $SrFeO_2$/DSO, and $SrFeO_2$/KTO, prepared by solid-phase reduction at 250 °C. 002 Diffraction peaks at $2\theta \approx 52°$, corresponding to the infinite-layer structure, were clearly observed in all samples, although the peak for $SrFeO_2$/DSO was somewhat diminished. No impurity phases such as SrO, FeO, and *b*-axis-oriented $SrFeO_{2.5}$ (brownmillerite, $2\theta \approx 59°$) were detected. At $\chi = 45°$, as shown in Figure 5-2(b), infinite-layer $SrFeO_2$ 011 diffraction peaks were clearly observed at $2\theta \approx 34°$ in all samples. The *a*- and *c*-axis lengths of the films are calculated to be $a = 0.398$ nm and $c = 0.3495$ nm (on STO), $a = 0.402$ nm and $c = 0.3493$ nm (on DSO), and $a = 0.398$ nm and $c = 0.3483$ nm (on KTO), while the lattice constants of bulk $SrFeO_2$ were reported to be $a = 0.3991$ nm and $c =$

0.3475 nm [58]. The full-width-half-maximum values of the rocking curves for the 002 diffraction, $\Delta\omega(002)$, were 2.08°, 1.27°, and 0.96°, respectively, in good coincidence with the lattice mismatch between bulk $SrFeO_2$ and each substrate, −2.2, −1.2, and −0.05%, respectively. This indicates that the $SrFeO_2$ films grown on lattice-matched KTO

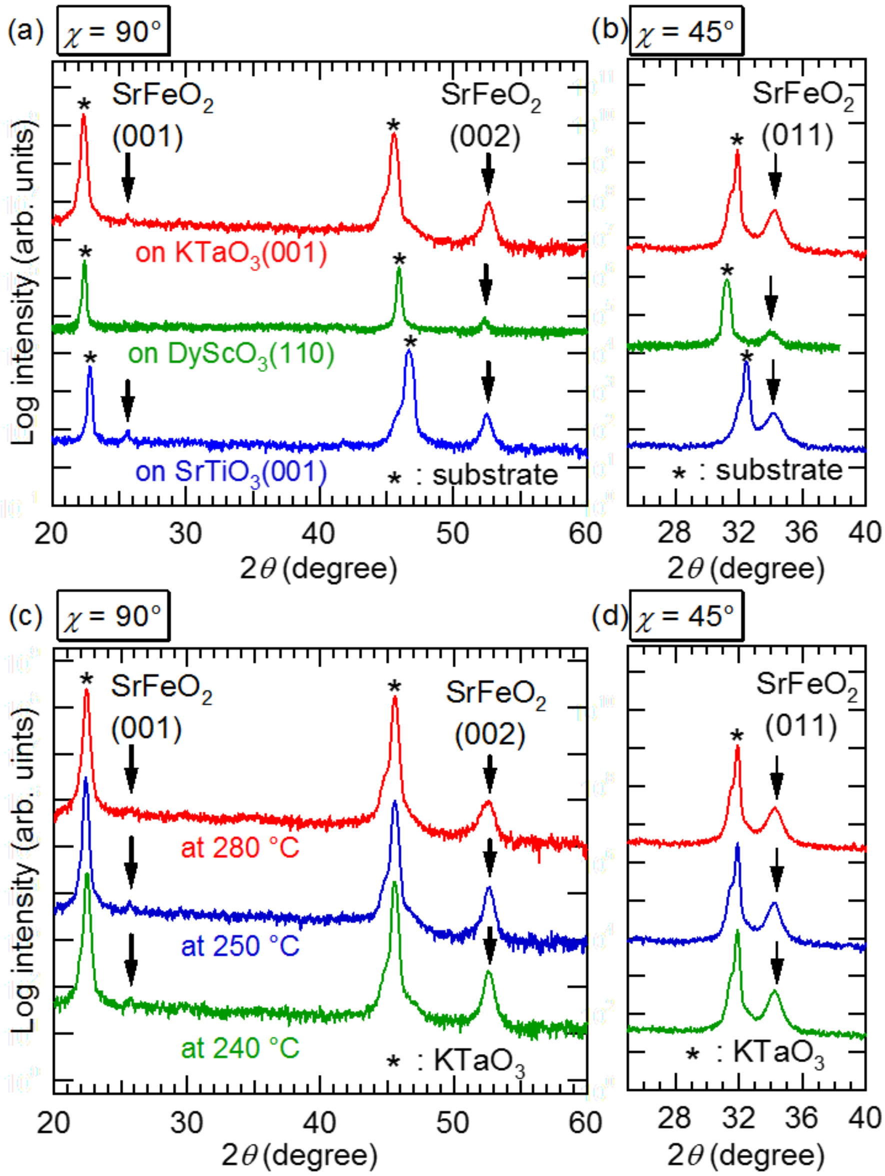

Figure 5-2. 2θ–θ XRD patterns at (a) $\chi = 90°$ and (b) $\chi = 45°$ measured for $SrFeO_2$ films on $SrTiO_3(001)$, $DyScO_3(110)$, and $KTaO_3(001)$ substrates prepared at 250 °C, and at (c) $\chi = 90°$ and (d) $\chi = 45°$ for $SrFeO_2$ films on $KTaO_3(001)$ substrate prepared at 240, 250, and 280 °C. The diffraction patterns at $\chi = 45°$ were obtained by integrating the peak intensities on the detector along χ direction from 43° to 53°.

substrates were of higher quality than those on STO and DSO substrates.

Figure 5-2(c) shows the 2θ–θ XRD patterns (χ = 90°) of $SrFeO_2$/KTO reduced at 240, 250, and 280 °C. Although all films exhibit the 001 and 002 diffraction peaks corresponding to the infinite-layer structure, the respective peaks of the film prepared at 280 °C are fairly weak and broadened. The infinite-layer $SrFeO_2$ 011 diffraction peak was observed as well in all XRD patterns at χ = 45°, as shown in Figure 5-1(d). The *a*- and *c*-axis length of the 240, 250, and 280 °C samples were calculated to be a = 0.398 nm and c = 0.3484 nm (240 °C), a = 0.398 nm and c = 0.3483 nm (250 °C), and a = 0.397 nm and c = 0.3492 nm (280 °C), while $\Delta\omega$(002) of these films measured 0.98, 0.96, and 1.13°, respectively. These results confirm the positive correlation between *c*-axis length and crystallinity. The highest crystallinity was obtained for $SrFeO_2$/KTO that was heat-treated at 250 °C.

5.3.2 Properties of $SrFeO_2$

Transport properties of the $SrFeO_2$ thin films

Figure 5-3(a) compares the ρ–T curves of the $SrFeO_2$ films prepared on the different substrates. The ρ–T curves of $SrFeO_2$/STO and $SrFeO_2$/DSO show insulating behavior with $d\rho/dT < 0$, being consistent with the electric properties of bulk $SrFeO_2$ [58]. In contrast, $SrFeO_2$/KTO demonstrates metallic behavior with $d\rho/dT > 0$. The ρ(300 K) value of $SrFeO_2$/KTO is 2.0×10^{-1} Ω cm, which is approximately four orders of magnitude lower than that of $SrFeO_2$/STO (1.4×10^{3} Ω cm) and $SrFeO_2$/DSO (4.0×10^{3} Ω cm).

Figure 5-3(b) compares the ρ–T curves of $SrFeO_2$/KTO prepared at 240, 250, and 280 °C. The ρ(300 K) value of 7.4×10^{-1} Ω cm of the film prepared at 280 °C is considerably higher than the ρ(300 K) prepared at 240 and 250 °C (2.3×10^{-1} and 2.0×10^{-1} Ω cm, respectively). Furthermore, the film prepared at 280 °C exhibits an I-M transition at 58 K, while the films prepared at 240 and 250 °C are metallic ($d\rho/dT > 0$) over the whole temperature range below 300 K.

Figure 5-4 plots ρ(300 K) as a function of $\Delta\omega$(002) for $SrFeO_2$/STO and

$SrFeO_2$/KTO. As is clear from this figure, ρ(300 K) decreases with decreasing $\Delta\omega$(002), indicating that the metallic $SrFeO_2$ phase only appears when a good crystallinity (i.e., $\Delta\omega(002) < 1\,°$) is achieved. This finding can be rationalized by the fact that the densities of the various crystalline defects are reduced with improved lattice matching between film and substrate, i.e., with increasing crystallinity. Charged defects such as edge dislocation could trap the conducting electrons, resulting in a decreased carrier density [138].

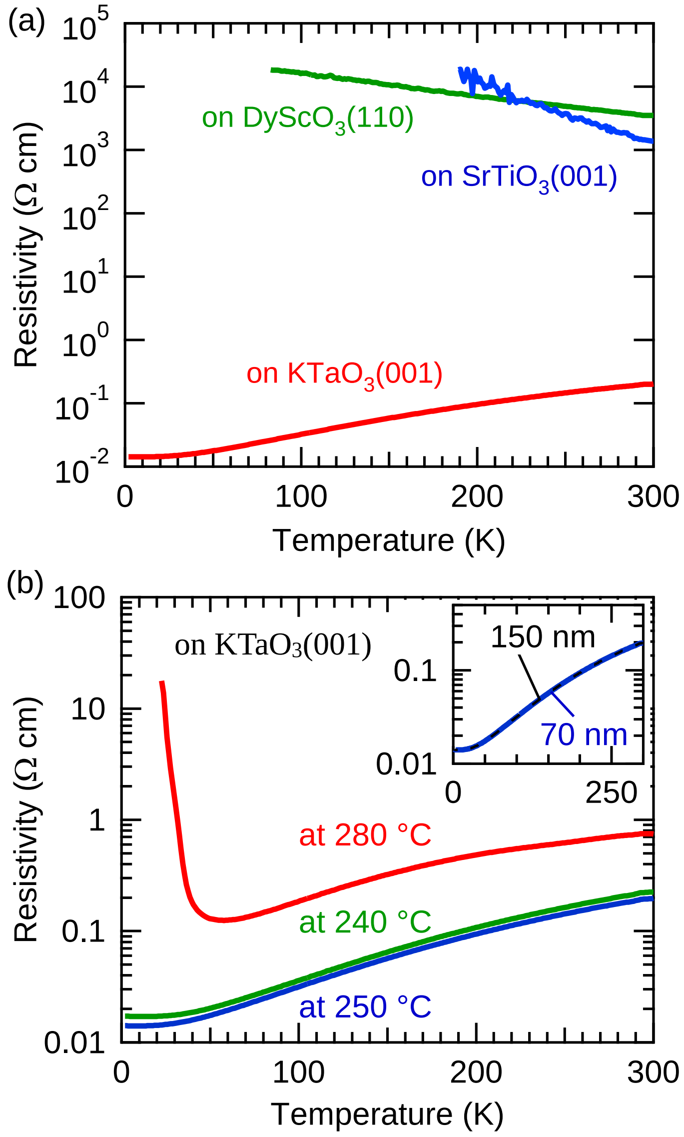

Figure 5-3. ρ–T curves for (a) the $SrFeO_2$ thin films on STO(001), DSO(110), and KTO(001) substrates prepared at 250 °C and (b) $SrFeO_2$ on KTO(001) prepared at 240, 250, and 280 °C. The inset in figure 3(b) depicts the ρ–T curves for the 70- and 150-nm-thick $SrFeO_2$ thin films on KTO(001), prepared at 250 °C.

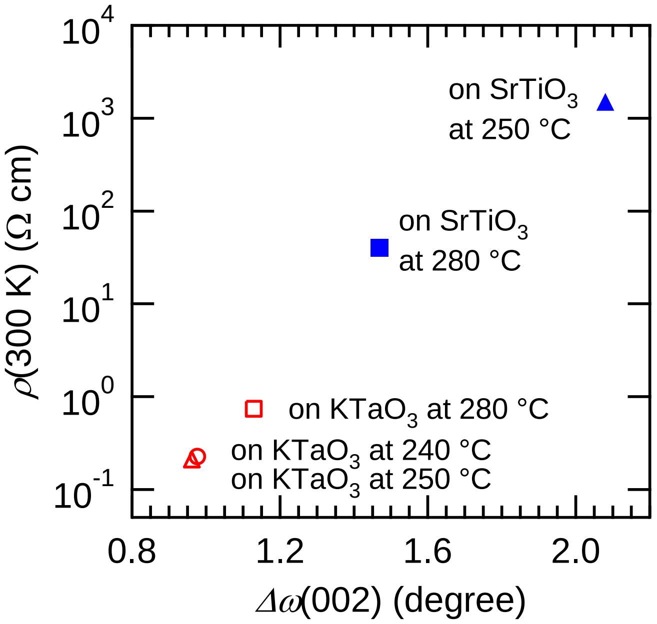

Figure 5-4. Resistivity at 300 K (ρ(300 K)), as a function of the full-width-half-maximum values of the rocking curves for the (002) diffraction (i.e., $\Delta\omega$(002)), for SrFeO$_2$ thin films on SrTiO$_3$(001) and KTaO$_3$(001) substrates.

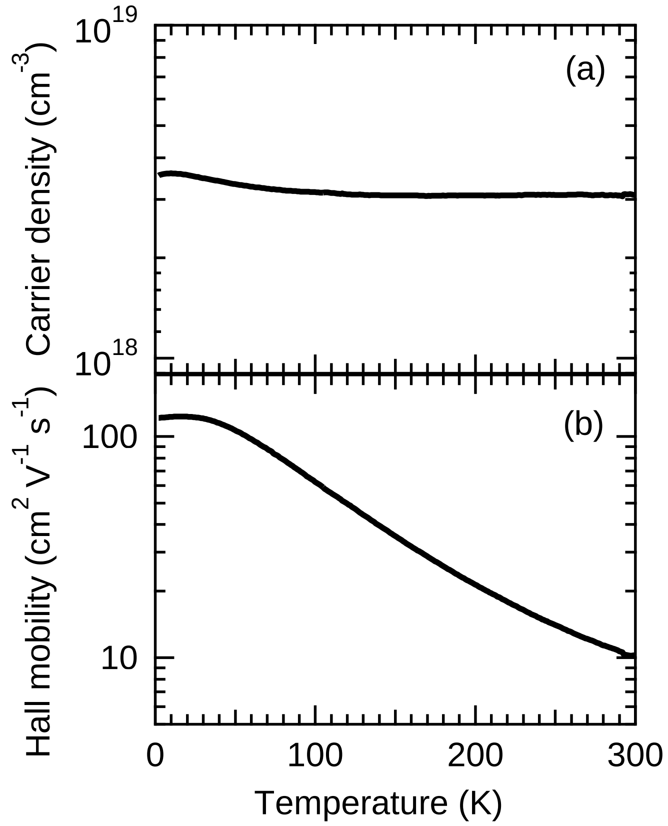

Figure 5-5. Temperature dependence of (a) the carrier density and (b) the Hall mobility for SrFeO$_2$ thin films on KTaO$_3$(001), prepared at 250 °C.

Figure 5-5 shows the carrier density (n_e) and Hall mobility (μ_H) of $SrFeO_2$/KTO prepared at 250 °C as a function of temperature. Because the Hall coefficient is negative, the electrons carry charge, while n_e is nearly independent of temperature, being a typical characteristic of metals (Fig. 5-5(a)). Remarkably, the n_e(300 K) value is estimated to be 3.1×10^{18} cm^{-3}. In contrast, the μ_H(300 K) value of 10.2 cm^2 V^{-1} s^{-1} is considerably higher than that of bulk $SrFeO_{3-\delta}$ (between 10^{-3}–1.0 cm^2 V^{-1} s^{-1}) and bulk $La_{1-x}Sr_xFeO_{3-\delta}$ (between 10^{-2}–0.3 cm^2 V^{-1} s^{-1}) [139,140] and comparable to that of infinite-layer cuprate $Sr_{0.9}La_{0.1}CuO_2$ (> 42 cm^2 V^{-1} s^{-1}) [141]. This observation suggests that the infinite-layer structure facilitates a high mobility.

Fe oxidation state of the $SrFeO_2$ thin films

The oxidation state of Fe in the $SrFeO_2$ thin films was probed by Fe 2*p* core-level XPS measurements. Figure 5-6 shows the Fe 2*p* core-level spectra of $SrFeO_2$/KTO prepared at 250 °C and $SrFeO_2$/STO prepared at 280 °C, as well as the spectrum of the precursor $SrFeO_{2.5}$/STO [115]. Each spectrum is characterized by a Fe $2p_{1/2}$–Fe $2p_{3/2}$ doublet and a weak satellite peak located between the doublet peaks. The Fe 2*p* spectrum of $SrFeO_2$/KTO shows the satellite peak to occur at a binding energy of ~715 eV, which is similar to the spectrum of $SrFeO_2$/STO. On the other hand, the satellite peak of $SrFeO_{2.5}$/STO is located at ~718 eV. By comparison of these spectra with previously reported XPS spectra of various Fe oxides [114], I determined the oxidation states of Fe in $SrFeO_2$/KTO, $SrFeO_2$/STO, and $SrFeO_{2.5}$/STO to be close to +2, +2, and +3, respectively. The carrier density of the conducting $SrFeO_2$/KTO, 3.1×10^{18} cm^{-3}, is about four orders of magnitude lower than that of Fe density, 1.8×10^{22} cm^{-3}. Thus, 10^{-4} of the total Fe should be present as Fe^+. Such small quantities are, however, outside the resolution of the XPS instrument.

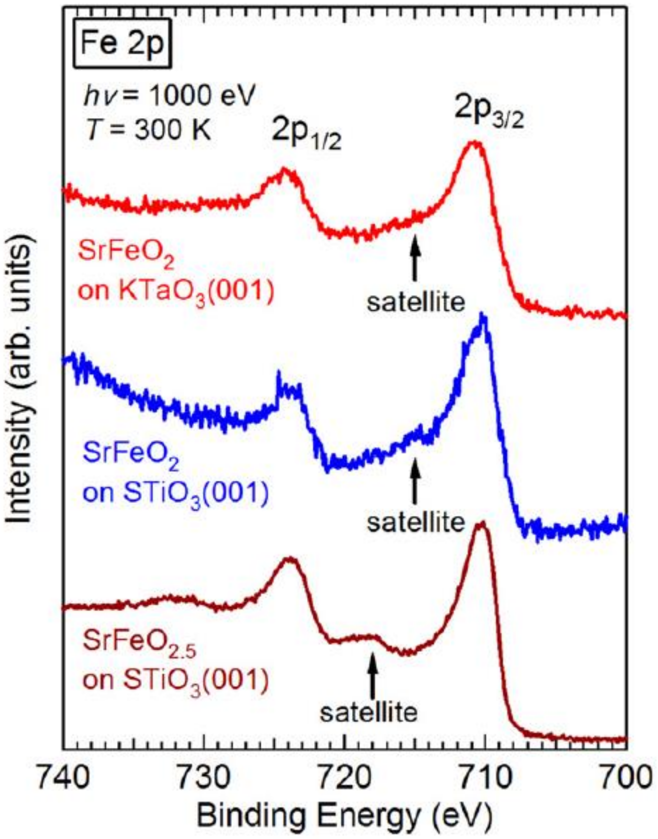

Figure 5-6. Fe 2*p* core-level spectra of the $SrFeO_2$ thin films prepared at 250 °C on $KTaO_3(001)$ and at 280 °C on $SrTiO_3(001)$, as well as the spectrum of the precursor $SrFeO_{2.5}$ thin film on $SrTiO_3(001)$.

Origin of metallic conductivity

It is possible that the observed metallic conduction of the $SrFeO_2$/KTO arose only at the interface between the film and the substrate, as has been frequently argued in studies concerning the interfaces between STO and other oxides [142]. It is, furthermore, likely that potassium exists as an *n*-type interstitial dopant in the $SrFeO_2$ film on KTO. To examine these possibilities, I compared the resistivity values of $SrFeO_2$ films as a function of thickness. The inset of Fig. 5-3(b) shows the ρ–T curves of 70- and 150-nm-thick $SrFeO_2$/KTO prepared at 250 °C. The two curves can be seen to coincide almost completely. In addition, carrier density and Hall mobility as a function of temperature were approximately the same for the 70-nm- and 150-nm-thick $SrFeO_2$/KTO films, while I could not detect any potassium atoms in the $SrFeO_2$ films by XPS or dynamic SIMS. In summary, these results prove that metallic conduction is an intrinsic property of the $SrFeO_2$ films.

The application of compressive pressure could enhance electron transfer relative to Coulomb repulsion and thus drive the I-M transition in $SrFeO_2$ [136]. Here, I discuss the possibility of a chemical pressure effect from the substrate, which could cause the I-M transition in our $SrFeO_2$ films. It is known that bulk $SrFeO_2$ undergoes an I-M transition at an external hydrostatic pressure of 34 GPa [136]. Furthermore, the lattice constants for bulk $SrFeO_2$, under pressures of 0, 22, and 40 GPa were reported to be $a = 0.3991$ nm and $c = 0.3475$ nm (0 GPa), $a = 0.386$ nm and $c = 0.318$ nm (22 GPa), and $a = 0.376$ nm and $c = 0.302$ nm (40 GPa) [136]. In comparison, metallic $SrFeO_2$/KTO prepared at 250 °C shows lattice constants of $a = 0.398$ nm, $c = 0.3483$ nm, which are very close to those of bulk $SrFeO_2$ without application of pressure (0 GPa). Therefore, I can reasonably exclude the chemical pressure effect as the origin of the observed metallic conduction.

One possible explanation for the metallic conduction is that oxygen vacancies in the $SrFeO_2$ thin films generated during CaH_2 treatment release *n*-type carriers. Although there must exist oxygen vacancies in all the $SrFeO_2$ thin films examined here, the $SrFeO_2$/KTO with the highest crystallinity only showed the metallic behavior, probably because in the lower crystallinity film the charge carriers undergo substantial scattering from local lattice dislocations. Another scenario assumes that hydrogen incorporated into the film are ionized to provide carriers. Although neutron powder diffraction measurements have revealed that bulk $SrFeO_2$ does not contain hydrogen ions [58], hydrogen diffusion in $SrFeO_2$ would be more significant when present in the form of a thin film. Figure 5-7 shows the dynamic SIMS depth profiles of H secondary ions in the $SrFeO_2$/KTO reduced at 250 °C and the precursor $SrFeO_{3-\delta}$/KTO. Notably, the hydrogen density in the film after CaH_2 reduction is one order of magnitude higher than that of the precursor film, although the values for the H ion density determined by using H-$SrTiO_3$ standards have some uncertainty due to chemical matrix effects, indicating that a large amount of hydrogen diffuses from the surface into the entire $SrFeO_2$ film during CaH_2

reduction process. Recently, it was reported that large quantities of hydride ions (H^-) can be incorporated into bulk $LaSrCoOH_{0.7}$, $Sr_3Co_2O_{4.33}H_{0.84}$, $BaTiO_{2.4}H_{0.6}$, and $ATiO_{3-x}H_x$ (A = Ba, Sr, Ca) epitaxial thin films by metal hydride treatment [9,14,15,17]. Among them, $ATiO_3$ (A = Ba, Sr, Ca) showed metallic behavior in the bulk and in thin films [15,17]. Thus, it seems natural to speculate that a similar H^- substitution reaction occurs in $SrFeO_2$ as well. Alternatively, it is possible that hydrogen is present as interstitial H^+ in the $SrFeO_2$ films. Indeed, substituted H^- and interstitial H^+ have been proposed to act as an *n*-type carrier in various oxide semiconductors [17,143]. Further spectroscopic investigations are needed to determine the chemical form of hydrogen in the $SrFeO_2$ films.

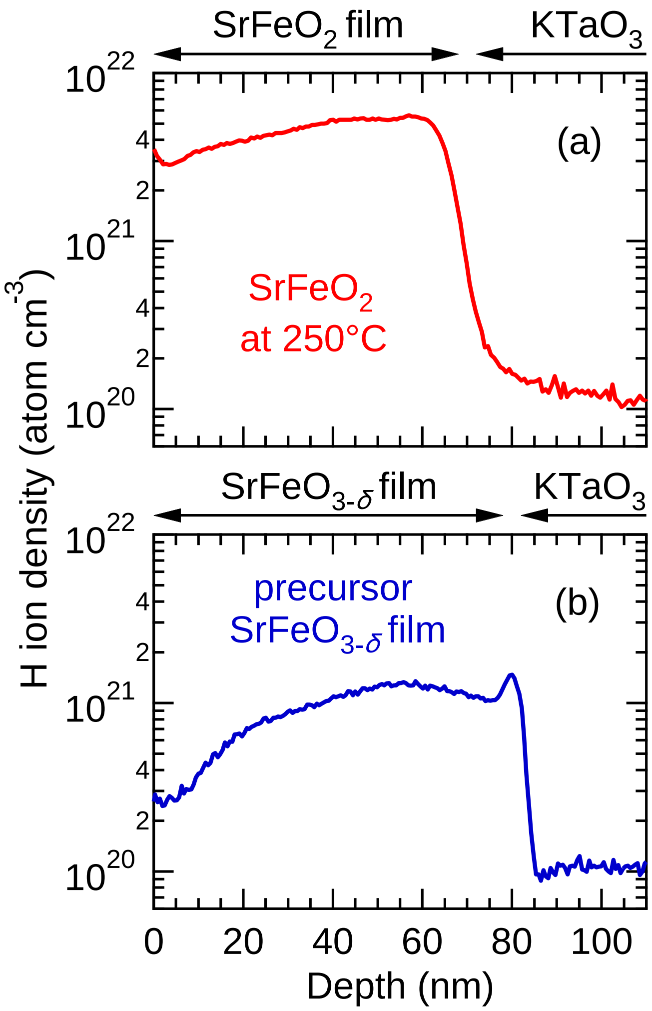

Figure 5-7. Dynamic secondary ion mass spectrometry depth profiles of H secondary ions in (a) the $SrFeO_{2.5}$ thin film prepared at 250 °C on $KTaO_3(001)$ and (b) the precursor $SrFeO_{3-\delta}$ thin film.

5.3.3 Sm substitution effect on $SrFeO_2$

Brief introduction

As mentioned above, the high-crystalline $SrFeO_2$ epitaxial thin film grown on lattice-matched KTO substrate exhibits metallic behavior with relatively high electron mobility of 10.2 $cm^2V^{-1}s^{-1}$ at 300 K. The electron carriers are supplied from oxygen vacancies or hydrogen ions in the film, while the carrier density in the film of 3.1×10^{18} cm^{-3} at 300 K is considerably small. Additionally, it was found that the conductivity of $SrFeO_2$ film is strongly dependent on its crystallinity. Thus, improvement of crystallinity is crucial in order to enhance the conductivity, although it is difficult due to low synthesis temperature. One promising way to improve crystallinity is to substitute a small amount of R^{3+} (R is rare-earth element) for Sr^{2+}, because it would prevent rapid structural change and/or over reduction caused by the synthesis reaction using CaH_2. Furthermore, the substitution would supply electron carriers. Thus, I attempted to improve the conductivity of $SrFeO_2$ film by Sm substitution.

Structural properties of the Sm-substituted $SrFeO_2$ thin films

Figure 5-8 shows the 2θ–θ XRD patterns for the precursor and CaH_2-treated $Sr_{0.95}Sm_{0.05}FeO_{2.5}$ films on KTO substrates. The precursor film exhibited 002 and $00\underline{5/2}$ diffraction peaks, indicating that the precursor film had c-axis oriented brownmillerite structure. After CaH_2-treatment at 280 °C, new 002 diffraction from infinite-layer structure appeared, while the peaks from the precursor disappeared. This proves that the CaH_2-treated $Sr_{0.95}Sm_{0.05}FeO_{2.5}$ film had c-axis oriented infinite-layer structure with the c-axis length of 3.485 Å. The other CaH_2-treated $Sr_{1-x}Sm_xFeO_{2.5}$ ($x = 0.01$, 0.03, and 0.1) films also had the same infinite-layer structure. These CaH_2-treated films are hereafter referred to as $Sr_{1-x}Sm_xFeO_2$ films.

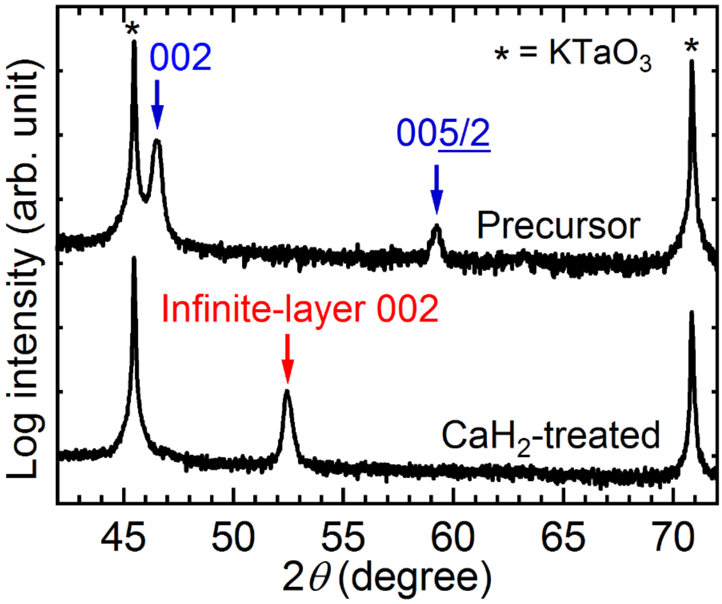

Figure 5-8. 2θ–θ X-ray diffraction patterns of the precursor $Sr_{0.95}Sm_{0.05}FeO_{2.5}$ film and the film reacted with CaH_2 at 280 °C for 24 h on $KTaO_3$(001) substrates.

Fe and Sm oxidation states of the Sm-substituted $SrFeO_2$ thin films

In order to estimate the valences of the Fe and Sm ions in the film, XPS and XAS measurements were performed. Figure 5-9(a) shows the Fe 2*p* core-level XPS spectra of the $Sr_{0.95}Sm_{0.05}FeO_2$ film on KTO prepared at 280 °C. The spectrum is characterized by a Fe $2p_{1/2}$–Fe $2p_{3/2}$ doublet and a weak satellite located at a binding energy of ~715 eV between the doublet peaks. It is known that the position of the Fe 2*p* satellite is very sensitive to the oxidation state of Fe. By comparing Fig. 5-9(a) with the Fe 2*p* core-level XPS spectra of $SrFeO_2$ and $SrFeO_{2.5}$ films (Fig. 5-6), I determined the valence of the Fe ions in the film to be mostly divalent. Figure 5-9(b) shows the XAS spectrum near the Sm M-edge observed in the $Sr_{0.95}Sm_{0.05}FeO_2$ film. The spectrum has a small peak at photon energy of ~1075 eV, a main peak at ~1080 eV, and a high-energy shoulder at ~1082 eV in the Sm M_5-edge. The spectrum is similar to the XAS spectra of Sm_2O_3 reported previously [144], indicating that trivalent Sm ions are dominant in the film. Considering charge neutrality, it is suggested that excess oxygen and/or hydride ions are incorporated into the film. Indeed, the $Sr_{0.95}Sm_{0.05}FeO_2$ film prepared at 280 °C contained a large amount of hydrogen ions, 5×10^{21} cm^{-3}, as seen from the dynamic SIMS results (Fig. 5-10), similar to the $SrFeO_2$ films. The fact that the *c*-axis length does not show remarkable change by Sm substitution in spite of smaller ionic radius of Sm^{3+} (1.08 Å) than Sr^{2+} (1.26 Å) [131] might be explained by the incorporation of excess oxygen and/or hydride ions.

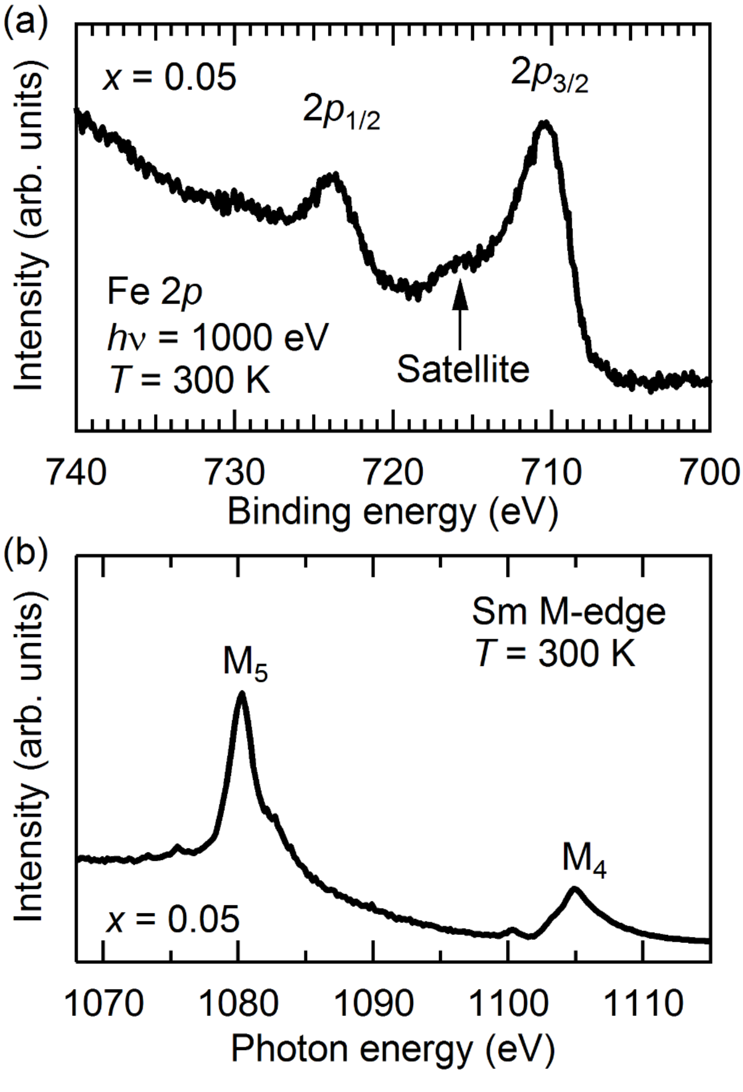

Figure 5-9. (a) Fe 2*p* core-level photoemission and (b) X-ray absorption spectra near the Sm M-edge in the $Sr_{0.95}Sm_{0.05}FeO_{2.5}$ film on $KTaO_3$(001) substrate prepared at 280 °C.

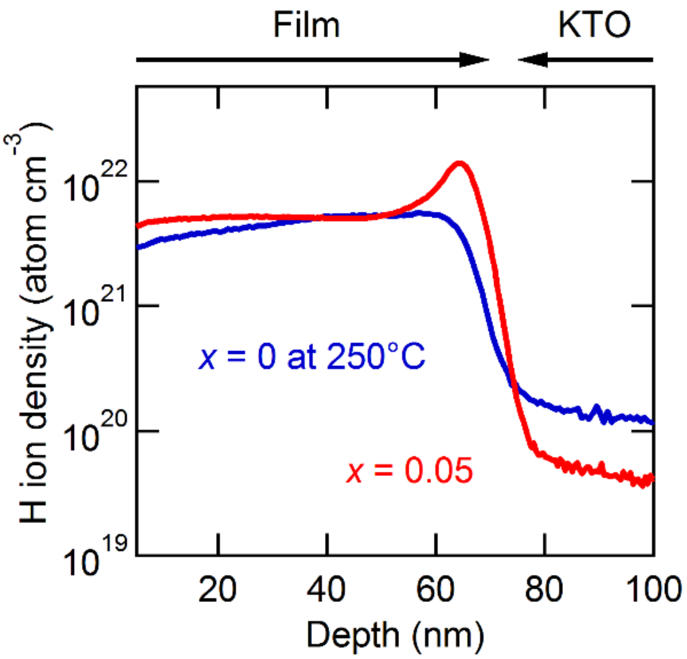

Figure 5-10. Dynamic secondary ion mass spectrometry depth profile of H content for the $Sr_{0.95}Sm_{0.05}FeO_2$ film prepared at 280 °C and $SrFeO_2$ film prepared at 250 °C on $KTaO_3(001)$ substrates.

Transport properties of the Sm-substituted $SrFeO_2$ thin films

Figure 5-11 shows the resistivity versus temperature (ρ–T) curves for the $Sr_{1-x}Sm_xFeO_2$ (x = 0, 0.01, 0.03, 0.05, and 0.1) prepared at 280 °C and the $SrFeO_2$ films on KTO substrates prepared at 250 °C. The $Sr_{1-x}Sm_xFeO_2$ (x = 0 and 0.01) films exhibit an insulator-metal transition at 58 K and 44 K, respectively. On the other hand, the $Sr_{1-x}Sm_xFeO_2$ (x = 0.03, 0.05, and 0.01) and the $SrFeO_2$ films are metallic ($d\rho/dT > 0$) over the whole temperature range below 300 K. Compared among the $Sr_{1-x}Sm_xFeO_2$ films prepared at 280 °C, the ρ(2 K) value decreased with increasing x up to 0.05. Thus, the electrical conductivity of $SrFeO_2$ thin film can be increased by Sm substitution. The $Sr_{0.95}Sm_{0.05}FeO_2$ film had the lowest ρ(2 K) value of 2.8×10^{-3} Ω cm, which is approximately five times lower than that of the $SrFeO_2$ film, 1.4×10^{-2} Ω cm.

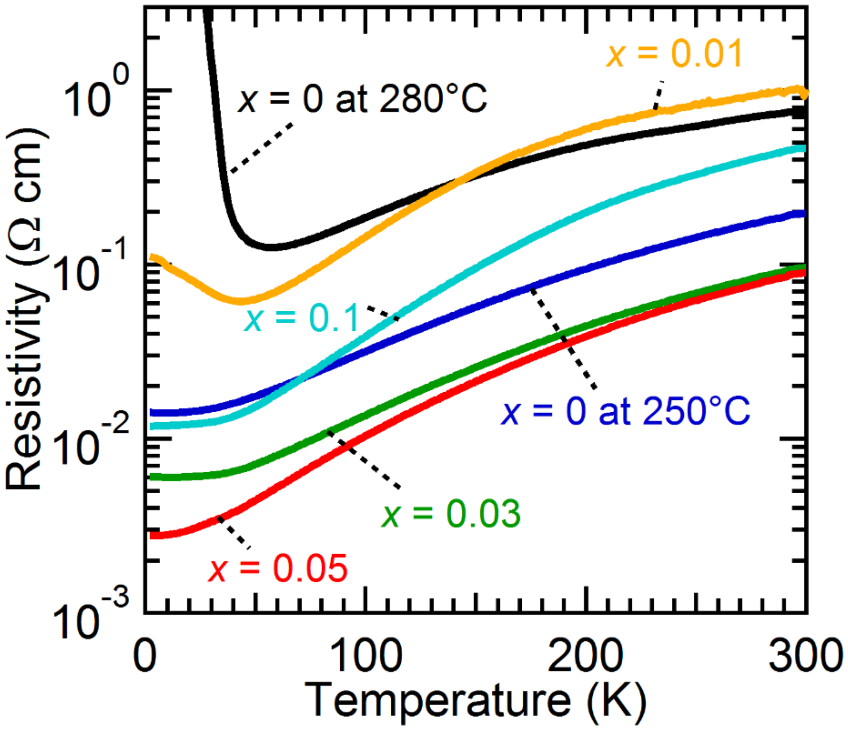

Figure 5-11. Resistivity versus temperature curves for the 280 °C CaH_2-treated $Sr_{1-x}Sm_xFeO_{2.5}$ (x = 0, 0.01, 0.03, 0.05, and 0.1) and the 250 °C CaH_2-treated $SrFeO_{2.5}$ films on $KTaO_3$(001) substrates.

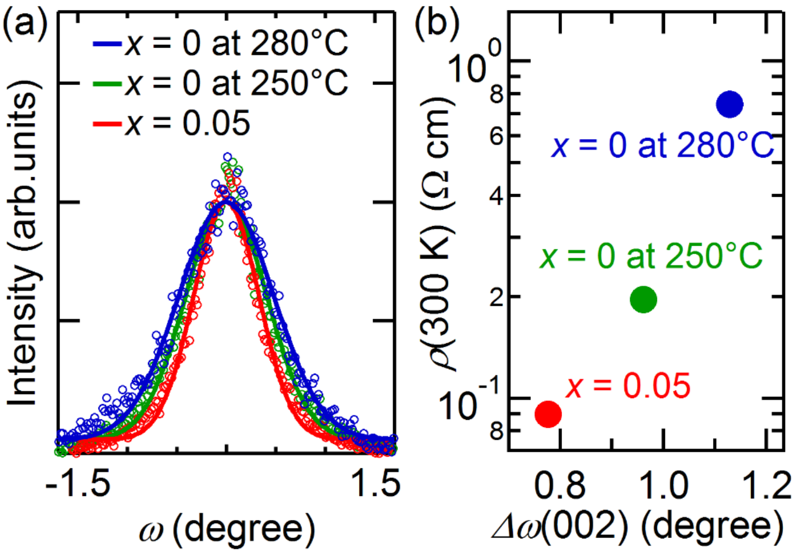

Figure 5-12. (a) Rocking curves of the 002 diffraction and (b) resistivity at 300 K (ρ(300 K)) as a function of the full-width-half-maximum values of the rocking curves (i.e., $\Delta\omega$(002)) for the 280 °C CaH_2-treated $Sr_{0.95}Sm_{0.05}FeO_{2.5}$ film and 250 °C and 280 °C CaH_2-treated $SrFeO_{2.5}$ films on $KTaO_3$(001) substrates.

The conduction carriers were evaluated by Hall measurements. In the $Sr_{0.95}Sm_{0.05}FeO_2$ film, the Hall coefficient showed negative value, indicating that electrons serve as carriers. At 300 K, its Hall mobility reached to be 13.5 $cm^2V^{-1}s^{-1}$, which is higher than that of the $SrFeO_2$ film, 10.2 $cm^2V^{-1}s^{-1}$. On the other hand, the carrier concentration (n_e) of the $Sr_{0.95}Sm_{0.05}FeO_2$ film, 5×10^{18} cm^{-3}, is much lower than the Sm concentration ($n_{Sm} = 9\times10^{20}$ cm^{-3}) and similar to n_e of the $SrFeO_2$ film, 3×10^{18} cm^{-3}. This may be due to influence of excess oxygen and/or hydride ions incorporated in the film.

In general, carrier mobility largely depends on crystallinity because defects can trap conducting electrons [138]. In order to discuss the relation between Sm substitution and crystallinity of the film. The rocking curves of the 002 diffraction for the $Sr_{0.95}Sm_{0.05}FeO_2$ film prepared at 280 °C and the $SrFeO_2$ films on KTO substrates prepared at 250 °C and 280 °C were measured as shown in Figure 5-12(a). The $\Delta\omega(002)$ values were evaluated to be 0.78°, 0.96°, and 1.13°, respectively, meaning that a small amount of Sm substitution was effective for improving the crystallinity of the film. Figure 5-12(b) shows ρ(300 K) as function of $\Delta\omega(002)$ for the films. The ρ value systematically decreased with increasing crystallinity, suggesting that the conductivity enhancement with Sm substitution is mainly caused by the improved crystallinity.

To verify whether Sm substitution improves conductivity even on other substrates, I fabricated $Sr_{1-x}Sm_xFeO_2$ films on DSO substrates. Figure 5-13(a) shows the ρ–T curves for $Sr_{1-x}Sm_xFeO_2$ (x = 0, 0.01, and 0.05) films on DSO heat-treated at 280 °C. As is seen in the figure, the ρ(300 K) value rapidly decreased with x up to 0.05. The $Sr_{0.95}Sm_{0.05}FeO_2$ film on DSO exhibited metallic-like behavior with ρ(300 K) of 10^{-1} Ωcm, though $SrFeO_2$ film on DSO prepared at the same temperature was insulating with ρ(300 K) of 10^3 Ωcm. As shown in Fig. 5-13(b), the metallic $Sr_{0.95}Sm_{0.05}FeO_2$ film on DSO shows higher crystallinity than that of the insulating $SrFeO_2$ films. Thus, it can concluded that Sm substitution improved the crystallinity and thus conductivity even on DSO substrate.

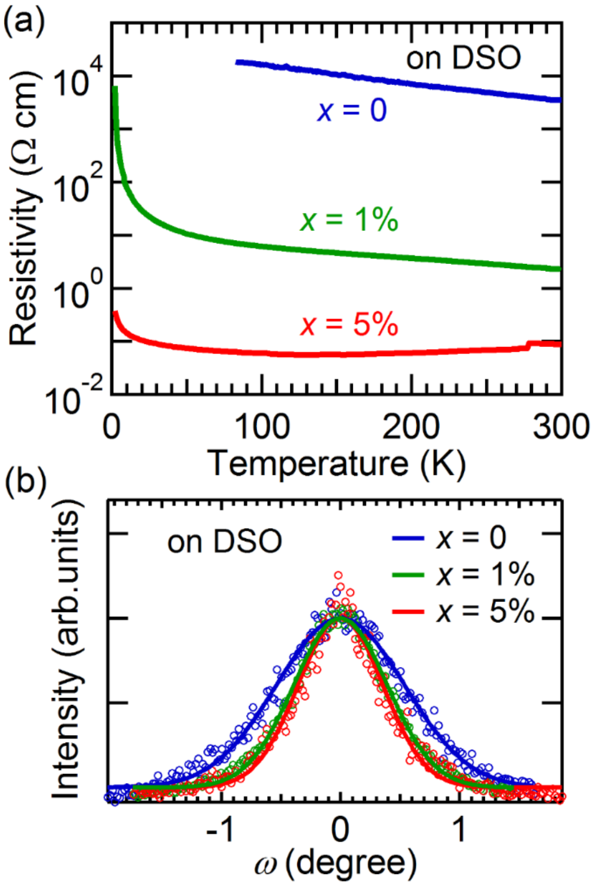

Figure 5-13. (a) Resistivity versus temperature curves and (b) rocking curves of the 002 diffraction for the 280 °C CaH_2-treated $Sr_{1-x}Sm_xFeO_{2.5}$ (x = 0, 0.01, and 0.05) films on $DyScO_3(110)$ substrates.

5.4 Conclusion

I investigated the structural properties and transport behavior of infinite-layer $SrFeO_2$ thin films grown on STO, DSO, and KTO substrates by PLD via solid-phase CaH_2 reduction of $SrFeO_{3-\delta}$ precursor films. As a consequence, I found that highly crystalline $SrFeO_2$ films prepared on lattice-matched KTO substrate exhibited metallic transport behavior, while those prepared on $SrTiO_3(001)$ and $DyScO_3(110)$ substrates were insulating films, in analogy to bulk $SrFeO_2$. Hall measurements of the metallic $SrFeO_2$/KTO confirmed that the conduction carriers were n-type (i.e., electrons) with a carrier density of 3.1×10^{18} cm^{-3} and a mobility of 10.2 cm^2 V^{-1} s^{-1} at 300 K. I speculate that the electron carriers are supplied by oxygen vacancies or hydrogen ions such as H^- that substitutes for vacant oxygen sites or H^+ that resides in the Sr layer between FeO_2 sheets. It was furthermore revealed that metallic conductivity can only be obtained in highly crystalline samples with $\Delta\omega(002) < 1°$. In addition, I also found that the conductivity of $SrFeO_2$ film could be enhanced by Sm substitution. This conductivity enhancement mainly originated from the improved crystallinity associated with Sm substitution. The Sm substituted $SrFeO_2$ films on KTO substrates exhibited relatively high Hall mobility of 13.5 $cm^2V^{-1}s^{-1}$ at 300 K, and the films on DSO substrates underwent an insulator-metal transition.

Chapter 6 Oxidation and reduction: *A*-site ordered perovskite $YBaCo_2O_x$ films

6.1 Introduction

A-site cation-ordered perovskite cobaltites, $RBaCo_2O_x$ (R = rare earth element), have attracted substantial attention because of their intriguing features, such as very high magnetoresistance, spin-crossover, and high electronic and ionic conductivity [145-149]. These cobaltite properties can be controlled over wide ranges by varying the ionic size of *R*, cell parameters, and especially the oxygen content (x), although the oxygen content range allowable in conventional high-temperature syntheses is limited [145,150-152]. Recently, low-temperature synthetic routes using topotactic reactions have been developed to expand the oxygen range [66,153,154]. For example, $YBaCo_2O_{4.5}$ was obtained by reacting $YBaCo_2O_5$ with NaH, a reducing agent, at 210 °C [66], although the conventional solid-state synthesis could produce $YBaCo_2O_x$ with $5.0 \leq x \leq 5.52$ [152]. The highly reductive atmosphere in the topotactic reaction resulted in the formation of oxygen vacancies in the [CoO_x] layers of $YBaCo_2O_x$ [66] and in the [YO_x] layers [152-155], as illustrated in Fig. 6-1. Because of the large variability in the oxygen contents, $YBaCo_2O_x$ has a rich electronic phase diagram containing antiferromagnetic ordering [66], charge order [156], and a temperature-induced metal-insulator transition (MIT) [152] at x = 4.5, 5.0, and 5.5, respectively.

Compared with bulk polycrystalline $YBaCo_2O_x$ ($4.5 \leq x \leq 5.52$), which has been intensively studied previously, the preparation of $YBaCo_2O_x$ thin films has not yet been reported. Epitaxial thin-film growth technology combined with the topotactic reduction and oxidation reactions should produce $YBaCo_2O_x$ in single-crystalline form, allowing us

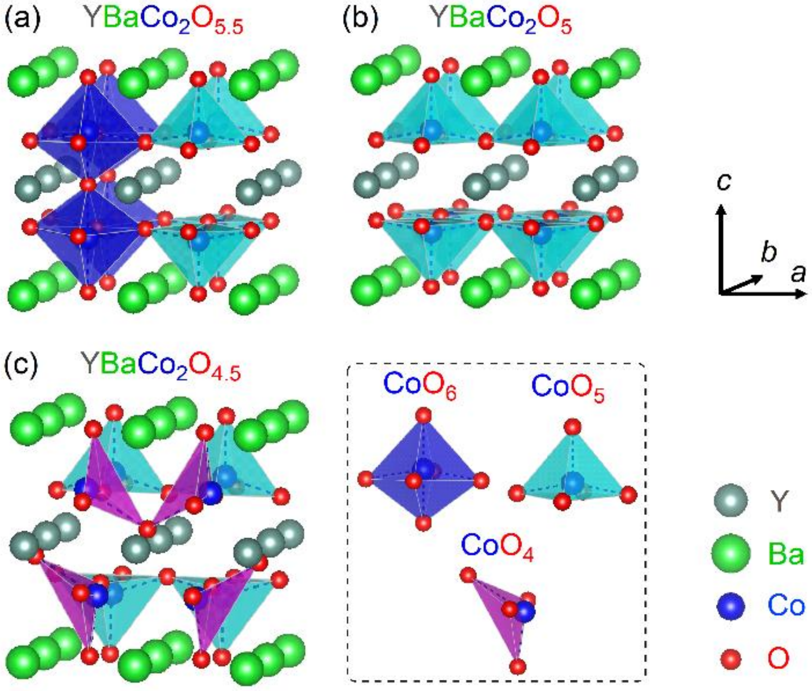

Figure 6-1. Crystal structures of (a) $YBaCo_2O_{5.5}$, (b) $YBaCo_2O_5$, and (c) $YBaCo_2O_{4.5}$. CoO_6, CoO_5, and CoO_4 units in $YBaCo_2O_x$ are shown in a box made of a dotted line.

to measure the intrinsic properties. Furthermore, high reactivity of the films would expand the oxygen content range. Therefore, I attempted to fabricate $YBaCo_2O_x$ epitaxial thin films by combining PLD and topotactic reduction and oxidation methods. As a result, the oxygen content (x) could be controlled in a range of 4.5–6, which was wider than the previous reports, 4.5−5.5, manifesting the strong oxidizing power of NaClO and high reactivity of the films. The c-axis lengths of the $YBaCo_2O_x$ films decreased with decreasing x when $x \geq 5.3$ but drastically increased when $x \sim 4.5$. The new phase, $YBaCo_2O_6$, exhibited ferromagnetic metallic behavior with T_C of 130 K, while the $YBaCo_2O_{5.5}$ film is an antiferromagnetic insulator. Furthermore, the $YBaCo_2O_6$ film shows crystal magnetic anisotropy and magnetoresistance.

6.2 Method

Synthesis method

A-site cation-ordered perovskite $YBaCo_2O_x$ films were grown on STO(001) substrates by PLD. I used a $YBaCo_2O_x$ (x ~ 5.5) ceramic pellet prepared from mixed powders of Y_2O_3, $BaCO_3$, and Co_3O_4 by a solid-state reaction (pre-sintering at 950 °C for 12 h and sintering at 1100 °C for 24 h with a cooling rate of 1 °C/min for several times) as a PLD target. The target was ablated by a KrF excimer laser operated at ~2 $J{\cdot}cm^{-2}{\cdot}shot^{-1}$ with a 10-Hz repetition rate. The substrate temperature and oxygen partial pressure were maintained at 900−950 °C and 200 mTorr, respectively, during the PLD deposition. The typical film thicknesses were measured to be 60–80 nm using a stylus surface profiler.

The obtained precursor films were further subjected to topotactic reduction using CaH_2 at a reaction temperature (T_r) of 100−400 °C for 24 h in an evacuated Pyrex tube. On the other hand, topotactic oxidation was conducted by reacting the $YBaCo_2O_x$ precursor films with NaClO aqueous solution (effective Cl concentration of 1 %) at 60−80 °C for 20−40 h.

Characterization method

Crystal structures were characterized by XRD using Cu-$K\alpha$ radiation. Chemical compositions were evaluated using EDS with an electron-accelerating voltage of 2.5 keV, which is sufficiently low to minimize substrate contributions. The oxygen amounts of the films were roughly calculated from the EDS peak area ratios of the O $K\alpha$/Co $L\alpha$ peaks by simulating the electron trajectory using the Monte Carlo method [88]. I also performed ERDA measurements by using Cl ion beam with 38.4 MeV to evaluate the oxygen contents of the films. XPS and XAS measurements were conducted at the BL-2A beamline of Photon Factory, KEK. The XPS spectra were recorded using a VG-SCIENTA SES-2002 electron-energy analyzer at a photon energy of 1,000 eV. The XAS spectra were measured with the total electron-yield method. The Fermi levels of the samples were referred to that of Au foil in electrical contact with the samples. In-plane resistivity (ρ) was measured by using four- and two-probe methods with Au electrodes. Magnetization versus temperature (*M*-*T*) measurements under field-cooling (FC) and zero-field-cooling (ZFC) conditions and *M*-*H* measurements were conducted by using a superconducting quantum interference device (SQUID) magnetometer.

6.3 Results and discussion

6.3.1 Synthesis of $YBaCo_2O_x$ films ($x \leq 5.5$)

Figure 6-2(a) shows a 2θ–θ X-ray diffraction (XRD) pattern of the as-grown $YBaCo_2O_x$ film. The 001, 002, 003, 004, and 006 diffraction peaks were clearly observed, indicating that the film has a *c*-axis-oriented *A*-site ordered perovskite structure. Figure 6-2(b) depicts the EDS spectrum of the film for the O $K\alpha$ and Co $L\alpha$ peaks. The EDS peak area ratio of the O $K\alpha$/Co $L\alpha$ peaks (S_O/S_{Co}) was calculated to be about 2.03. To evaluate the x value, the relation $x = 2 \times a \times (S_O/S_{Co})$ was used, where the relative sensitivity factor (a) was estimated as 1.368 based on a Monte Carlo simulation of electron trajectory in solids [88]. The oxygen amount (x) of the as-grown $YBaCo_2O_x$ film was roughly estimated to be $x \sim 5.6 \pm 0.3$. Thus, the as-grown film on the STO substrate can be regarded to consist of layer stacking of $[YO_{0.5}]$–$[CoO_2]$–$[BaO]$–$[CoO_2]$, as illustrated in Fig. 6-1(a). The film is hereafter referred to as $YBaCo_2O_{5.5}$. Figure 6-2(c) shows the XRD reciprocal space map (RSM) for the 206 diffraction of the $YBaCo_2O_{5.5}$ film. The q_x value of the film's 206 peak is identical to that of STO 103, demonstrating that the $YBaCo_2O_{5.5}$ film was grown coherently on the STO substrate. The film had a pseudo-tetragonal lattice with $a/2 = b = 3.905$ and $c = 7.485$ Å, while bulk $YBaCo_2O_{5.5}$ is reported to have an orthorhombic lattice with $a/2 = 3.923$, $b = 3.819$ and $c = 7.516$ Å [152]. Notably, the film has a smaller out-of-plane (*c*-axis) length and a larger in-plane unit cell area ($S = a/2 \times b = 15.25$ Å^2) than bulk $YBaCo_2O_{5.5}$ ($S = 14.98$ Å^2); i.e., the film experiences tensile-like

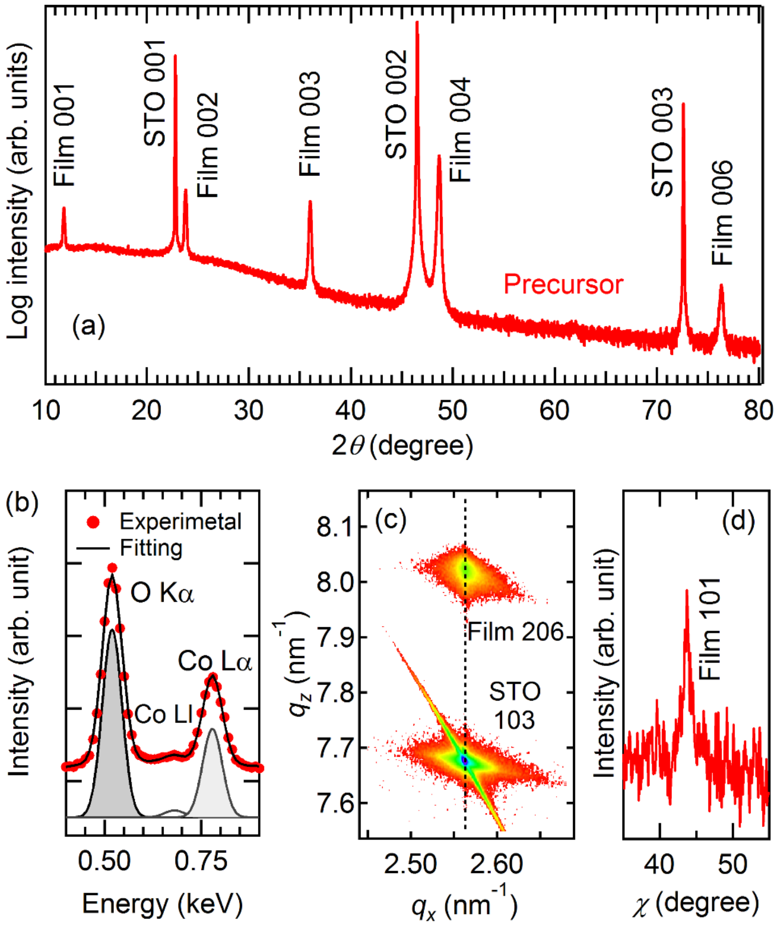

Figure 6-2. (a) 2θ–θ X-ray diffraction pattern, (b) energy dispersive X-ray spectroscopy spectrum and the O *K*α, Co *L*l, and Co *L*α components obtained by least square fitting, (c) reciprocal space map around the $SrTiO_3$ 103 diffraction peak, and (d) X-ray diffraction pattern measured at 2θ = 16.8° around χ = 44° for the $YBaCo_2O_{5.5}$ film.

strain from the substrate.

Figure 6-2(d) shows the XRD data at 2θ = 16.8° at approximately χ = 44° for the as-grown $YBaCo_2O_{5.5}$ film. The 101 diffraction peak was clearly observed, which corresponds to the in-plane superstructure peak. In bulk $YBaCo_2O_x$, the 101 diffraction peak appears when $5.45 \leq x \leq 5.52$ because the oxygen vacancies are ordered along the *a*-axis in the [$YO_{0.5}$] layer, as illustrated in Fig. 6-1(a) [152]. Therefore, it is suggested that the $YBaCo_2O_{5.5}$ film contains oxygen vacancies that are ordered along the in-plane axis, similar to bulk $YBaCo_2O_{5.5}$, and that the x value is approximately 5.5, which agrees well with the EDS result suggesting that the x value from the EDS measurement is convincible.

After the reaction with CaH_2 at T_r = 200 °C, the XRD peaks shifted toward lower diffraction angles without forming any impurity phases (Fig. 6-3(a)). In addition, the EDS measurements revealed that the x value decreased to ~4.5 ± 0.3 after the CaH_2-treatment (Fig. 6-3(b)). These results indicate that a large quantity of oxygen vacancies are introduced into the film without changing the cation framework during the reaction. Figure 6-3(c) shows the RSM for the CaH_2-treated film. The 106 peak of the film is much broader than that of $YBaCo_2O_{5.5}$, and it splits into three components along q_x, as shown in the inset of Fig. 6-3(c). The q_x value of the main component is equivalent to that of the

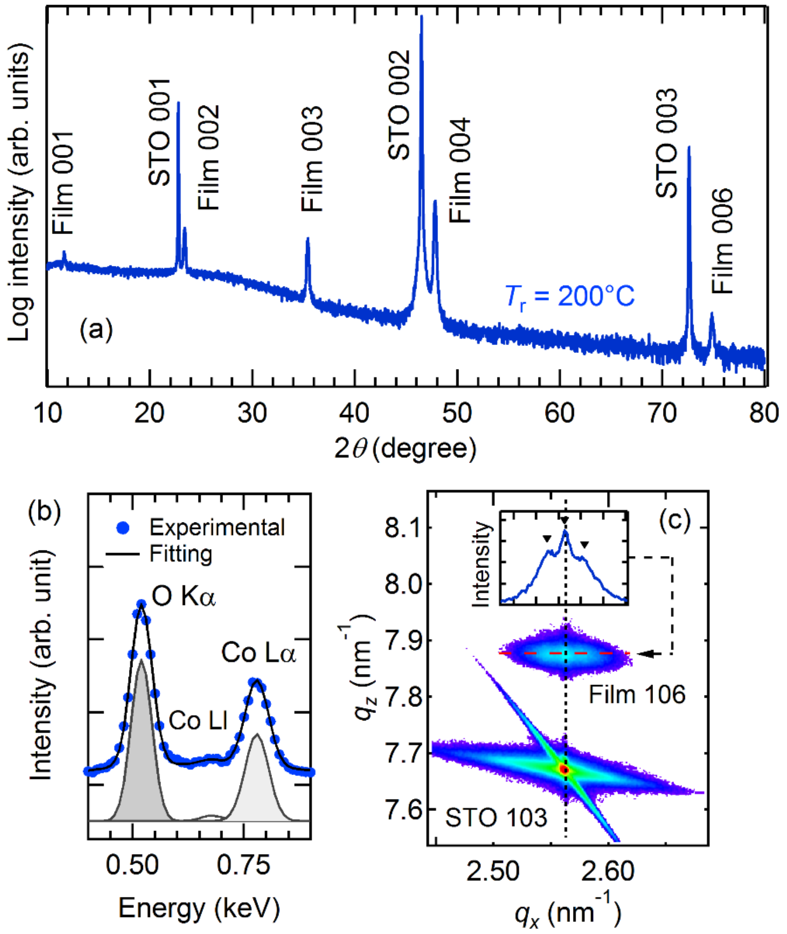

Figure 6-3. (a) 2*θ*–*θ* X-ray diffraction pattern, (b) energy dispersive X-ray spectroscopy spectrum_and the O *K*α, Co *L*l, and Co *L*α components obtained by least square fitting, and (c) reciprocal space map around the $SrTiO_3$ 103 diffraction peak for the CaH_2-treated $YBaCo_2O_x$ films at T_r = 200 °C. The inset shows a cross section along the dotted line across the 106 peak of the film.

STO 103 peak, implying that coherent and relaxed regions coexist in the film prepared at T_r = 200 °C. The former has a pseudo-tetragonal lattice with $a = b = 3.905$ and $c = 7.608$ Å, while the latter can be described by an orthorhombic lattice with $a = 3.93$, $b = 3.88$, and $c = 7.608$ Å. Notably, the in-plane lattice constants of the coherent and relaxed regions in the film were very similar to those of STO ($a = b = 3.905$ Å), whereas the deviation from bulk $YBaCo_2O_{4.5}$ (monoclinic lattice with $a/2 = 4.1334$, $b = 3.6818$ and $c = 8.6474$ Å and $\beta = 118.51°$) [66] is as large as 5 %. This suggests that the in-plane lattice constants remain under the influence of the epitaxial strain during the topotactic reaction. The c-axis length of the film was slightly larger than the $c \cdot \sin\beta$ value (7.599 Å) of bulk $YBaCo_2O_{4.5}$.

Figure 6-4(a) shows the x values of the $YBaCo_2O_x$ films prepared at various T_r. As can be seen, x decreased with increasing T_r, indicating that CaH_2 was an effective reducing reagent. The x value was in the range of 5.3–5.5 below T_r = 125 °C, while it was

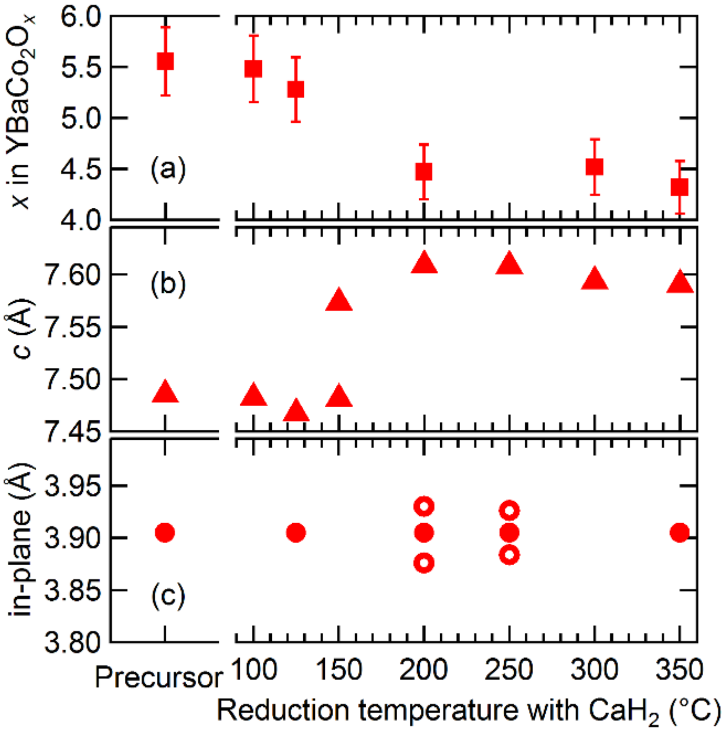

Figure 6-4. (a) Oxygen contents, (b) c-axis, and (c) in-plane lattice lengths of the $YBaCo_2O_x$ films. Filled and open circles in (c) indicate the lattice parameters corresponding to coherent and relaxed regions, respectively.

reduced down to ~4.5 at T_r = 200−350 °C. The CaH_2-treatment did not produce x ~ 5 phase, in contrast to the previously reported Ar gas-treatment [152], indicating that the strong reducing power of CaH_2 makes it difficult to control oxygen content gradually. The film became amorphous after higher temperature treatment (T_r = 400 °C). Figure 6-4(b) plots the c-axis lengths of the films as a function of T_r. The c-axis lengths of the films prepared at T_r = 100 and 125 °C are 7.482 and 7.467 Å, respectively, which are smaller than that of the $YBaCo_2O_{5.5}$ film: 7.485 Å. This result suggests that the c-axis length decreased with decreasing x when $5.3 \leq x \leq 5.5$, similar to the case of bulk $YBaCo_2O_x$ ($5.0 \leq x \leq 5.5$) [152]. In contrast, at T_r = 200−350 °C, the c-axis length significantly increased to 7.608 Å, which is similar to the $c{\cdot}\sin\beta$ (7.599 Å) value for bulk $YBaCo_2O_{4.5}$ [66]. Thus, the relationship between the c-axis length and x value of the $YBaCo_2O_x$ film was, as a whole, very similar to that of the bulk. As depicted in Fig. 6-4(c), the in-plane lattice constants of the films were essentially the same as that of STO, although the films prepared at T_r = 200−250 °C contained relaxed regions (Fig. 6-3(c)).

6.3.2 Properties of $YBaCo_2O_x$ films ($x \leq 5.5$)

Figure 6-5 shows the resistivity versus temperature (ρ–T) curves for the $YBaCo_2O_x$ (x ~ 4.5, 5.3 and 5.5) films. The figure also includes the ρ–T curve of bulk $YBaCo_2O_{5.5}$ for comparison [152]. The $YBaCo_2O_{5.5}$ film shows semiconducting behavior ($d\rho/dT < 0$) below 380 K, unlike bulk $YBaCo_2O_{5.5}$, which undergoes MIT at 297 K [152]. In the case of bulk $YBaCo_2O_{5.5}$, the large temperature dependence of the lattice parameters is thought to be an important factor driving the MIT [152,157]. Therefore, the absence of MIT in the present $YBaCo_2O_x$ film might be attributable to the epitaxial lattice strain from the STO substrate. Figure 6-5(b) plots log ρ against $T^{-1/4}$ for the $YBaCo_2O_{5.5}$ film. The linear log ρ versus $T^{-1/4}$ relationship indicates that the carrier transport can be described by the three-dimensional variable-range-hopping (3D VRH) model. In single crystal $GdBaCo_2O_x$ which has the higher out-of-plane resistivity than the in-plane resistivity, 3D VRH becomes dominant when x deviates somewhat from 5.500 such as x

= 5.450−5.480 and 5.505−5.525 [145]. This derives from the hopping motion of localized Co^{2+} or Co^{4+} states generated by the deviation from $x = 5.500$ [145]. The $YBaCo_2O_{5.5}$ film also showed the 3D VRH behavior, indicating the existence of a few localized Co^{2+} or Co^{4+} states in the film.

The ρ(300 K) value of the $YBaCo_2O_x$ film decreased from 5.1×10^{-3} to 9.8×10^{-4} Ωcm with decreasing oxygen content x from ~5.5 to ~5.3, possibly because the generated

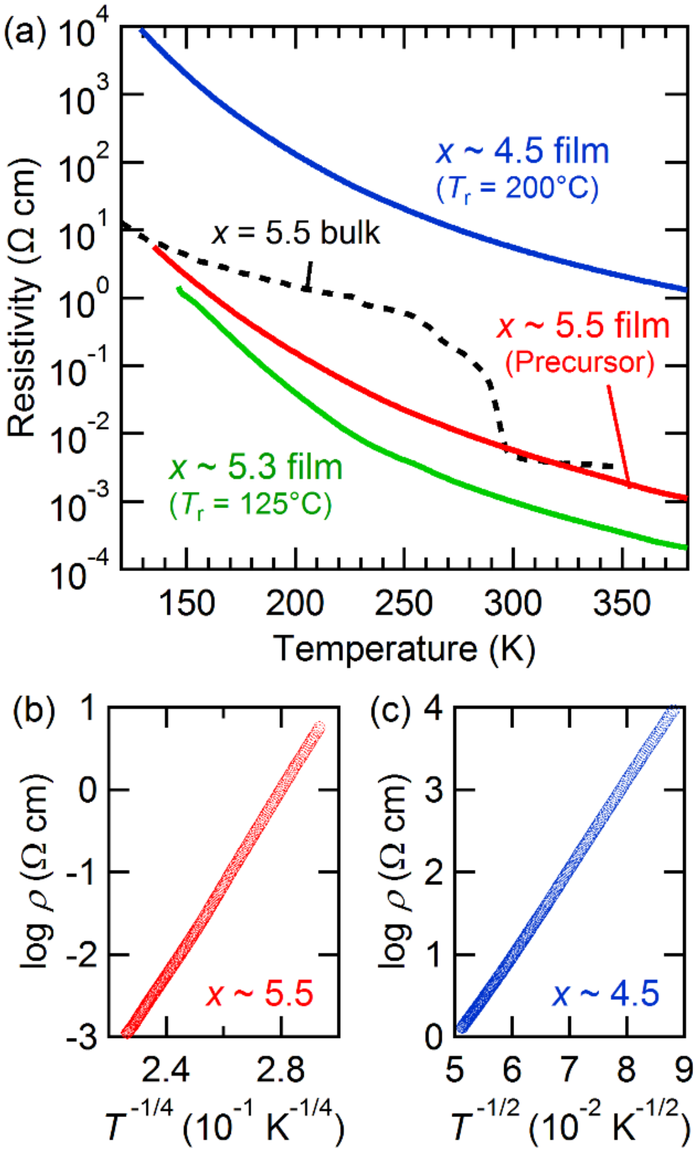

Figure 6-5. (a) ρ-T curves of the $YBaCo_2O_x$ (x ~ 4.5, 5.3, and 5.5) films and bulk $YBaCo_2O_{5.5}$. Bulk data were obtained from Akahoshi and Ueda 2001 [152]. (b) log ρ vs. $T^{-1/4}$ and (c) log ρ vs. $T^{-1/2}$ plots for the $YBaCo_2O_x$ films with x ~ 5.5 and ~ 4.5, respectively.

oxygen vacancies supply conduction electrons, as reported in bulk $GdBaCo_2O_x$ with $5.0 \leq x \leq 5.5$ [145]. In contrast, the $YBaCo_2O_{4.5}$ film shows much higher ρ, probably originating from the distortion of the CoO_x layer. The resistivity behavior of the $YBaCo_2O_{4.5}$ film could not be fitted well by the 3D VRH model, unlike the as-grown $YBaCo_2O_{5.5}$ film. As shown in Fig. 6-5(c), the ρ–T curve of the $YBaCo_2O_{4.5}$ film follows the $\rho = \rho_0\exp[(T_0/T)^{1/2}]$ relation, suggesting the Efros-Shklovskii-type hopping mechanism [145]. This type of transport behavior is usually observed when the Coulomb interaction plays a key role in carrier hopping [145].

6.3.3 Synthesis of $YBaCo_2O_x$ film ($x \approx 6$)

Figure 6-6(a) shows a 2θ–θ XRD pattern of the NaClO-treated $YBaCo_2O_x$ film prepared by reacting the precursor film with NaClO at 80 °C for 40 h. The 001, 002, 003 and 004 diffraction peaks were clearly observed, indicating that the film has *c*-axis oriented *A*-site ordered perovskite structure as illustrated in the inset of Fig. 6-6(a). Figure 6-6(b) shows the RSM image of the film. The 106 peak of the film and the 103 peak of the substrate have the identical q_x values, proving that the in-plane axis of the film was completely locked to the STO lattice even after the NaClO-treatment. In other words, the cation framework was maintained during the reaction because of the low synthesis temperature. The lattice constants of the film were $a = 3.905$ Å and $c = 7.558$ Å.

In order to investigate the oxidation states of Co ions in the film, Co *L*-edge XAS measurements were conducted on the film. Figure 6-6(c) shows the Co *L*-edge XAS spectra of the $YBaCo_2O_x$ film with those of Sr_2CoO_3Cl as a high-spin (HS) Co^{3+} reference and $SrCoO_3$ as an intermediate-spin (IS) Co^{4+} reference [158]. The Co L_3 edge of the film was located at 781.0 eV, which was between those of Sr_2CoO_3Cl and $SrCoO_3$, indicating that the Co oxidation state is a mixture of Co^{3+} and Co^{4+} in the film.

In order to evaluate the *x* value in the film, EDS and ERDA measurements were conducted. From both measurements, the *x* value of the film was roughly evaluated to be 6.0±0.3, which agrees well with the Co oxidation state measured by XAS. Hereafter, the

$YBaCo_2O_x$ film with $x \sim 6$ is referred to as $YBaCo_2O_6$. Figure 6-7 shows the *c*-axis lengths of the $YBaCo_2O_x$ films as a function of *x*, where the *x* values were estimated by using three kinds of independent techniques, EDS, ERDA and XAS. The figure also includes bulk data for comparison. The *c*-axis length of the films increased linearly with increasing *x* similar to bulk when $x > 5.0$, proving that the doped oxygen ions were successfully introduced into the perovskite lattice. The *c*-axis length of the films was shorter than that

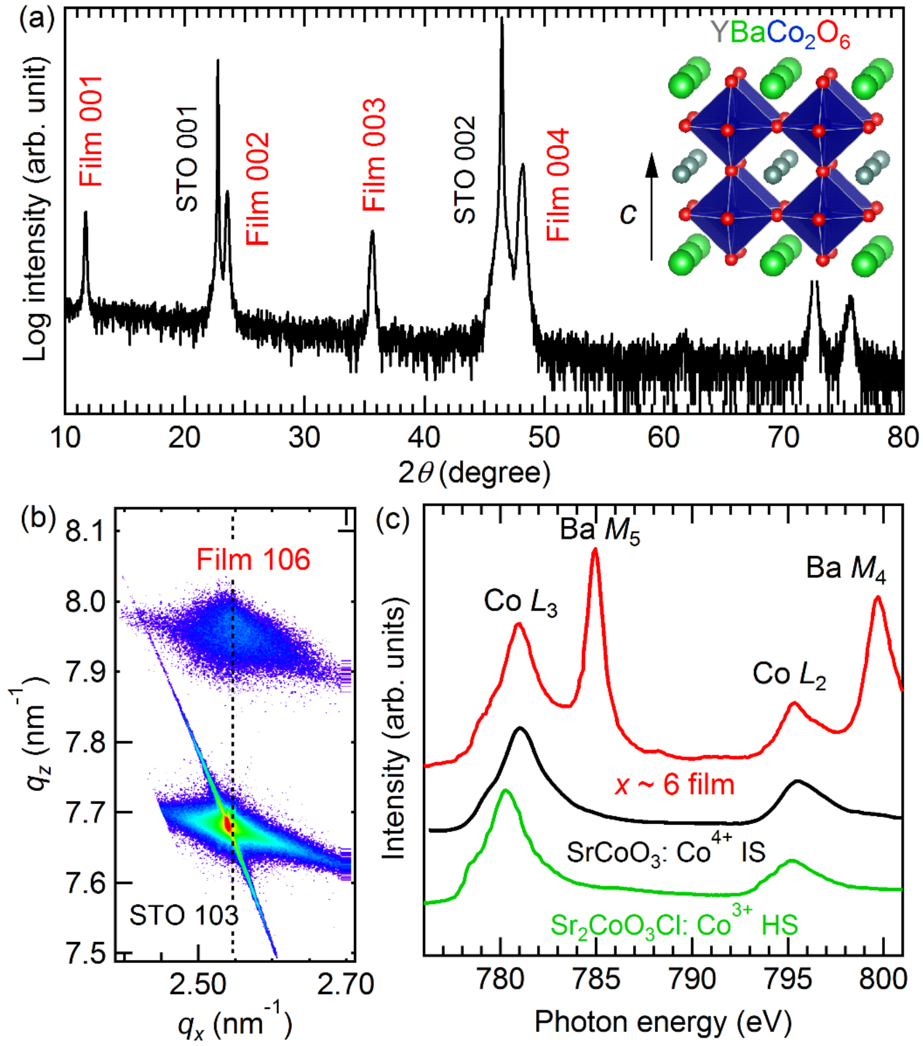

Figure 6-6. (a) 2θ–θ X-ray diffraction pattern for the $YBaCo_2O_x$ film. The inset shows a crystal structure of $YBaCo_2O_6$. (b) Reciprocal space map around the $SrTiO_3$ 103 diffraction peak for the $YBaCo_2O_x$ film. (c) Co *L*-edge XAS spectrum for the NaClO-treated $YBaCo_2O_x$ film, and the relevant spectra of $SrCoO_3$ (Co^{4+} IS state) and Sr_2CoO_3Cl (Co^{3+} HS state) [158].

of bulk because of the epitaxial strain from the substrate. The x values of the films were controlled in a range of 5.3−6 through topotactic oxidation using NaClO. Notably, the maximum x value obtained in this study, $x \sim 6$, was much higher than the previous reports, $x \leq 5.54$ [152], manifesting the strong oxidizing power of NaClO and high reactivity of the films.

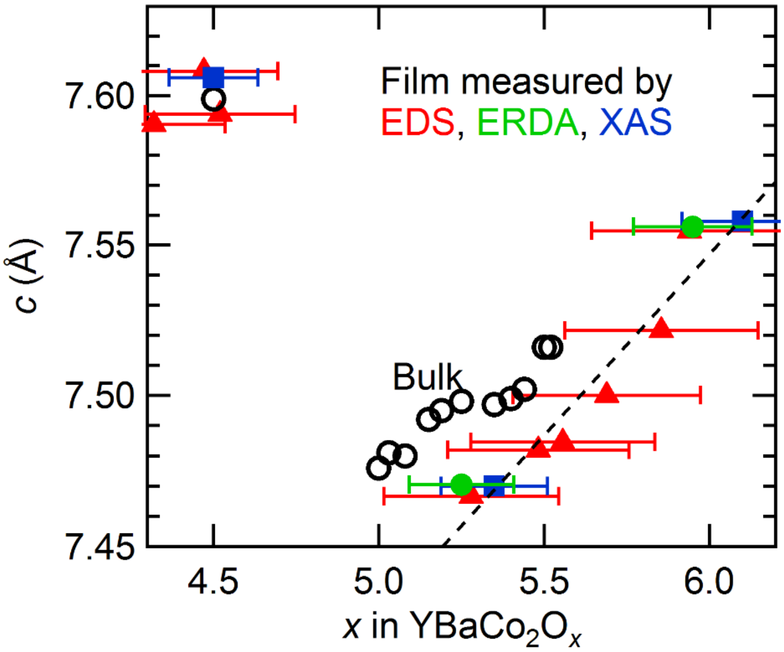

Figure 6-7. c-axis length of the $YBaCo_2O_x$ films and the bulk as a function of x. The x values were measured by EDS, ERDA, and XAS measurements. Bulk data were obtained from Ref. 152.

6.3.4 Properties of $YBaCo_2O_x$ film ($x \approx 6$)

Figure 6-8 shows magnetization versus magnetic field (M-H) curves for the $YBaCo_2O_6$ film with H along [110], [100], and [001] directions at 5 K. The $YBaCo_2O_6$ film exhibited a clear magnetic hysteresis loop, proving that the $YBaCo_2O_6$ film was ferromagnetic, while the precursor $YBaCo_2O_{5.5}$ film was an antiferromagnetic insulator. This ferromagnetic interaction in the $YBaCo_2O_6$ film might derive from the double exchange mechanism between Co^{3+} and Co^{4+}. The coercive field (H_c) and saturation

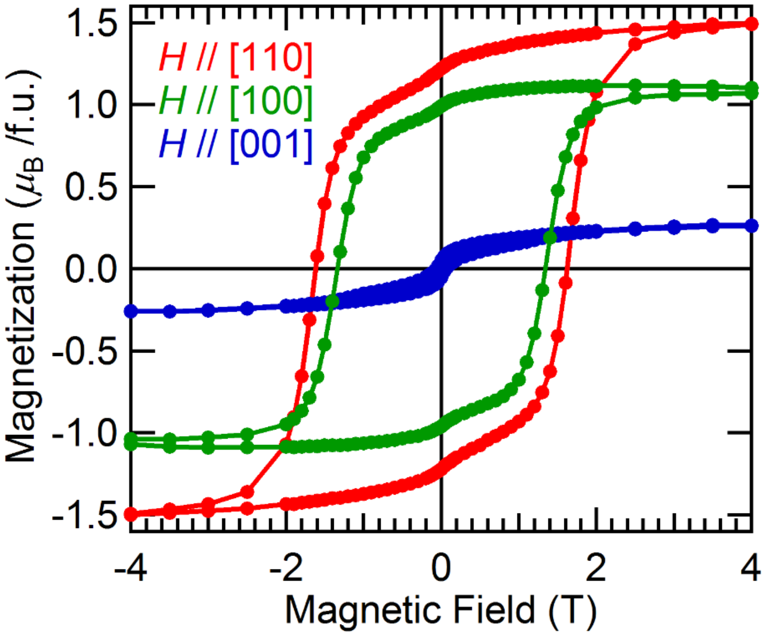

Figure 6-8. *M*-*H* curves for the $YBaCo_2O_6$ film at 5 K by applying *H* along [110], [100], and [001] directions.

magnetization (M_s) depended on the magnetic field direction. That is, the (H_c, M_s) values of the $YBaCo_2O_6$ film at 5 K were (1.6 T, 1.5 μ_B/f.u.), (1.3 T, 1.1 μ_B/f.u.), and (0.08 T, 0.3 μ_B/f.u.) when *H* was applied along [110], [100], and [001] directions, respectively, indicating that the magnetic moment was hardly parallel to *c*-axis because of the *A*-site cation-ordered structure along *c*-axis. This demonstrates the large crystal magnetic anisotropy.

Figure 6-9(a) shows the *M*-*T* curves of the $YBaCo_2O_6$ film with $H = 0.1$ T along [110] direction. The splitting between ZFC and FC magnetizations occurred below ~130 K, which corresponds to ferromagnetic - paramagnetic phase transition temperature. The ZFC magnetization possessed a maximum at 112 K, which is approximately 20 K lower than the Currie temperature (T_C), 130 K. This behaviour is typical in ferromagnetic (short-range ordered) cluster model [159,160]; i.e., both ferromagnetic and antiferromagnetic phases coexist in the film. The ferromagnetism is thought to originate from the double exchange interaction between Co^{3+} and Co^{4+}, while the antiferromagnetic one may come from the superexchange interactions between Co^{3+} and Co^{3+} and between Co^{4+} and Co^{4+}.

The $YBaCo_2O_6$ film exhibited metallic behavior (Fig. 6-9(b)), proving that the $YBaCo_2O_6$ film was a ferromagnetic metal with T_C of 130 K. There was a kink point in the ρ-T curve near T_C evaluated from the M-T curve. The film showed negative magnetoresistance (MR) below 200 K owing to the magnetic field-induced spin polarization. The MR values were –4.3 and –0.6% at 10 K with H = 9 T along [100] and [001] directions, respectively.

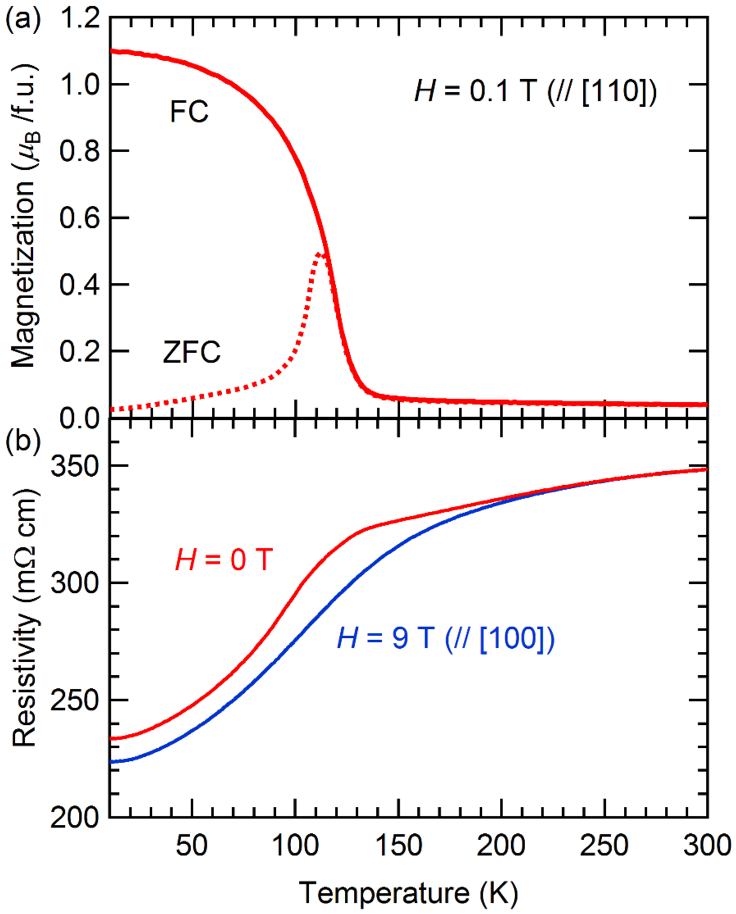

Figure 6-9. (a) M-T curves for the $YBaCo_2O_6$ film at H = 0.1 T along [110] direction. Field cooling (FC) and zero field cooling (ZFC) measurements are drawn as solid and dot lines, respectively. (b) ρ-T curves for the $YBaCo_2O_6$ film at H = 0 and 9 T along [100] direction.

6.4 Conclusion

In this chapter, I successfully fabricated $YBaCo_2O_x$ (x = 4.5−6) epitaxial thin films with *A*-site cation-ordered perovskite structure by combining PLD and topotactic reduction and oxidation methods. The x range obtained in this study, 4.5−6, was wider than the previous reports, 4.5−5.5, manifesting the strong oxidizing power of NaClO and high reactivity of the films. The *c*-axis lengths and resistivities of the $YBaCo_2O_x$ films tended to decrease with decreasing x when $x \geq 5.3$ but increased when $x \sim 4.5$. The $YBaCo_2O_{5.5}$ film showed semiconducting behavior without MIT, possibly because of the epitaxial strain effect. The resistivity behaviors of the $YBaCo_2O_{5.5}$ and $YBaCo_2O_{4.5}$ films could be described by the 3D VRH and Efros-Shklovskii-type hopping models, respectively. On the other hand, the new phase, $YBaCo_2O_6$, exhibited ferromagnetic metallic behavior with T_C of 130 K. The film also showed large crystal magnetic anisotropy, owing to the cation-ordering.

Chapter 7 General conclusion

In this thesis, I demonstrated anion control in perovskite transition metal oxide epitaxial thin films via four types of topotactic reactions: hydridation, fluorination, reduction, and oxidation. The topotactic techniques applied to thin-film samples enable to fabricate new phases, owing to the larger surface area/volume ratio and stabilization of the perovskite-based framework arising from the epitaxial effect.

In Chapter 3, I described fabrication of perovskite $SrCoO_xH_y$ and $SrVO_2H$ oxyhydride films via topotactic hydridation of $SrCoO_{2.5}$ and $SrVO_3$ films using CaH_2, respectively. The new phase of $SrCoO_xH_y$ film was epitaxially stabilized by substrate and possessed novel two-dimensional Co–H^-–Co networks. The film exhibited insulating behavior and had a direct band gap of 2.1 eV. On the other hand, the $SrVO_2H$ films were grown in single-crystalline form and possessed 1D V-H^--V bonds along the out-of-plane direction. The synthesis temperature of the $SrVO_2H$ film was lowered by reducing the film thickness.

In Chapter 4, I presented perovskite oxyfluoride $SrFeO_{3-x}F_x$ and $SrCoO_xF_y$ epitaxial thin films fabricated via topotactic fluorination of $SrFeO_{3-\delta}$ and $SrCoO_{2.5}$ films using PVDF, respectively. The fluorination temperature of the $SrFeO_{3-x}F_x$ films, 150–270 °C, was much lower than that of the polycrystalline bulk one, 400 °C. Furthermore, the fluorine content (x) of the $SrFeO_{3-x}F_x$ films was widely controllable by the fluorination temperature and/or the amount of oxygen vacancies in the precursor film. The optical bandgap of the $SrFeO_{3-x}F_x$ films was expanded with fluorine doping. On the other hand, the new $SrCoO_xF_y$ phase possessed relatively low Co oxidation state of $Co^{2+/3+}$.

In Chapter 5, I reported on preparation of single-crystalline $SrFeO_2$ epitaxial thin films on perovskite substrates with various lattice parameters by combining PLD method with solid-phase reduction using CaH_2. High crystallinity films fabricated on lattice-matched KTO substrate exhibited metallic conduction, while those on STO and DSO substrates were insulating, in analogy to bulk $SrFeO_2$. The electron carriers are supplied by oxygen vacancies or hydrogen ions in the metallic $SrFeO_2$ films. In addition, the crystallinity and thus conductivity of $SrFeO_2$ film could be enhanced by Sm substitution for Sr.

In Chapter 6, I performed topotactic oxidation and reduction on *A*-site cation-ordered perovskite $YBaCo_2O_x$ epitaxial thin films using NaClO and CaH_2, respectively. The x values of the films were controllable in a wide range of 4.5−6. The new $YBaCo_2O_6$ phase exhibited ferromagnetic metallic behavior with T_C of 130 K possibly due to the double exchange interaction between Co^{3+} and Co^{4+}, while the $YBaCo_2O_x$ films with $x \leq 5.5$ were found to be an antiferromagnetic insulator. Moreover, the $YBaCo_2O_6$ film exhibited crystal magnetic anisotropy and negative magnetoresistance.

In conclusion, topotactic reactions on perovskite transition metal oxide thin films were performed and new mixed anion phases were obtained showing interesting properties such as new anion arrangement and easily controllable anion ratio. These findings proved that topotactic anion doping into transition metal oxide thin films is a promising way of synthesizing new mixed anion compounds.

Acknowledgement

Foremost, I would like to show my greatest appreciation to my supervisor Prof. Tetsuya Hasegawa for the continuous support of this study. His unconditional guidance and support during these past six years make this thesis possible. I was encouraged many times by his warm personality and insightful scientific advice. The time I spent in his laboratory will help me much in the future. I am also deeply grateful to Dr. Akira Chikamatsu who is my immediate boss in the laboratory. He gave me many opportunities to develop this study and guided me to be a good scientist with his invaluable patience and suggestions. A great deal of discussions with him helped me to solve issues.

I want to express my great gratitude to Prof. Tomoteru Fukumura and Prof. Yasushi Hirose for the great scientific advice. They always helped me with their deep knowledge about solid state chemistry. I also thank to Dr. Hideyuki Kamisaka for his support about computational calculation. I also thank to my collaborators. Prof. Hiroshi Kumigashira of High Energy Accelerator Research Organization (KEK) Institute of Materials Structure Science and Prof. Hiroki Wadati, Prof. Yasuyuki Hirata and Yuichi Yokoyama of The University of Tokyo assisted me to carry out the XPS and XAS measurements.

I thank present and past coworkers who helped this work: S. Nakao, T. Matsuyama, Dr. K. Shigematsu, R. Takagi, T. Onozuka, K. Kawahara, Y. Kurauchi, K. Yamada and Y. Suzuki. Their assistances and suggestions were essential. I am also thankful to other labmates: Dr. S. Okazaki, Dr. C. Yang, Dr. Y. Park, Dr. D. Ogawa, Dr. A. Watanabe, Dr. J. Wei, Dr. D Oka, A. Suzuki, K. Aizawa, K. Shimamoto, S. Kojima, J. Tanihira, M. Otaki, X. Shen, S. Inoue, M. Oka, R. Sei, K. Kurita, R. Takagi, K. Kaminaga, M. Sano, J. Takahashi, V. Motaneeyachart, K. Yamatake, R. Kantake, F. S. Kahn, Y. Uchida, T. Yamazaki, D Kutsuzawa, T. Takeda, S. Shibata, N. Kashiwa, N. Hashimoto, K. Maruyama, S. Fujiwara, T. Fukumoto, M. Umino, A. Imoji, M. Kikuchi and M.

Komazawa.

I especially thank Thantip S. Krasienapibal for her invaluable support and encouragement. She is very active and smart, and has a wonderful smile. When I am at my wit's end, she always continues encouraging and helps to make a good plan. An encounter with her is very lucky for me.

I will be forever grateful to my family. They support me everyday with their infinite love. I respect them a lot and want to be like them. I dedicate this thesis to my family.

Publications related to the thesis

This thesis contains the contents of the following publications.

1. “Topotactic fluorination of strontium iron oxide thin films using polyvinylidene fluoride” T. Katayama, A. Chikamatsu, Y. Hirose, R. Takagi, H. Kamisaka, T. Fukumura, and T. Hasegawa, J. Mater. Chem. C **2**, 5350 (2014).
2. “Metallic conductivity in infinite-layer strontium iron oxide thin films reduced by calcium hydride” T. Katayama, A. Chikamatsu, Y Hirose, H. Kumigashira, T. Fukumura, and T. Hasegawa, J. Phys. D: Appl. Phys. **47**, 135304 (2014).
3. “Topotactic reductive fluorination of strontium cobalt oxide epitaxial thin films” T. Katayama, A. Chikamatsu, Y. Hirose, T. Fukumura, and T. Hasegawa, J. Sol-Gel Sci. Technol. **73**, 527 (2015).
4. “Topotactic synthesis of strontium cobalt oxyhydride thin film with perovskite structure” T. Katayama, A. Chikamatsu, H. Kamisaka, Y. Yokoyama, Y. Hirata, H. Wadati, T. Fukumura, and T. Hasegawa, AIP Adv. **5**, 107147 (2015).
5. “Experimental and theoretical investigation of electronic structure of $SrFeO_{3-x}F_x$ epitaxial thin films prepared via topotactic reaction” T. Katayama, A. Chikamatsu, H. Kamisaka, H. Kumigashira, and T. Hasegawa, Appl. Phys. Express **9**, 025801 (2016). (Selected as Spotlight)
6. “Topotactic reductive synthesis of *A*-site cation-ordered perovskite $YBaCo_2O_x$ (x = 4.5−5.5) epitaxial thin films” T. Katayama, A. Chikamatsu, T. Fukumura, and T. Hasegawa, Jpn. J. Appl. Phys. *in press*.

References

[1] M. A. Hayward, *Comprehensive Inorganic Chemistry II (Second Edition)* (Elsevier, 2013) Chapter 2.15

[2] A. R. Armstrong, and P. A. Anderson, Inorg. Chem. **33**, 4366 (1994).

[3] R. J. Cave, A. Santoro, D. W. Murphy, S. M. Zahurak, and R. S. Roth, J. Solid State Chem. **50**, 121 (1983).

[4] Y Takahashi, N Kijima, K Tokiwa, T Watanabe, and J Akimoto, J. Phys.: Condens. Matter. **19**, 436202 (2007)

[5] A. P. Drozdov, M. I. Eremets, I. A. Troyan, V. Ksenofontov, and S. I. Shylin, Nature **525**, 73 (2015).

[6] L. Gao, Y. Y. Xue, F. Chen, Q. Xiong, R. L. Meng, D. Ramirez, C. W. Chu, J. H. Eggert, and H. K. Mao, Phys. Rev. B **50**, 4260 (1994).

[7] M. C. Verbraeken, C. Cheung, E. Suard, and J. T. S. Irvine, Nat. Mater. **14**, 95 (2015).

[8] B. Malaman, and J. F. Brice, J. Solid State Chem. **53**, 44 (1984).

[9] M. A. Hayward, E. J. Cussen, J. B. Claridge, M. Bieringer, M. J. Rosseinsky, C. J. Kiely, S. J. Blundell, I. M. Marshall, and F. L. Pratt, Science **295**, 1882 (2002).

[10] C. A. Bridges, G. R. Darling, M. A. Hayward, and M. J. Rosseinsky, J. Am. Chem. Soc. **127**, 5996 (2005).

[11] S. J. Blundell, I. M. Marshall, F. L. Pratt, M. A. Hayward, E. J. Cussen, J. B. Claridge, M. Bieringer, C. J. Kiely, and M. J. Rosseinsky, Physica B **326**, 527 (2003).

[12] F. D. Romero, A. Leach, J. S. Mçller, F. Foronda, S. J. Blundell, and M. A. Hayward, Angew. Chem. **126**, 7686 (2014).

[13] J. Bang, S. Matsuishi, H. Hiraka, F. Fujisaki, T. Otomo, S. Maki, J. Yamaura, R. Kumai, Y. Murakami, and H. Hosono, J. Am. Chem. Soc. **136**, 7221 (2014).

[14] R. M. Helps, N. H. Rees, and M. A. Hayward, Inorg. Chem. **49**, 11062 (2010).

[15] Y. Kobayashi, O. J. Hernandez, T. Sakaguchi, T. Yajima, T. Roisnel, Y. Tsujimoto, M. Morita, Y. Noda, Y. Mogami, A. Kitada, M. Ohkura, S. Hosokawa, Z. Li, K. Hayashi, Y. Kusano, J. Kim, N. Tsuji, A. Fujiwara, Y. Matsushita, K. Yoshimura, K. Takegoshi, M. Inoue, M. Takano, and H. Kageyama, Nat. Mater. **11**, 507 (2012).

[16] C. Tassel, Y. Goto, Y. Kuno, J. Hester, M. Green, Y. Kobayshi, and H. Kageyama, Angew. Chem. **53**, 10377 (2014).

[17] T. Yajima, A. Kitada, Y. Kobayashi, T. Sakaguchi, G. Bouilly, S. Kasahara, T. Terashima, M. Takano, and H. Kageyama, J. Am. Chem. Soc. **134**, 8782 (2012).

[18] T. Yamamoto, R. Yoshii, G. Bouilly, Y. Kobayashi, K. Fujita, Y. Kususe, Y. Matsushita, K. Tanaka, and H. Kageyama, Inorg. Chem. **54**, 1501 (2015).

[19] M. A. Hayward, and M. J. Rosseinsky, Chem. Mater. 12, 2182 (2000).

[20] Y. Wei, H. Gui, X. Li, Z. Zhao, Y. H. Zhao, and W. Xie, J. Phys.: Condens. Matter. **27**, 206001 (2015).

[21] M. Al-Mamouri, P. P. Edwards, C Greaves, and M. Slaski, Nature **369**, 382 (1994).

[22] G. Ehora, C. Renard, S. Daviero-Minaud, and O. Mentre, Chem. Mater. **19**, 2924 (2007).

[23] O. Clemens, and P. R. Slater, Rev. Inorg. Chem. **33**, 105 (2013).

[24] Y. Inaguma, J. M. Greneche, M. P. Crosnier-Lopez, T. Katsumata, Y. Calage, and J. L. Fourquet, Chem. Mater. **17**, 1386 (2005).

[25] Y. Tsujimoto, J. J. Li, K. Yamaura, Y. Matsushita, Y. Katsuya, M. Tanaka, Y. Shirako, M. Akaogi, and E. Takayama-Muromachi, Chem. Commun. **47**, 3263 (2011).

[26] R. K. Li, and C. Greaves, Phys. Rev. B **62**, 3811 (2000).

[27] E. Sullivan, and C. Greaves, Mater. Res. Bull. **47**, 2541 (2012).

[28] A. M. Abakumov, J. Hadermann, G. V. Tendeloo, R. V. Shpanchenko, P. N. Oleinikov, and E. V. Antipov, J. Solid State Chem. **142**, 440 (1999).

[29] P. R. Slater, and R. K. B. Gover, J. Mater. Chem. **12**, 291 (2002).

[30] M. G. Francesconi, P. R. Slater, J. P. Hodges, C. Greaves, P. P. Edwards, M. Al-Mamouri, and M. Slaski, J. Solid State Chem. **135**, 17 (1998).

[31] F. J. Berry, X. Ren, R. Heap, P. Slater, M. F. Thomas, Solid State Commun. **134**, 621 (2005).

[32] F. J. Berry, R. Heap, Ö. Helgason, E. A. Moore, S. Shim, P. R. Slater, and M. F. Thomas, J. Phys.: Condens. Matter **20**, 215207 (2008).

[33] Y. Kobayashi, M. Tian, M. Eguchi, and T. E. Mallouk, J. Am. Chem. Soc. **131**, 9849 (2009).

[34] R. Heap, P. R. Slater, F. J. Berry, O. Helgason and A. J. Wright, Solid State Commun. **141**, 467 (2007).

[35] O. Clemens, M. Kuhn, and R. Haberkorn, J. Solid State Chem. **184**, 2870 (2011).

[36] C. A. Hancock, T. Herranz, J. F. Marco, F. J. Berry, and P. R. Slater, J. Solid State Chem. **186**, 195 (2012).

[37] P. R. Slater, J. Fluorine Chem. **117**, 43. (2002).

[38] T. Sivakumar, and J. B. Wiley, Mater. Res. Bull. **44**, 74 (2009).

[39] T. Kawashima, Y. Matsui, and E. Takayama-Muromachi, Physica C **257**, 313 (1996).

[40] M. Sturza, H. Kabbour, S. Daviero-Minaud, D. Filimonov, K. Pokholok, N. Tiercelin, F. Porcher, L. Aldon and O. Mentré, J. Am. Chem. Soc. **133**, 10901 (2011).

[41] C. M. Thompson, C. K. Blakely, R. Flacau, J. E. Greedan, and V. V. Poltavets, J. Solid State Chem. **219**, 173 (2014).

[42] F. J. Berry, F. C. Coomer, C. Hancock, Ö. Helgason, E. A. Moore, P. R. Slater, A. J. Wright, and M. F. Thomas, J. Solid State Chem. **184**, 1361 (2011).

[43] H. E. Shinawi, J. F. Marco, F. J. Berry, and C. Greaves, J. Mater. Chem. **20**, 3253 (2010).

[44] O. Mentré, H. Kabbour, G. Ehora, G. Tricot, S. Daviero-Minaud, and M. H. Whangbo, J. Am. Chem. Soc. **132**, 4865 (2010).

[45] L. D. Aikens, L. J. Gillie, R. K. Li, and C. Greaves, J. Mater. Chem. **12**, 264 (2002).

[46] Y. Tsujimoto, K. Yamaura, and T. Uchikoshi, Inorg. Chem. **52**, 10211 (2013).

[47] R. L. Toquin, W. Paulus, A. Cousson, C. Prestipino, and C. Lamberti, J. Am. Chem. Soc. **128**, 13161 (2006).

[48] C. C. K. Chiang, and K. R. Poeppelmeier, Mater. Lett. **12**, 102 (1991).

[49] B.H. Chen, D. Walker, B. A. Scott, and D. B. Mitzi, J. Solid State Chem. **121**, 498 (1996).

[50] J. A. Alonso, M. J. Martínez-Lope, J. L. García-Munoz, and M. T. Fernandez-Díaz, J. Phys.: Condens. Matter **9**, 6417 (1997).

[51] A. Nemudry, M. Weiss, I. Gainutdinov, V. Boldyrev, and R. Schöllhorn, Chem. Mater. **10**, 2403 (1998).

[52] A. Nemudry, P. Rudolf, and R. Schöllhorn, Chem. Mater. **8**, 2232 (1996).

[53] O. H. Hansteen, H. Fjellvåg, and B. C. Hauback, J. Solid State Chem. **141**, 411 (1998).

[54] T. Yamamoto, and H. Kageyama, Chem. Lett. **42**, 946953 (2013).

[55] M. A. Hayward, M. A. Green, M. J. Rosseinsky, and J. Sloan, J. Am. Chem. Soc. **121**, 8843 (1999).

[56] V. V. Poltavets, K. A. Lokshin, S. Dikmen, M. Croft, T. Egami, and M. Greenblatt, J. Am. Chem. Soc. **128**, 9050 (2006).

[57] C. K. Blakely, S. R. Bruno, and V. V. Poltavets, Inorg. Chem. **50**, 6696 (2011).

[58] Y. Tsujimoto, C. Tassel, N. Hayashi, T. Watanabe, H. Kageyama, K. Yoshimura, M. Takano, M. Ceretti, C. Ritter, and W. Paulus, Nature **450**, 1062 (2007).

[59] C. Tassel, J. M. Pruneda, N. Hayashi, T. Watanabe, A. Kitada, Y. Tsujimoto, H. Kageyama, K. Yoshimura, M. Takano, M. Nishi, K. Ohoyama, M. Mizumaki, N. Kawamura, J. Íñiguez, and E. Canadell, J. Am. Chem. Soc. **131**, 221 (2009).

[60] T. Yamamoto, Y. Kobayashi, N. Hayashi, C. Tassel, T. Saito, S. Yamanaka, M. Takano, K. Ohoyama, Y. Shimakawa, K. Yoshimura, and H. Kageyama, J. Am. Chem. Soc. 134, 11444 (2012).

[61] F. D. Romero, S. J. Burr, J. E. McGrady, D. Gianolio, G. Cibin, and M. A. Hayward, J. Am. Chem. Soc. **135**, 1838 (2013).

[62] C. Tassel, L. Seinberg, N. Hayashi, S. Ganesanpotti, Y. Ajiro, Y. Kobayashi, and H. Kageyama, Inorg. Chem. **52**, 6096 (2013).

[63] H. Kageyama, T. Watanabe, Y. Tsujimoto, A. Kitada, Y. Sumida, K. Kanamori, K. Yoshimura, N. Hayashi, S. Muranaka, M. Takano, M. Ceretti, W. Paulus, C. Ritter, and G. André, Angew. Chem., Int. Ed. **47**, 5740 (2008).

[64] E. Dixon, J. Hadermann, S. Ramos, A. L. Goodwin, and M. A. Hayward, J. Am. Chem. Soc. **133**, 18397 (2011).

[65] H. J. Kitchen, I. Saratovsky, and M. A. Hayward, Dalton Trans. **39**, 6098 (2010).

[66] J. Seddon, E. Suard, and M. A. Hayward, J. Am. Chem. Soc. **132**, 2802 (2010).

[67] F. C. Chou, J. H. Cho, and D. C. Johnston, Physica C **197**, 303 (1992).

[68] T. Hirayama, M. Nakagawa, A. Sumiyama, and Y. Oda, Phys. Rev. B **58**, 5856 (1998).

[69] H. Sato, M. Naito, and H. Yamamoto, Physica C **280**, 178 (1997).

[70] E. Takayma-Muromachi, T. Sasaki, and Y. Matsui, Physica C **207**, 97 (1993).

[71] C. Rial, E. Morán, M. A. Alario-Franco, U. Amador, N. H. Andersen, Physica C **278**, 122 (1997).

[72] Q. Y. Tu, X. L. Chen, B. K. Ma, Z. X. Zhao, Y. C. Lan, J. K. Liang, Appl. Phys. A **74**, 79 (2002).

[73] F. Millange, V. Caignaert, B. Domengès, B. Raveau, and E. Suard, Chem. Mater. **10**, 1974 (1998).

[74] T. Nakajima, M. Ichihara and Y. Ueda, J. Phys. Soc. Jpn. **74**, 1572 (2005).

[75] Y. Hosaka, N. Ichikawa, T. Saito, P. Manuel, D. Khalyavin, J. P. Attfield, and Y. Shimakawa, J. Am. Chem. Soc. **137**, 7468 (2015).

[76] S. Inoue, M. Kawai, Y. Shimakawa, M. Mizumaki, N. Kawamura, T. Watanabe, Y. Tsujimoto, H. Kageyama, and K. Yoshimura, Appl. Phys. Lett. **92**, 161911 (2008).

[77] M. Kawai, S. Inoue, M. Mizumaki, N. Kawamura, N. Ichikawa, and Y. Shimakawa,

Appl. Phys. Lett. **94**, 082102 (2009).

[78] F. Arrouy, J. P. Locquet, E. J. Williams, E. Mächler, R. Berger, C. Gerber, C. Monroux, J. C. Grenier, and A. Wattiaux, Phys. Rev. B **54**, 7512 (1996).

[79] G. Bouilly, T. Yajima, T. Terashima, Y. Kususe, K. Fujita, C. Tassel, T. Yamamoto, K. Tanaka, Y. Kobayashia, and H. Kageyama, CrystEngComm. **16**, 9669 (2014).

[80] S. Ohashi, M. Lippmaa, N. Nakagawa, H. Nagasawa, H. Koinuma, and M. Kawasaki, Rev. Sci. Instrum. **70**, 178 (1999).

[81] M. N. R. Ashfold, F. Claeyssens, G. M. Fuge, and S. J. Henley, Chem. Soc. Rev. **33**, 23 (2004).

[82] J. C. Morris, J. Phys. Chem. **70**, 3798 (1966).

[83] J. M. Cowley, *Diffraction Physics* (Elsevier, 1995)

[84] F. J. Giessibl, Rev. Mod. Phys. **75**, 949 (2003).

[85] N. Dellby, O. L. Krivanek, P. D. Nellist, P. E. Batson, and A. R. Lupini, J. Electron Microscopy **50**, 177 (2001).

[86] J. Goldstein, *Practical Scanning Electron Microscopy* (Springer Science & Business Media, 2012)

[87] A. Kinbara, and S. Yoshida, *薄膜の評価技術ハンドブック* (株式会社テクノシステム, 2013)

[88] D. Drouin, A. R. Couture, D. Joly, X. Tastet, V. Aimez, and R. Gauvin, Scanning, **29**, 92 (2007).

[89] J. R. Tesmer, and M. Nastasi, *Handbook of Modern Ion Beam Analysis* (Materials Research Society, 1995)

[90] D. Dieumegard, B. Maurel, and G. Amsel, Nucl. Instr. and Meth. **168**, 93 (1980).

[91] S. Hüfner, *Photoelectron Spectroscopy* (Springer Science & Business Media, 2013)

[92] O. S. Heavens, Chapter 5. *Optical Properties of Thin Solid Films* (Courier Corporation, 1991)

[93] 日本化学会編集, *実験化学講座 7 電気物性、磁気物性* (丸善株式会社, 2004)

[94] B. D. Cullity, and C. D. Graham, *Introduction to Magnetic Materials* (John Wiley

& Sons, 2009)

[95] F. Jensen, *Introduction of Computational Chemistry* (John Wiley & Sons, 2007)

[96] N. Ichikawa, M. Iwanowska, M. Kawai, C. Calers, W. Paulusb, and Y. Shimakawa, Dalton Trans. **41**, 10507 (2012).

[97] H. Jeen,W. S. Choi, M. D. Biegalski, C. M. Folkman, I. C. Tung, D. D. Fong, J. W. Freeland, D. Shin, H. Ohta, M. F. Chisholm, and H. N. Lee, Nat. Mater. **12**, 1057 (2013).

[98] V. V. Vashook, M. V. Zinkevich, and Y. G. Zonov, Solid State Ionics **116**, 129 (1999).

[99] A. N. Vasiliev, O. S. Volkova, L. S. Lobanovskii, I. O. Troyanchuk, Z. Hu, L. H. Tjeng, D. I. Khomskii, H. J. Lin, C. T. Chen, N. Tristan, F. Kretzschmar, R. Klingeler, and B. Büchner, Phys. Rev. B **77**, 104442 (2008).

[100] W. S. Choi, H. Jeen, J. H. Lee, S. S. A. Seo, V. R. Cooper, K. M. Rabe, and H. N. Lee, Phys. Rev. Lett. 2013, 111, 097401.

[101] H. Nagata, T. Tsukahara, M. Yoshimoto and H. Koinuma, Thin Solid Films **208**, 264 (1992).

[102] H. F. Pen, M. Abbate, A. Fuijmori, Y. Tokura, H. Eisaki, S. Uchida, and G. A. Sawatzky, Phys. Rev. B **59**, 7422 (1999).

[103] E. Hryha, E. Rutqvist, and L. Nyborg, Surf. Interface Anal. **44**, 1022 (2012).

[104] R. P. Vasquez, J. Electron Spectrosc. Relat. Phenom. **56**, 217 (1991).

[105] E. J. Moon, Y. Xie, E. D. Laird, D. J. Keavney, C. Y. Li, and S. J. May, J. Am. Chem. Soc. **136**, 2224 (2014).

[106] G. Kresse, and J. Furthmüller, Phys. Rev. B **54**, 11169 (1996).

[107] J. M. Pruneda, J. Iniguez, E. Canadell, H. Kageyama, and M. Takano, Phys. Rev. B **78**, 115101 (2008).

[108] O. Diéguez, O. E. González-Vázquez, J. C. Wojdeł, and J. Íñiguez, Phys. Rev. B **83**, 094105 (2011).

[109] G. Rollmann, A. Rohrbach, P. Entel, and J. Hafner, Phys. Rev. B **69**, 165107 (2004).

[110] W. C. Koehler, and E. O. Wollan, J. Phys. Chem. Solids **2**, 100 (1957).

[111] G. Kresse, and D. Joubert, Phys. Rev. B **59**, 1758 (1999).

[112] I. D. Brown, and D. Altermatt, Acta Cryst. **B41**, 244 (1985).

[113] H. Wadati, D. Kobayashi, H. Kumigashira, K. Okazaki, T. Mizokawa, A. Fujimori, K. Horiba, M. Oshima, N. Hamada, M. Lippmaa, M. Kawasaki and H. Koinuma, Phys. Rev. B **71**, 035108 (2005).

[114] T. Yamashita and P. Hayes, Appl. Surf. Sci. **254**, 2441 (2008).

[115] A. Chikamatsu, T. Matsuyama, Y. Hirose, H. Kumigashira, M. Oshima, and T. Hasegawa, J. Electron Spectrosc. Relat. Phenom. **184**, 547 (2012).

[116] H. Yamada, M. Kawasaki and Y. Tokura, Appl. Phys. Lett. **80**, 622 (2002).

[117] E. Fischer, L. Joshua and J. L. Hertz, Solid State Ionics **218**, 18 (2012).

[118] M. D. Scafetta, Y. J. Xie, M. Torres, J. E. Spanier, and S. J. May, Appl. Phys. Lett. **102**, 081904 (2013).

[119] H. Wadati, A. Chikamatsu, M. Takizawa, R. Hashimoto, H. Kumigashira, T. Yoshida, T. Mizok, A. Fujimori, M. Oshima, M. Lippmaa, M. Kawasaki, and H. Koinuma, Phys. Rev. B **74**, 115114 (2006).

[120] C. K. Blakely, J. D. Davis, S. R. Bruno, S. K. Kraemer, M. Zhu, X. Ke, W. Bi, E. E. Alp, and V. V. Poltavets, J. Fluor. Chem. 159, 8 (2014).

[121] L. Pauling, J. Am. Chem. Soc. 54, 3570 (1932).

[122] H. Mizoguchi, H. W. Eng, and P. M. Woodward, Inorg. Chem. 43, 1667 (2004).

[123] J. B. Torrance, P. Lacorre, and A. I. Nazzal, Phys. Rev. B 45, 8209 (1992).

[124] Y. Tsujimoto, C. I. Sathish, K. P. Hong, K. Oka, M. Azuma, Y. Guo, Y. Matsushita, K. Yamaura, and E. Takayama-Muromachi, Inorg. Chem. **51**, 4802 (2012).

[125] K. Luo, T. T, Tran, P. S. Halasyamani, and M. A. Hayward, Inorg. Chem. **52**, 13762 (2013).

[126] M. Itoh, I. Natori, S. Kubota, and K. Motoya, J. Phys. Soc. Jpn. **63**, 1486 (1994).

[127] D. Fuchs, P. Schweiss, P. Adelmann, T. Schwarz, and R. Schneider, Phys. Rev. B **72**, 014466 (2005).

[128] A. Chainani, M. Mathew, and D. D. Sarma, Phys. Rev. B **46**, 9976 (1992).

[129] F. Munakata, H. Takahashi, and Y. Akimune, Phys. Rev. B **56**, 979 (1997).

[130] M. C. Biesinger, B. P. Payne, A. P. Grosvenor, L. W. M. Lau, A. R. Gerson, and R. S. C. Smart, Appl. Surf. Sci. **257**, 2717 (2011).

[131] R. D. Shanon, Acta Cryst. A **32**, 751 (1976).

[132] Y. Shimakawa, S. Inoue, M. Haruta, M. Kawai, K. Matsumoto, A. Sakaiguchi, N. Ichikawa, S. Isoda, and H. Kurata, Cryst. Growth Des. **10**, 4713 (2010).

[133] See for example: M. G. Smith, A. Manthiram, J. Zhou, J. B. Goodenough, and J. T. Markert, Nature **351**, 549 (1991).

[134] L. Seinberg, T. Yamamoto, C. Tassel, Y. Kobayashi, N. Hayashi, A. Kitada, Y. Sumida, T. Watanabe, M. Nishi, K. Ohoyama, K. Yoshimura, M. Takano, W. Paulus, and H. Kageyama, Inorg. Chem. **50**, 3988 (2011).

[135] M. Retuerto, F. Jiménez-Villacorta, M. J. Martínez-Lope, M. T. Fernández-Díaz, and J. A. Alonso, Inorg. Chem. **50**, 10929 (2011).

[136] T. Kawakami, T. Tsujimoto, H. Kageyama, X. Q. Chen, C. L. Fu, C. Tassel, A. Kitada, S. Suto, K. Hirama, Y. Sekiya, Y. Makino, T. Okada, T. Yagi, N. Hayashi, K. Yoshimura, S. Nasu, R. Podloucky, and M. Takano, Nat. Chem. **1**, 371 (2009).

[137] T. Matsuyama, A. Chikamatsu, Y. Hirose, T. Fukumura, and T. Hasegawa, Appl. Phys. Express **4**, 013001 (2011).

[138] K. Seeger, *Semiconductor Physics* (Springer, Berlin,1991)

[139] J. Hombo, Y. Matsumoto, and T. Kawano, J. Solid State Chem. **84**, 138 (1990).

[140] M. V. Patrakeev, I. A. Leonidov, V. L. Kozhevnikov, and K. R. Poeppelmeier, J. Solid State Chem. **178**, 921 (2005).

[141] Y. Krockenberger, K. Sakuma, and H. Yamamoto, Appl. Phys. Express **5**, 043101 (2012). The μ_H(300 K) value of the $Sr_{0.9}La_{0.1}CuO_2$ film was estimated from its resistivity and the La concentration, which was assumed to be equal to the carrier density.

[142] A. Ohtomo, and H. Y. Hwang, Nature **427**, 423 (2004).

[143] C. Kılıç, and A. Zunger, Appl. Phys. Lett. **81**, 73 (2002).

[144] M. Alexander, H. Romberg, N. Nücker, P. Adelmann, J. Fink, J. T. Markert, M. B. Maple, S. Uchida, H. Takagi, Y. Tokura, A. C. W. P. James, and D. W. Murphy: Phys. Rev. B **43**, 333 (1991).

[145] A. A. Taskin, A. N. Lavrov, and Y. Ando, Phys. Rev. B **71**, 134414 (2005).

[146] C. Martin, A. Maignan, D. Pelloquin, N. Nguyen, and B. Raveau, Appl. Phys. Lett. **71**, 1421 (1997).

[147] S. Roy, I. S. Dubenko, M. Khan, E. M. Condon, J. Craig, and N. Ali, Phys. Rev. B **71**, 024419 (2005).

[148] A. A. Taskin, A. N. Lavrov, and Y. Ando, Appl. Phys. Lett. **86**, 091910 (2005).

[149] A. Tarancón, S. J. Skinner, R. J. Chater, F. Hernández-Ramírez, and J. A. Kilner, J. Mater. Chem. **17**, 3175 (2007).

[150] E. L. Rautama and M. Karppinen, J. Solid State Chem. **183**, 1102 (2010).

[151] A. Maignan, C. Martin, D. Pelloquin, N. Nguyen, and B. Raveau, J. Solid State Chem. **142**, 247 (1999).

[152] D. Akahoshi and Y. Ueda, J. Solid State Chem. **156**, 355 (2001).

[153] V. Pralong, V. Caignaert, S. Hebert, A. Maignan, B. Raveau, Solid State Ionics. **177**, 1879 (2006).

[154] M. M. Seikh, V. Pralong, O. I. Lebedev, V. Caignaert, and B. Raveau, J. Appl. Phys. **114**, 013902 (2013).

[155] D. D. Khalyavin, D. N. Argyriou, U. Amann, A. A. Yaremchenko, and V. V. Kharton, Phys. Rev. B **75**, 134407 (2007).

[156] T. Vogt, P. M. Woodward, P. Karen, B. A. Hunter, P. Henning, and A. R. Moodenbaugh, Phys. Rev. Lett. **84**, 2969 (2000).

[157] J. P. Pantoj, C. Frontera, J. Herrero-Martín, and J. L. García-Muńoz, J. Appl. Phys. **111**, 07D710 (2012).

[158] R. H. Potze, G. A. Sawatzky, and M. Abbate, Phys. Rev. B **51**, 11501 (1995).

[159] J. Wu and C. Leighton, Phys. Rev. B **67**, 174408 (2003).

[160] K. Asai, O. Yokokura, N. Nishimori, H. Chou, J. M. Tranquada, G. Shirane, S. Higuchi, Y. Okajima, and K. Kohn, Phys. Rev. B **50**, 3025 (1994).